

**Development of a novel iron-manganese alloy and its application**

**by**

**Vikram Varadaraajan**

**A dissertation submitted in partial fulfillment  
of the requirements for the degree of  
Doctor of Philosophy  
(Automotive System Engineering)  
in The University of Michigan-Dearborn  
2015**

**Doctoral Committee:**

**Professor Pravansu Mohanty, Chair  
Associate Professor Cheol Lee  
Associate Professor German Reyes  
Professor Oleg Zikanov**

© Vikram Varadaraajan

---

2015

*To my loving parents,*

## **Acknowledgements**

First and foremost, I would like to thank my parents for their love and support. Words cannot express my appreciation for the countless sacrifices and prayers they have made on my behalf. They have been the bedrock upon which this work was built and a cushion for me to rebound at every obstacle I have faced.

I have been very fortunate to have Prof. Pravansu Mohanty as my advisor. I am grateful for his invaluable guidance and funding to make this work possible. He has taught me to be an independent thinker and has given me the freedom to explore, diversify and develop my own individuality during the course of this work. I am also thankful for the excellent example he has set for me as a professor and successful entrepreneur

I would like to thank my committee members Prof Zikanov, Prof Reyes and Prof Lee for their assistance in shaping this work. I am grateful to Prof Mallick, Prof Little, Dr Satish, Dr Jagjit, Dr Maridass, Dr Hemang and Dr Ostrom. Thank you all for being a great source of inspiration. I would like to thank faculty and staff at the Electron-beam Microanalysis Laboratory, Ann Arbor (Michigan) for training and use of analytical instruments: Prof Mansfield, Dr Zhongrui (Jerry) Li, Dr Haiping and Dr Kaiping.

Steve Annear has been a source of immense energy and enthusiasm which has greatly boosted my morale.

I am indebted to my brothers in arms a.k.a colleagues: Ram, Praneet, Kang, Sharan, Sathwik and Vincent for their time and support. I would like to thank Mike, Matt and Hunter for help with machining critical components necessary to complete this mission. I would like to thank Eric Krik and Kevin Bean for their efforts to inculcate a safe working culture. A very special thank you to Rich Durant for 24X7 dedicated IT support. I would like to thank Connie, Sherry and Deidra for their help with administrative complexities. I appreciate assistance from Trista for her

help with formatting the dissertation. Research would not have been possible without the shipping department. I would like to thank John and Bonnie for their help.

I would not have made it this far without my friends: I would like to thank Anand, Abishek for being more than family, Hari especially for his committed care and attention when I fell sick, Ram for his extraordinary friendship since freshmen year. I would like to express gratitude to my roommates Hemang and Karthick for all the fun times. I would like to thank my sister Aarthi, my brother-in-law Sriraman and my nephew Anirudhan for their love and motivation.

I would like to thank my beloved wife Aishu. Her support, patience and unconditional love have kept me positive through tough times. I also thank Aishu's parents for their constant encouragement and support.

Thank you grandpa for being a brother, friend and much more. You have always been there for me and I love you always.

## Table of Contents

<b>Acknowledgements.....</b>	<b>iii</b>
<b>List of Figures.....</b>	<b>X</b>
<b>List of Tables .....</b>	<b>xvi</b>
<b>Abstract.....</b>	<b>xvii</b>
<b>1. Introduction .....</b>	<b>1</b>
<b>2. Background.....</b>	<b>6</b>
2.1 The Fe-Mn Alloy system.....	6
2.2 Laser cladding process .....	9
2.3 Cold spray process: .....	10
<b>3. Iron manganese alloy development: Effect of alloying composition on wear and corrosion property .....</b>	<b>22</b>
3.1 Introduction: .....	22
3.2 Experimental .....	24
3.2.1 Precursor preparation: .....	24
3.2.2 Cladding onto 1018 mild steel. ....	24
3.2.3 Cladding on to aluminum alloy: .....	25
3.2.4 Microstructure characterization: .....	25
3.2.5 Electrochemical test: .....	26
3.2.6 Wear characteristics: .....	26
3.3 Results and Discussion.....	27

3.3.1	Microstructure and phase characterization on 1018 steel substrates: .....	27
3.3.2	Microstructure and phase characterization Aluminum 6061 substrate: .....	28
3.3.3	Electrochemical characterization .....	30
3.3.4	Wear testing: .....	34
3.4	Summary .....	36
<b>4.</b>	<b>Coating development strategies .....</b>	<b>37</b>
<b>5.</b>	<b>Cold spray process development of Iron manganese alloys: Numerical modeling and experimental validation.....</b>	<b>39</b>
5.1	Introduction .....	39
5.1.1	Expansion ratio: .....	39
5.1.2	Nozzle throat: .....	40
5.1.3	Nozzle length: .....	40
5.1.4	Standoff distance:.....	40
5.1.5	Nozzle crosssection geometry: .....	41
5.1.6	Nozzle wall friction: .....	41
5.1.7	Powder injection: .....	42
5.1.8	Nozzle contour: .....	42
5.1.9	Computational Fluid Modeling and Visualization:.....	42
5.2	Experimental .....	44
5.2.1	Geometry and Preliminary particle injection evaluation .....	44
5.2.2	Computational domain:.....	45
5.2.3	Microstructure characterization .....	47

5.2.4	Surface temperature .....	48
5.2.5	Wear characteristics .....	48
5.2.6	Bond strength measurements .....	48
5.3	Results and discussion:.....	49
5.3.1	Experimental verification.....	54
5.3.2	Fe-Mn Deposition parameter optimization:.....	57
5.4	Summary: .....	60
<b>6.</b>	<b>Cold spray deposition of Fe-Mn coatings for wear resistant applications: Alloying, Microstructure and Property evolution .....</b>	<b>62</b>
6.1	Introduction .....	62
6.2	Experimental .....	64
6.2.1	Feedstock, substrate and deposition system.....	64
6.2.2	Stainless steel deposition and feedstock annealing:.....	66
6.2.3	Microstructure characterization .....	66
6.2.4	Wear characteristics .....	67
6.2.5	Electrochemical Corrosion test .....	67
6.3	Results and discussion.....	68
6.3.1	Annealing treatment on powders: .....	71
6.3.2	Deposition efficiency: .....	72
6.3.3	Wear testing: .....	73
6.3.4	Open Circuit Potential - Time Measurements .....	74
6.3.5	Potentiodynamic Polarization .....	75



6.4	Summary .....	78
<b>7.</b>	<b>Coaxial laser assisted cold spray deposition of Fe-Mn Alloys: Microstructure characterization – process development.....</b>	<b>79</b>
7.1	Introduction .....	79
7.2	Experimental .....	84
7.2.1	Deposition hardware .....	84
7.2.2	Experimental matrix.....	85
7.2.3	Microstructure characterization .....	86
7.2.4	Laser Power measurement: .....	86
7.2.5	Shear Punch Test: .....	87
7.2.6	Wear characteristics:.....	87
7.2.7	Electrochemical Corrosion test.....	88
7.2.8	Bond strength measurements .....	88
7.3	Results and discussion:.....	88
7.3.1	Surface temperature profile: .....	89
7.3.2	Swipe tests .....	90
7.3.3	Auger Electron Spectroscopy (AES) .....	92
7.3.4	Coating microstructure analysis.....	93
7.3.5	Electrochemical Study – Open circuit potential: .....	96
7.3.6	Wear testing: .....	97
7.3.7	Shear punch test (SPT): .....	98
7.3.8	Bond testing of cold sprayed coatings deposited with different laser powers: .....	99

7.4	Summary .....	100
<b>8.</b>	<b>Application case study: Iron manganese alloy as wear resistant coated aluminum brake rotors.....</b>	<b>101</b>
8.1	Introduction .....	101
8.2	Experimental .....	103
8.2.1	Scaled dynamometer testing: .....	103
8.3	Results and Discussion.....	106
8.3.1	Coating characterization .....	106
8.3.2	XRD characterization: .....	108
8.4	Summary .....	109
<b>9.</b>	<b>General Conclusions and Suggestions.....</b>	<b>110</b>
9.1	Conclusions .....	110
9.2	Suggestions for future study.....	112
9.3	Publications arising from this work .....	113
<b>10.</b>	<b>References .....</b>	<b>114</b>

## List of Figures

Figure 1.1: Growth of use of aluminum in vehicles.....	1
Figure 1.2: Comparison of various deposition processes in terms of particle velocity and temperature [28] .....	3
Figure 2.1: High strength and ductile – High Mn Austenitic steels [12] .....	6
Figure 2.2: Composition and temperature determine the dominant deformation mode [15].....	7
Figure 2.3: (A) schematic of a stacking fault sequence in a FCC structure. (B) HRTEM images show various planar defects in thin film silicon. ISF- Intrinsic stacking fault in which adjacent layers are shifted slightly and Extrinsic stacking fault in which there is an intervening layer between two slightly shifted layers.....	7
Figure 2.4 Laser cladding involves less dilution with base material compared to other laser based alloying techniques and suitable for alloy development [38] .....	11
Figure 2.5: Schematic of the cold spray process 1- Supersonic nozzle, 2- powder feeder, 3- dust insulation chamber, 4- gas heater and 5- Target/Substrate [39] .....	12
Figure 2.6: Effect of particle velocity on deposition.....	12
Figure 2.7: Critical and erosion velocity of different metals calculates from equation [40] .....	14
Figure 2.8: Optimum particle size distribution for cold spraying [41] .....	14
Figure 2.9: Particle velocity over particle temperature with window of spray-ability (WS) and the regime if particle impact conditions [40].....	15
Figure 2.10: Schematic diagram of dependency of deposition efficiency on spray angle [51] .....	16
Figure 2.11: (a) Adiabatic shear localization phenomena (b) and (c) deformation under complete and adiabatic localization [25].....	17

Figure 2.12 (A) Schematic of instability based evolutions of the particle/substrate interface and accompanying formation of interfacial roll-ups and vortices (B) BSE image of Copper coating on aluminum [25].....	18
Figure 2.13: Parameterization using a normalized process grid that combines the discussed characteristics of high-velocity impact, dynamic yield strength, impact pressure, the material bond through the melting temperature of the material sprayed [55].....	19
Figure 2.14: TEM micrograph of an inter-particle triple point in a CS copper coating showing typical microstructural features [13]; (b) TEM micrograph of a CS Ni coating.....	20
Figure 3.1: Experimental setup for Zero Resistance Ammetry (ZRA) study .....	26
Figure 3.2: Cross-section microstructure of the Fe-25Mn-6Al-4Cr-0.2C % wt Specimen (A) BSE Image bringing out compositional contrast (B) EDS map showing with Mn (red dots) showing minimum dilution with base alloy .....	27
Figure 3.3: X-ray diffraction data of select Fe-Mn Alloys .....	28
Figure 3.4: (A) Cladding on aluminum substrate (B) Improved cladding on aluminum after preheating (C) EDS Map shows dilution in the Clad/Aluminum interface .....	29
Figure 3.5: Open circuit potential of Fe XMn YAl 2Cr. Solid lines- 6 Al, Dashed- 2 Al. Blue-35% Mn, Teal-25% Mn, Red-15% Mn.....	30
Figure 3.6: Open circuit potential of Fe XMn 2Al YCr. Solid lines- 4 Cr, Dashed- 2 Cr. Blue-35% Mn, Teal-25% Mn, Red-15% Mn.....	31
Figure 3.7: Open circuit potential data of Aluminum 356 Alloy (Black) Fe-35Mn-2Al-4Cr (Cyan) Fe-35Mn-4Al-4Cr (Green) Fe-35Mn-6Al-4Cr (Red) .....	31
Figure 3.8: Potentiodynamic plot of Fe-Mn Alloys in 0.5wt% NaCl solution .....	32
Figure 3.9: ZRA current density evolution of various samples against aluminum as cathode .....	34

Figure 3.10: Coefficient of friction curves for various alloys A) Fe-Mn-2Al-4Cr (B) Fe-Mn-6Al-2Cr (C) Fe-Mn-2Al-2Cr. Red-35%Mn, Orange-25%Mn, Green-15%Mn .....	35
Figure 3.11: Depth profiles of the worn sections of Fe-XMn-2Al-2Cr-0.2C alloy after wear test.....	36
Figure 5.1: Non dimensional chart showing the effect of standoff distance on deposition efficiency [72] .....	41
Figure 5.2: Deposition profiles with circular and rectangular nozzles .....	41
Figure 5.3: Parameters that affect particle acceleration and cold spray deposition efficiency .....	44
Figure 5.4: (A) Schematic of the computation flow domain (B) Injection geometries evaluated in this study.....	47
Figure 5.5: Grid independence study .....	49
Figure 5.6: Axial gas velocities and temperature profiles across the length of the deposition system.....	50
Figure 5.7: Gas velocity contours (clipped >200m/s) at nozzle exit indicating the operating modes of the nozzle from perfectly expanded to over expanded regimes (A to D) .....	51
Figure 5.8: Particle velocity distribution achieved at 10mm standoff from various nozzles.....	52
Figure 5.9: Spatial velocity distribution of particles from different injection angles at 10mm plane from nozzle exit.....	53
Figure 5.10: Crossection of deposition with nozzles listed in Table 5.1 .....	54
Figure 5.11: Deposition weights of SS316 alloy with different nozzle geometries.....	55
Figure 5.12: XRD data of SS316 coatings with deposited with different nozzle geometries.....	55
Figure 5.13: Coefficient of friction of SS316 coatings deposited with the nozzles in Table 5.1.....	56
Figure 5.14: Worn track profile of SS316 coatings deposited with the nozzles listed in Table 5.1 .....	57
Figure 5.15: Crossection of Fe-Mn <sub>2</sub> alloy cold sprayed coatings sprayed with A) -325mesh and B) - 500mesh powder.....	58

Figure 5.16: Deposition weight and hardness levels of Fe-Mn <sub>2</sub> coatings deposited with as received powder and that sieved with 500mesh. ....	58
Figure 5.17: Crossection of Fe-Mn <sub>2</sub> coatings deposited at different traverse velocities .....	59
Figure 5.18: Deposition weight and bond strength of Fe-Mn <sub>2</sub> coatings deposited at 1→5mm/s,2→10mm/s,3→30mm/s and 4→50mm/s.....	60
Figure 5.19: Surface temperature evolution profile during cold spray deposition of Fe-Mn <sub>2</sub> at scan speed of 10 and 50mm/s .....	60
Figure 6.1: Microstructure and size distribution of the powders .....	65
Figure 6.2: The U of M cold spray nozzle. ....	66
Figure 6.3: Cross section BSE image of cold sprayed Fe-Mn alloy coatings.....	68
Figure 6.4: Bright field TEM image of cold sprayed Fe-Mn <sub>2</sub> alloy coating .....	69
Figure 6.5 XRD patterns from Fe-Mn and SS316 precursor powder and deposited coatings .....	70
Figure 6.6: Size distribution (A) and micro hardness (B) of Fe-Mn <sub>2</sub> powders before and after (dotted) annealing.....	71
Figure 6.7: SEM (A) and XRD (B) of Fe-Mn <sub>2</sub> coatings deposited with annealed powders .....	72
Figure 6.8: Deposition rates of various powders .....	73
Figure 6.9: Coefficient of friction of Fe-Mn alloys .....	74
Figure 6.10: Surface profile of worn track section after wear tests .....	74
Figure 6.11: Open circuit potentials (OCP) of Fe-Mn alloys in 0.5% NaCl solution.....	75
Figure 6.12: Potentiodynamic polarization plot of Fe-Mn alloys in 0.5% NaCl solution .....	76
Figure 6.13: Crossection of samples after Potentiodynamic testing Fe-Mn <sub>1</sub> (A) Fe-Mn <sub>2</sub> (B) Fe-Mn <sub>3</sub> (C) and SS316 (D).....	77

Figure 7.1: (a) Experimental set-up, (b) side view of experimental set-up, (c) movement geometry of coupled cold-spray gun-laser head and (d) top view of the pattern of both cold-sprayed particles and laser spot [101] .....	81
Figure 7.2: External laser assisted cold spray process [108] .....	82
Figure 7.3: Limitation of external laser assisted cold spray process: Beam path obstruction .....	83
Figure 7.4 The U of M Coaxial laser assisted cold spray nozzle [109] .....	84
Figure 7.5: Schematic of Coaxial laser assisted cold spray process used in this study.....	85
Figure 7.6: Laser power attenuation measurement due to powder stream [110] .....	87
Figure 7.7: Beam attenuation at various powder loading/feeding rates .....	89
Figure 7.8: Surface temperature profile during deposition at different laser powers 0 to 300W in 50W increments.....	90
Figure 7.9: SEM images at 52° of ‘Swipe’ tested samples using a coaxial laser beam .....	91
Figure 7.10: FIB crosssection examination of deposited particles at 0 and 500W laser power with coaxial laser beam .....	91
Figure 7.11: AES spectra of the swipe tested Fe-Mn <sub>2</sub> samples at 0 and 500W laser power.....	92
Figure 7.12: Effect of laser power on deposition efficiency of Fe-Mn <sub>2</sub> coatings at optimum cold spray conditions.....	93
Figure 7.13: Effect of laser power on deposition efficiency of Fe-Mn <sub>2</sub> Alloy at non optimum cold spray deposition condition (higher particle loading) .....	94
Figure 7.14: XRD peaks of Fe-Mn <sub>2</sub> deposited coatings at increasing levels of axial laser irradiation .....	95
Figure 7.15: Open circuit potential of Fe-Mn <sub>2</sub> coatings at increasing levels of axial laser irradiation .....	96
Figure 7.17: Coefficient of friction of Fe-Mn <sub>2</sub> coatings at increasing levels of axial laser irradiation.....	97

Figure 7.18: Normalized shear stress vs displacement of Fe-Mn <sub>2</sub> coatings with and without laser assistance .....	98
Figure 7.19: Bond strength of Fe-Mn <sub>2</sub> coatings deposited at different laser powers and different powder loading rates.....	99
Figure 7.20: Proposed schematic highlighting the effect of laser power density .....	100
Figure 8.1: Fuel savings based on 10% reduction of initial weight [21] .....	102
Figure 8.2: A schematic of the brake tester arrangement used for testing in the current study .....	104
Figure 8.3: Maximum temperature vs Cumulative stop.....	105
Figure 8.4: Aluminum pucks with cold sprayed Fe-Mn <sub>2</sub> coatings before and after testing .....	106
Figure 8.5: Crossection of cold sprayed Fe-Mn <sub>2</sub> coatings after testing in the scaled dynamometer.....	107
Figure 8.6: Crossection of laser clad Fe-Mn <sub>2</sub> composition after testing .....	108
Figure 8.7: XRD patterns of coating before and after the scaled brake testing .....	108



## **List of Tables**

Table 3.1: Laser clad deposition parameters.....	25
Table 3.2: Ecorr and Icorr obtained from polarization curves by Tafel extrapolation method.....	33
Table 4.1: Deposition routes to achieve iron-manganese coatings on aluminum.....	38
Table 5.1: Nozzle geometries evaluated in this study.....	45
Table 5.2: Composition of Fe-Mn powders (balance Fe) .....	47
Table 5.3: Comparison of injection pressure and obtained velocity .....	54
Table 6.1: Composition of Fe-Mn powders (balance Fe) .....	65
Table 6.2 CNO analysis results of the Fe-Mn <sub>2</sub> Alloy powder.....	71
Table 6.3: Tafel interpolated corrosion potential and corrosion current density .....	77
Table 7.1: Deposition parameters used in this study.....	85
Table 7.2: Composition of Fe-Mn alloys used in this study .....	85

## **Abstract**

Aluminum alloys enable lighter fuel efficient cars making them attractive for automotive applications but they exhibit poor tribological properties. Industrial coatings practices for wear protection are not suitable to protect aluminum as they lack compatible material and feasible manufacturing processes. The purpose of this research is hence twofold: development of a low cost material and a suitable manufacturing process to improve wear resistance of widely used Aluminum alloys

The material was iteratively developed from existing Iron manganese (Fe-Mn) alloys which are used extensively in mining applications. Influence of aluminum, chromium and carbon were studied in order to improve both corrosion and wear resistance of the alloy. A laser cladding process was utilized to create desired alloys. Studies were then conducted to understand phase, wear and corrosion property evolution. It was found that at an optimum composition, the material would barely form a galvanic couple with base aluminum alloy. Wear resistance of the alloy was found to be superior to that of conventional stainless steel.

The Fe-Mn alloys are one of the hardest steels to work with. They are also susceptible to oxidation and depletion of manganese during processing. Hence existing coating processes are not suitable for deposition. To this end, cold gas dynamic spray (CS) was utilized to deposit Fe-Mn alloys. In order to improve CS deposition efficiency, the process was at first numerically modeled with experimental feedback. In the next step, a novel coaxial laser assisted cold spray process was utilized to enhance deposition. The improved process resulted in Fe-Mn coatings with multifold improvement in deposition rate and bond strength at significantly lower powers densities than competing complex technologies. The influence of laser on bonding mechanism

was then studied through a splat level analysis and auger spectroscopy was utilized to understand variations in chemical composition due to the laser irradiation.

As a proof of concept, Fe-Mn alloy was coated onto aluminum pucks and evaluated in a scaled disc brake test environment. The material system and deposition process were found suitable and hence present a potential solution to manufacture coated brake rotors.

## 1. Introduction

With high specific strength, ease of manufacturing and priced well below titanium alloys; aluminum alloys represent a viable solution to achieve weight reduction for automotive applications. As a result, the switch to aluminum based parts has been consistently growing (Figure 1.1). The modest gains in emissions and fuel efficiency per vehicle translate significantly given billions of vehicles worldwide. Till date, aluminum has replaced components that are not prone to wear and abrasion. To further sustain this growth, research is well underway to engineer aluminum for use in more demanding settings, ensuing safer, efficient vehicles with reduced carbon foot print. The progress in precipitation strengthened aluminum alloys [1]–[3], development of reliable and cost effective production of aluminum matrix composites[4], [5] and protective coating formulations[6], [7] have been instrumental towards this goal.

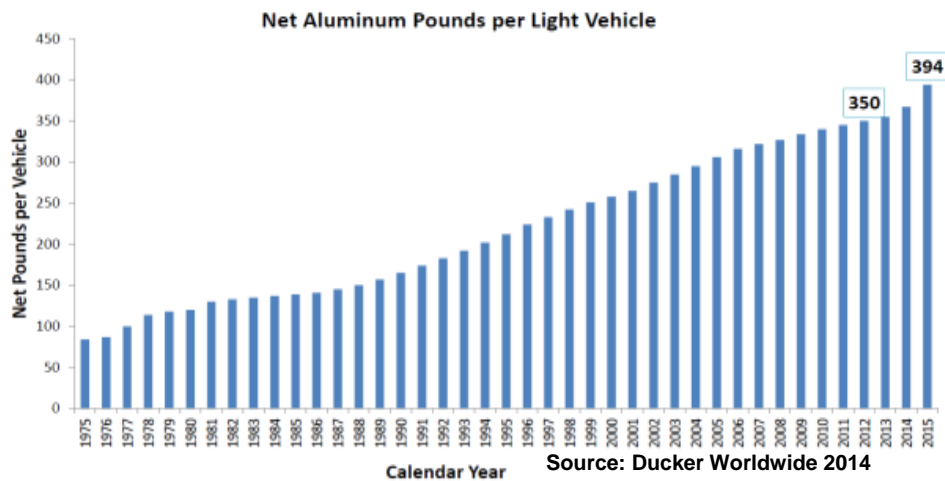


Figure 1.1: Growth of use of aluminum in vehicles

In this study an Iron manganese alloy composition is developed as coating material to enhance wear resistance of aluminum components. Although coatings are a straightforward solution; certain complexities prevent the use of existing established manufacturing routes. These stem from issues related to physical and electrochemical property: Lower melting point of aluminum leading to part distortion, formation of harmful intermetallics and galvanic corrosion with coating material. Till date coatings on aluminum alloys have hence been limited to its native oxides, nitrides [8]–[10] and exotic DLC style materials [11]. Hence, there is scope for tailored coating material and deposition processes suitable for aluminum alloys.

The iron-manganese binary (Fe-Mn) and ternary (Fe-Mn-C) alloy systems possess a distinctive combination of ductility and strength [12]–[15]. Presence of manganese is known to induce transformation or twinning of the austenite phase resulting in unique work hardened material. By completing substituting nickel, austenitic Fe-Mn, which are widely used in automotive industry as TRIP (TRansofmation Induced Plasticity) and TWIP (TWinning Induced Plasticity) steels, represent a potential low cost wear resistant materials. The presence of manganese in these alloys lowers the corrosion potentials [16] to ranges similar to that of Aluminum alloys. Additionally slight modifications in the electrochemical property by varying additions of Aluminum and Chromium [16]–[19] have been reported. Still more, Austenite has a coefficient of thermal expansion closer to that of Aluminum alloy.

The Fe-Mn alloy is complex; the effect of its alloying elements on strength and deformation related properties are nonlinear. These emanate from variations in its stacking fault energy [17], [20], [21]. The effect on corrosion property of the alloy however is more linear. Aluminum and Chromium have enhanced corrosion property of the alloy [16], [22]. For the application as mechanical property, phase and corrosion resistance are in question, select Fe-Mn alloys are experimentally studied. Laser cladding was used as a rapid manufacturing tool to melt predetermined mixture of Fe-Mn alloy for subsequent testing. One key advantage of laser cladding is that the solidification rates achieved in laser cladding are similar to that achieved during gas atomization of powders that are commonly used to manufacture precursors for coating deposition processes.

With recent advances in low temperature coatings processes such as cold gas dynamic spray, coatings can be achieved with little or minimal melting (Figure 1.2). Here, as will be described in

detailed in the following chapters, desired material in the form of micron sized powders are accelerated at supersonic velocities to create a splat. During this course the particle does not experience heating and reaches the substrate in as received condition. Upon impact, the kinetic energy of the particle translates into plastic deformation. Frictional heating that will occur is beneficial. It enables plastic deformation in the material to overcome its strain rate hardening behavior. With no melting and oxidation proof processing temperatures, virginity of deposited materials is preserved[23]–[27]. Cold spray opens up new avenues to deposit material in a cost effective way.

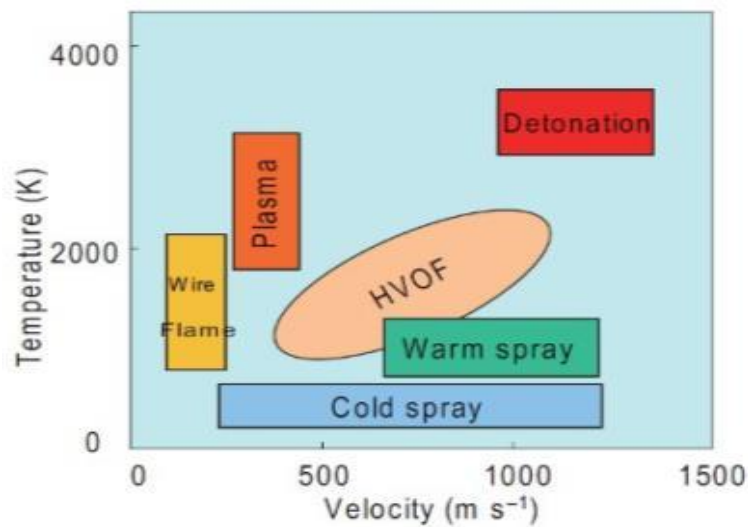


**Figure 1.2: Comparison of various deposition processes in terms of particle velocity and temperature [28]**

In order to improve deposition quality of cold spray process, a co-axial laser assisted cold spray process is developed. Studies have shown an increase in substrate temperature is beneficial for cold spray [29]–[31]. The laser beam is designed to improve deposition quality along similar lines. Through appropriate lenses, the beam is shaped to seamlessly integrate with inner profile of the cold spray nozzle. The effect of laser beam is studied on macro-structural properties (bond strength, wear and corrosion) as well as on individual particle impact events.

The body of the study is divided into following chapters. A concise review of relevant literature is presented in Chapter 2. Chapter 3 begins the study with development of numerous blends of Fe-Mn alloy. The laser cladding was used to formulate select alloying combinations. Wear and electrochemical analysis is carried out to create a library of laser clad Fe-Mn alloys

The rest of the chapters discuss coating deposition. Cold spray is a solid-state approach to deposition and is well suited for current material system. Preliminary depositions with other thermal approaches are summarized in chapter 4. Unlike conventional thermal spray processes, the nozzle geometry forms the heart of the cold spray process. For a given processing gas conditions, nozzle geometry optimization is essential to achieve large gas velocities. Hence an optimization of nozzle geometry and effect of processing gas conditions was performed and presented in chapter 5. Here a numerical analysis is carried out to optimize two critical factors – expansion ratio and powder injection angle. Numerical results were then compared with experimental findings.

Findings on Fe-Mn coating parameter optimization are summarized in Chapter 6. The effect of deposition standoff, traverse velocity and particle size is studied. Based on the results, a deposition mechanism was proposed which agrees with literature. Chapters 7 focusses on development of coaxial laser assisted cold spray deposition process. A standard sequence of preliminary adjustments to laser power was followed by micro-dissection of individual splats post deposition. With the laser assistance, an increase in jetting was observed. Experiments were conducted with varying laser powers and traverse rates to verify the effect of substrate temperature and to identify a deposition sweet- spot. Wear, Electrochemical and Bond tests were conducted. These provide a numerical means to evaluate against current cold spray process.

As a separate investigation, improvement in cold spray deposition efficiency is realized through annealing of powders. Cold spray process relies exclusively on plastic deformation. Hence yield strength of starting material will affect deposition. Annealing powders result in softening of material through grain coarsening and recovery from cold work. It homogenizes the physical property of the powder. The effect of enhanced deposition rate is compared to final coating properties such as strength, wear and corrosion. Given the cumbersome annealing process, risk of sintering and the very objective of avoiding heat treatment of sprayed materials, the investigation seeks to understand if annealed powders represent a feasible pre-treatment for cold spray deposition.

Chapter 8 focusses on cold sprayed Fe-Mn coatings are then tested for durability in scaled brake testing environment. The phase stability of the material system and physical integrity of the

coating are assessed through analytical means. The study ends with note. Important conclusions are summarized along with suggestions for future work in Chapter 9.



## 2. Background

A concise literature review is presented on topics that are of interest to this study

### 2.1 The Fe-Mn Alloy system

Since its discovery in 1888 by Sir Robert Hadfield, the Fe-Mn-C Alloy system has gained considerable interest for its high strength and ductility properties[32]. The co-existence of otherwise mutually exclusive property has revived the interest in the production of cold-stamped parts used largely by car-manufacturers. Complex and multiple deformations occurring in this system result in its excellent mechanical properties. These deformations are dependent on the alloy composition and temperature as sketched in while the effect of the later is straight forward, the composition determines the stacking fault energy (SFE) and critical resolved shear stress (CRSS) of the alloy.

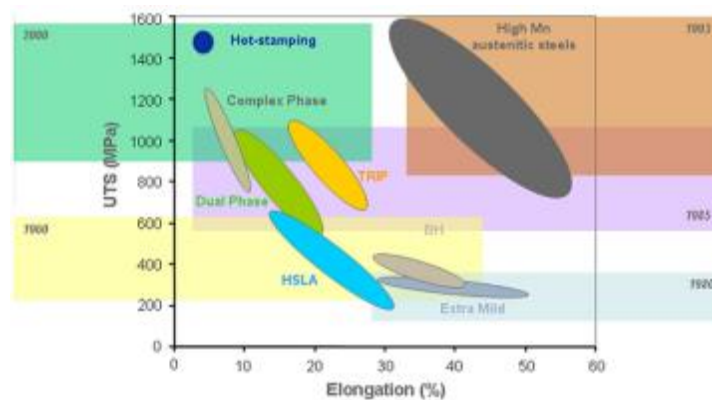


Figure 2.1: High strength and ductile – High Mn Austenitic steels [12]

SFE represents the energy required for creating the defect and the dislocation distance between partial dislocations surrounding the defect. The CRSS represents the stress concentrations required to extend the initial stacking fault. At very low SFE ( $<10\text{mJ/m}^2$ ) the transformation into bcc  $\alpha'$  phase followed by  $\gamma$  to  $\epsilon$  ( $<20\text{mJ/m}^2$ ). At SFE's between 20 to  $60\text{mJ/m}^2$  the formation of

twinning is favored. Further increase in SFE results in partial and finally perfect dislocation motion (Figure 2.2).

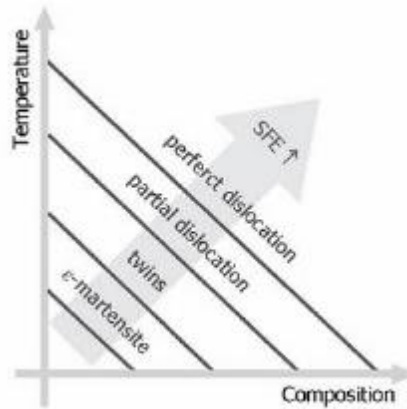


Figure 2.2: Composition and temperature determine the dominant deformation mode [15]

Role of stacking fault energy:

Stacking faults basically interruptions in the naturally occurring stacking sequences that occur in crystalline materials (see Figure 2.3). Stacking faults are the direct and observable result of dislocations of crystallographic defects or irregularities in a crystal structure. Because stacking faults decrease the amount of order within a crystal structure, they carry an associated energy penalty with them.

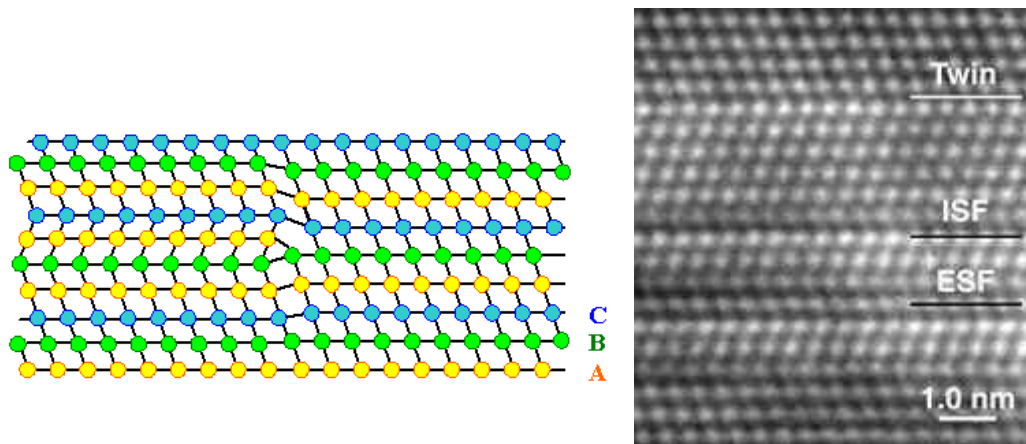


Figure 2.3: (A) schematic of a stacking fault sequence in a FCC structure. (B) HRTEM images show various planar defects in thin film silicon. ISF- Intrinsic stacking fault in which adjacent layers are shifted slightly and Extrinsic stacking fault in which there is an intervening layer between two slightly shifted layers

In many occasions, a perfect dislocation—which would yield a single stacking fault—dissociates into two partial dislocations, which tend to repel each other. This creates a stacking fault with a particular width, instead of the infinitesimally thin (a single plane of atoms thick) stacking fault associated with perfect dislocations. The width of the stacking fault in this case is directly attributed to the value of the stacking fault energy (SFE) of that particular material. There must be an energy balance between the repulsive force that exists between two separate partial dislocations, and the attractive force which exists as a consequence of the surface tension created by the stacking fault itself. The net quantity of energy which remains after the summation of these opposing forces is the quantitative value of the SFE of the material in study. More simply put, SFE is the energy penalty which is paid to create a stacking fault in a crystal structure—a material property which is unique in every material.

When SFE is low, such as in Fe-Mn alloys, wider stacking faults occur because there is a smaller energy penalty to be paid for the associated defect in the crystal structure. These defects in the crystal structure prevent the movement of dislocations via the processes of cross-slip and climb—thus low SFE materials have the capacity to become very hard and brittle when cold worked.

When SFE is high, such as in aluminum, it becomes exceedingly difficult for a perfect dislocation to dissociate into two partial dislocations, and as such the material tends to deform only via dislocation glide. If dissociation into two partial dislocations does occur, then the stacking fault tends to be very thin, and carries a significant amount of energy within the fault. Because these materials leave cross slip and climb relatively unhindered as manners to achieve dislocation motion, cold work does not impart as strong of an effect on the hardness and brittleness of the material as seen in low-SFE materials.

#### Effect of alloying elements

The Fe-Mn-Al system has been thoroughly investigated to replace conventional Ni-Cr based stainless steel[19]. The work hardening property of the Mn based ferrous alloy system results in plastic deformation under impact loading with abrasion or erosion. This mechanism obviates the possibility of brittle fracture and spalling [33] Manganese is an austenite former and a cost effective replacement Nickel. Disadvantages of manganese are the tendency to segregate forming

beta manganese and its high affinity for oxygen at higher temperature[34]. This often results in the alloy with depleted Mn content. This alters the stacking fault energy leading to formation of martensitic phases which could be unwarranted and detrimental. Aluminum also helps increase the SFE. Therefore it stabilizes the austenitic phase and prevents formation of martensitic phases. At Higher levels of aluminum, the formation of a continuous passive layer has been shown. Silicon is known to reduce SFE and promotes  $\gamma$  to  $\epsilon$  transformation. Silicon is often added as it improves fluidity during casting and also increases strength by solid solution alloying. Chromium Additions to Fe-Mn Alloys have been widely studied as means to improve the corrosion properties of this alloy[15], [35]. Chromium also increases the yield strength or the flow stress thus enhancing wear property [36]. There is discrepancy on the effect of the stacking fault energy by Chromium. Some prove that it increases while the others prove otherwise. Carbon and Nitrogen are two other important elements widely researched in Ni-free austenitic alloys. Both these elements have higher solubility in austenite matrix. The disadvantage of these interstitials is precipitation. The maximum amount of carbon that can be added was limited to 1.2% [13] Nitrogen up to .22wt% has shown to reduce work-hardenability [37]. Carbon has been shown to precipitate at 4500C [14].Carbon was however added as it affects the critical resolved shear stress which is necessary for twinning [13], [20]. In addition to the above, it was found that aluminum delayed the precipitation of carbides and promoted formation of pearlite. It also reduced the frequency of mechanical twins indicating an increase in stacking fault energy [21].

Development and optimization of Fe-Mn alloy will be as follows: The role of manganese is to ensure the stability of gamma phase at all temperatures and compensate for losses during oxidation. The role of aluminum and chromium is to control the corrosion property and reduce galvanic coupling with A356 aluminum alloy. The role of carbon will be to enhance twinning tendency. Any precipitation will result in strengthening of the alloy and could possibly introduce lubrication as free graphite and prevent galling.

## **2.2 Laser cladding process**

Laser cladding was employed in this study as a combinatorial method to develop Fe-Mn Alloys. Here a laser beam acts as the heat source to deposit a thin layer of material on a substrate. The

desired material can be introduced in the form of powder or wire. Further these can be introduced in-situ during deposition through a delivery system or preplaced on the substrate. Of these methods, deposition via powder injection is most effective. The laser beam melts the powder particles to create a thin layer on the substrate. Coaxial powder injection is widely used to fabricate layer by layer 3 dimensional parts. Through control of process powder, traverse rate and spot size various microstructures can be obtained. As presented in Figure 2.4, for the purposes of present study base material dilution in the clad is avoided.

During laser cladding, two fundamental physical phenomena occur [38] These are as follows:

Heat transfer: Based on absorption of the laser beam: A substantial portion is absorbed by the substrate which creates a melt pool. A smaller portion of the laser beam is absorbed by the powder particles which then enter the melt pool. Hence this can be expressed by a heat conduction equation

Fluid flow in the melt pool: In the melt pool surface tension drives the fluid flow (marangoni convection) due to this melted powder are rapidly mixed in the melt pool. These can be described in mass transfer phenomena.

The density and bonding of the cladding is controlled by the energy delivered by the laser beam. The high temperature gradient causes strong convective forces the help the liquid phases rapidly mix and become homogenous. This forms the basis of dense claddings upon solidification.

### **2.3 Cold spray process:**

Discovery:

The cold gas dynamic spray coating process was discovered in mid 1980s by a group of russian scientists performing studies with compressed gas at supersonic velocities. The phenomenon of cold spray was then accidentally discovered when the seeding particles formed a coating with extraordinary adhesion. This cold spray phenomenon only occurs at certain particle size and velocity range. Since then enormous amount of research has been done. The ability to achieved deposition in lower temperatures without melting has attracted significant efforts into commercialization of the process. Cold spray is widely used to coat ductile as well as temperature sensitive materials such as titanium, tantalum alloys.

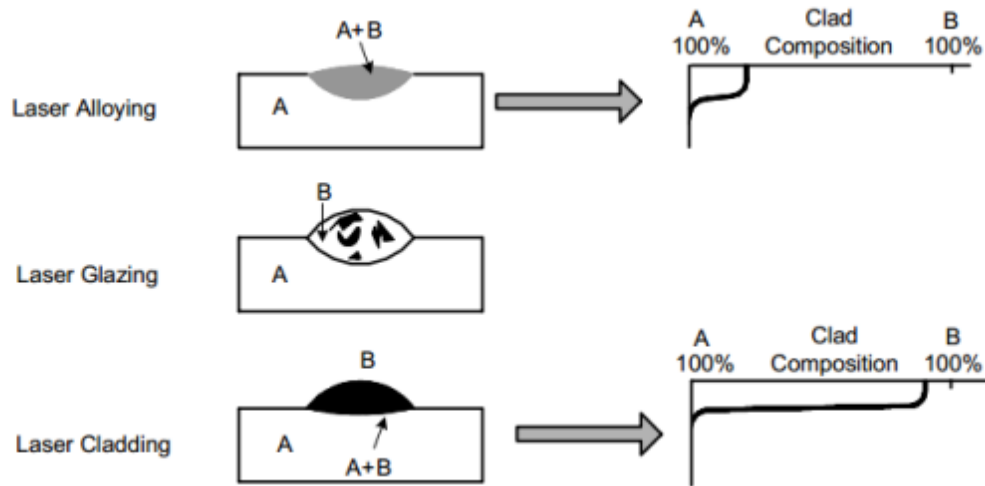


**Figure 2.4 Laser cladding involves less dilution with base material compared to other laser based alloying techniques and suitable for alloy development [38]**

The cold spray process presents unique system for niche applications in that the lack of high temperature heat source and undesirable melting that usually go with flame, plasma, hvof arc spray process. Hence the process is suitable for oxidation resistant materials,

The cold-spray system: General discussion

Figure 2.5 shows schematic of the cold gas dynamic spray setup. Although the system can operate without gas heating, temperatures of about 600degC are commonly used in the process. Pressurized gas is heated and enters a convergent divergent- de Laval style nozzle. The exit gas velocity reaches about 1200m/s which accelerate powders to create a solid-state splat. The powder through a metering device can be introduced upstream or downstream. Depending upon the loading rate Powder particles attain velocities well over 500m/s. combine the high temperatures of the gas used in the process do not melt the particles. Rapidly accelerated by the gas flow, powder particles experience short residence time in the nozzle. Further, the gas rapidly cools in the expansion region. Despite these conditions, neither substrate nor powder particles are at room temperature during deposition.

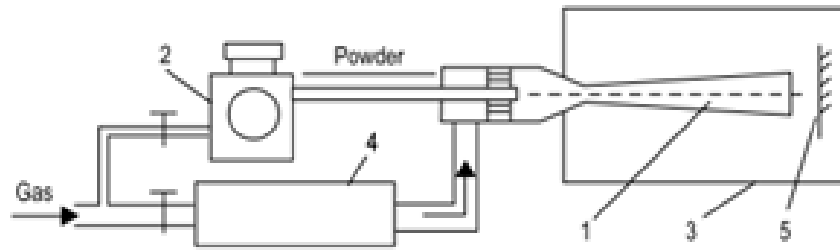


**Figure 2.5: Schematic of the cold spray process 1- Supersonic nozzle, 2- powder feeder, 3- dust insulation chamber, 4- gas heater and 5- Target/Substrate [39]**

Successful deposition/impact: Concept of critical velocity

From experimental determination for successful deposition, the deposited powder particles must exceed a particular critical velocity (see Figure 2.6). This velocity is dependent on processing conditions and deposited material. Below the velocity, the deposited powder is unable to undergo mutual deformation with the substrate. During rebound, depending on its momentum (based on its size) it can lead to detrimental abrasion of the substrate or previously deposited layer. Again, if the velocity exceeds the critical velocity it results in excessive jet formation preventing useful deposition. This is caused by a hydrodynamic phenomenon [40]. The higher the critical velocity of the system, higher pressure or temperatures will be required.

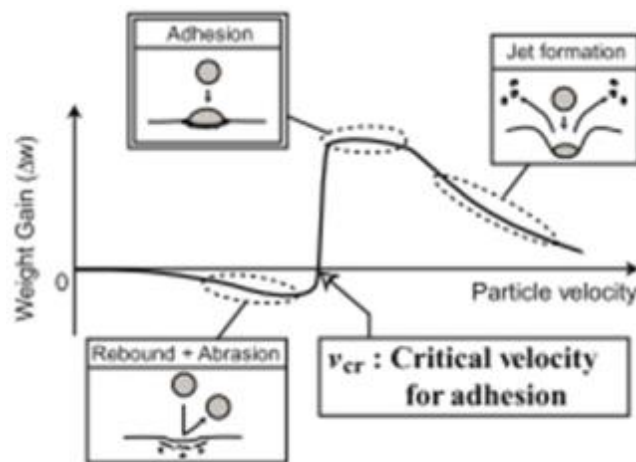


**Figure 2.6: Effect of particle velocity on deposition**

Assadi et al [24] experimentally derived the critical velocity by performing single impact studies of several materials. Shown in Figure 2.7, some materials require higher velocity than the others. Based on these measurements, an empirical equation was formulated to determine critical velocity (Eq 2.1).

$$v_{cr} = 667 - 14\rho + 0.08T_m + 0.1\sigma_u - 0.4T_i \quad \text{Eq. 2.1}$$

Where,  $\rho$  the mass density in g/cm<sup>3</sup>,  $T_m$  is the melting temperature in °C  
 $\sigma_u$  is the ultimate strength in MPa;  $T_i$  is the initial particle temperature in °C

While the formula presents a generalized number, anomalies exist with certain materials such as tantalum; will be explained in continuing sections of the current chapter. It also doesn't take into particle size, material properties, and thermal history of the powder. Further the effect of alloyed materials alter stress-strain relationship significantly are neglected for simplicity. These include strain hardening, strain-rate hardening and thermal softening. Heating from the frictional plastic viscous dissipation was assumed adiabatic. The model was developed particularly for copper for which the author obtained good agreement with experimental results.

Schmidt et al [40] have proposed another technique to calculate critical velocity. By considering the impact dynamic effects, the energy balance and a weighting factor for the velocities to arrive at the following equation (Eq 2.2) Here calibration factors (respectively F1 and F2) are calculated by correlating critical velocities on the basis of materials properties with experimentally values. This results in F1 = 1.2, F2 = 0.3.

$$v_{crit}^{th, mech} = \sqrt{\frac{F_1 \cdot 4 \cdot \sigma_{TS} \cdot \left(1 - \frac{T_i - T_R}{T_m - T_R}\right)}{\rho} + F_2 \cdot c_p \cdot (T_m - T_i)} \quad \text{Eq. 2.2}$$

where,  $c_p$  is the specific heat (J/K.kg),  $T_i$  the impact temperature (K),  
 $T_m$  the melting temperature (K),  $T_R$  the reference temperature (293 K),  
 $\sigma_{TS}$  the tensile strength (MPa) and  $\rho$  the specific mass (kg/m<sup>3</sup>).

The effect of particle size on critical velocity is presented in Figure 2.8. As a general rule, very fine powders experience globalized temperature rise preventing flow localization hence requires higher velocity to deposit [41].



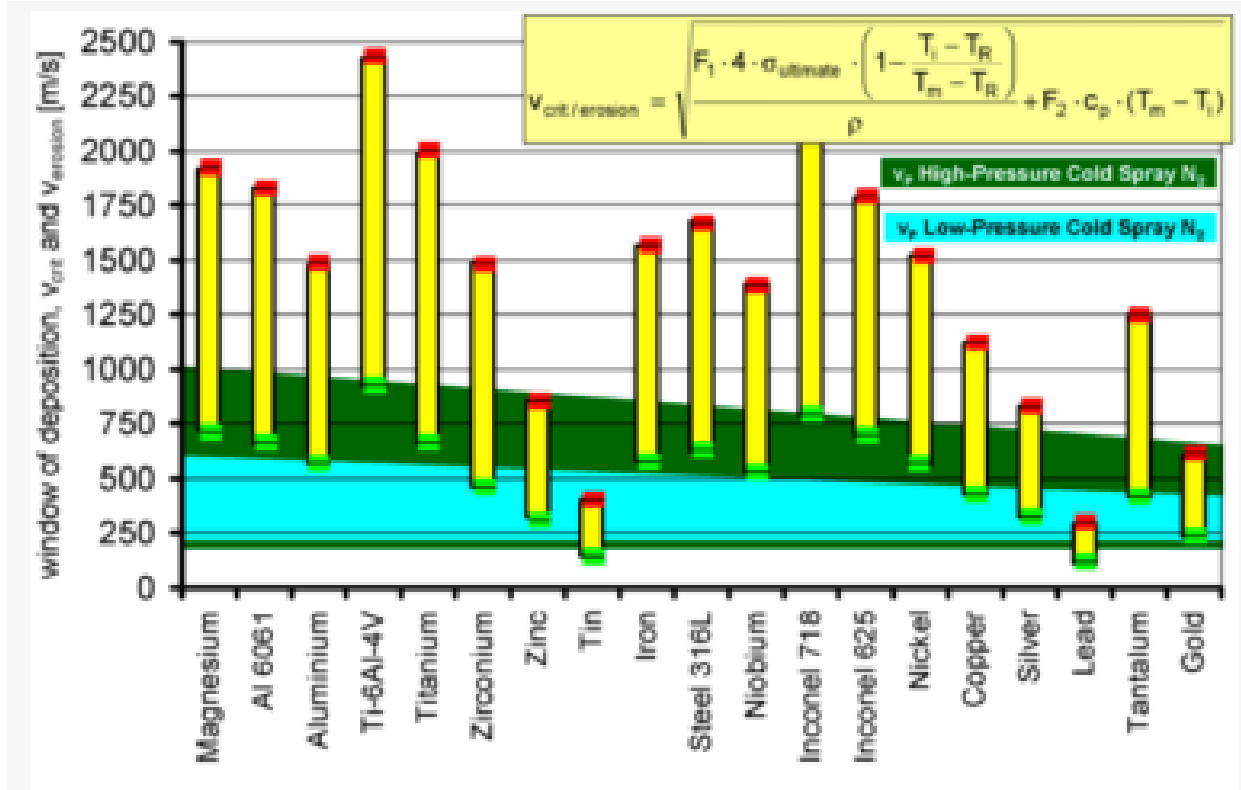


Figure 2.7: Critical and erosion velocity of different metals calculates from equation [40]

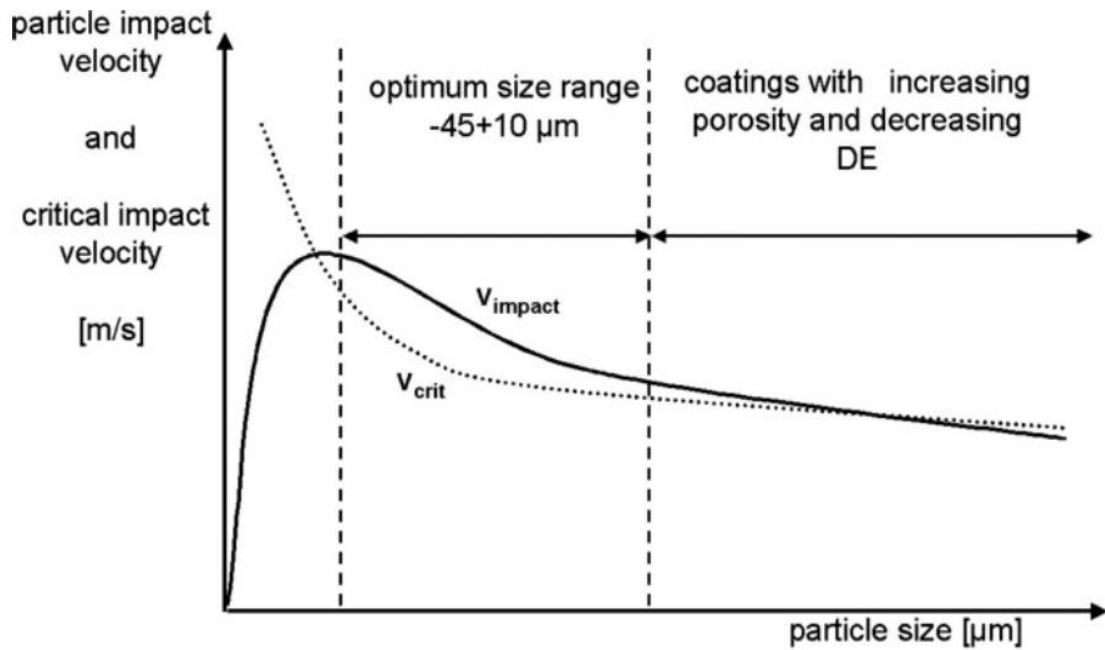
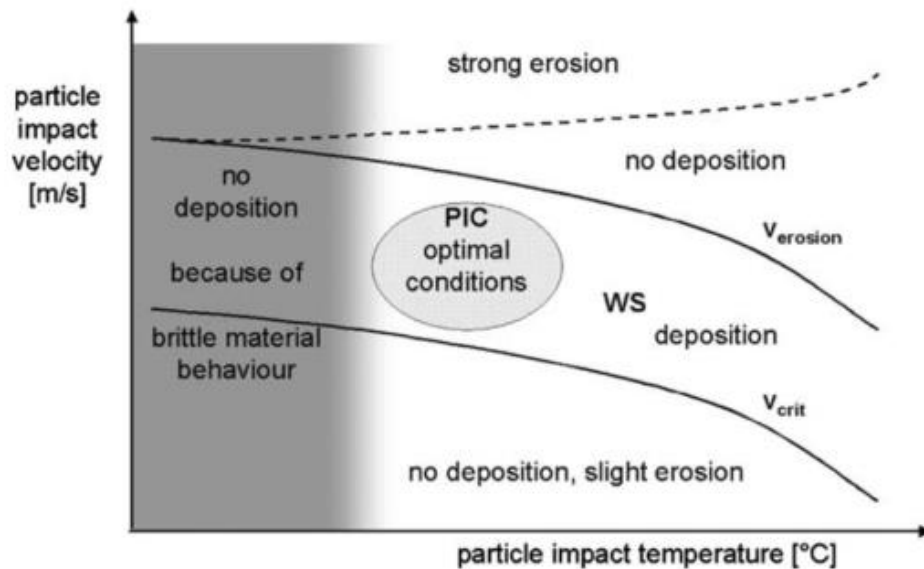


Figure 2.8: Optimum particle size distribution for cold spraying [41]

### Role of Impact and substrate temperature:

The effect of substrate temperature has been investigated and found to have a favorable effect on deposition [29]–[31], [42]–[44]. This was realized from the fact that longer spray time and higher gas temperature resulted in increase of deposition efficiency. King et al confirmed that the substrate preheating promoted the occurrence of interfacial melting. Schmidt [40] pointed out that impact temperatures must be higher than the ductile to brittle transition temperature of the material. Figure 2.9 describes the WS (window of spray ability with respect to particle impact velocity and impact temperature).



**Figure 2.9: Particle velocity over particle temperature with window of spray-ability (WS) and the regime if particle impact conditions [40]**

It is believed that for successfully bonding to occur, the substrate must undergo some form of activation [45]. Substrate roughness has shown to be beneficial for cold spray, but the technique used to achieve the roughness such as grit blasting results in contamination of the surface and leads to unreliable bond strengths. Is it still unclear if surface roughness or increase in residual strength due to peening effect is beneficial of cold spray [46].

### Role of spray angle on deposition efficiency:

Given the shearing action during cold spray particle adhesion, several authors have investigated the effect of spray angle [47]–[51]. The mechanism proposed by Li et Al is shown in Figure 2.10. The deposition efficiency is the highest when the particle makes a normal impact. At other angles, the velocity of the particle in normal direction is reduced. As these velocities go below critical velocity, the efficiency is reduced. At too shallow angles, deposition fails to occur.

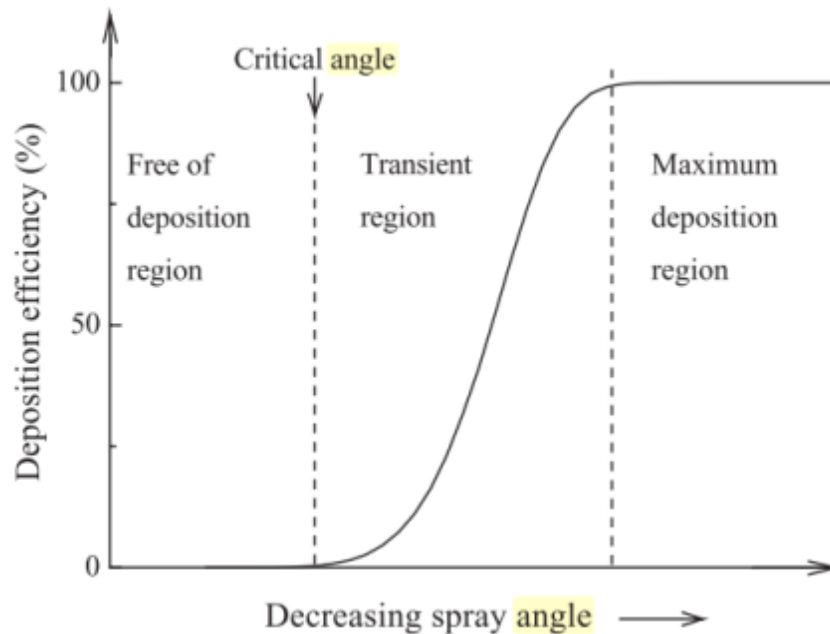
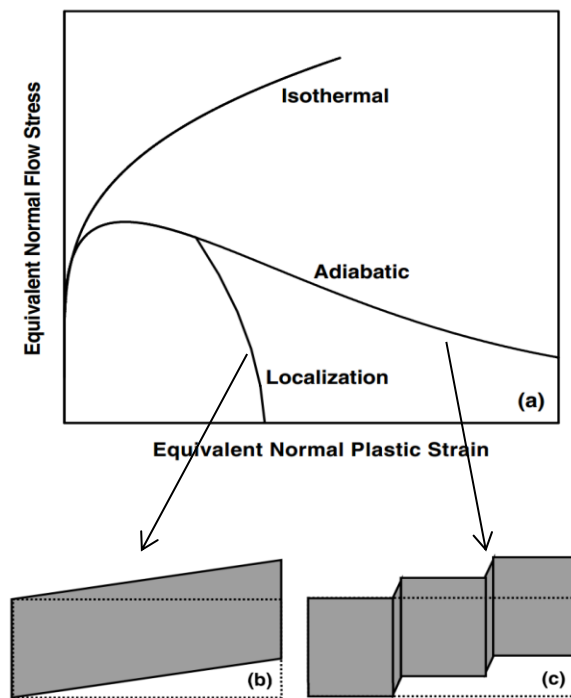


Figure 2.10: Schematic diagram of dependency of deposition efficiency on spray angle [51]

Cold spray process maximum theoretical maximum deposition efficiency:

Studies have shown that 100% deposition efficiency is not possible in cold spray. The deposited powder is poly-dispersed, meaning they have a size distribution and are not uni-sized. Smaller powder is often blown away or may not reach at preferred angle(90deg) and require higher velocity [52] Initial layer of material cannot be deposited. Break away layer is required [53] Particle velocity is not uniform everywhere and maintains a Gaussian distribution (circular nozzles)thus a constant fraction of particles will not exceed critical velocity [54]

Falling in the lower strain rate regimes of shock or explosive deformation, cold spray deformation mechanism follow similar adiabatic mechanisms. The well agreed deformation mechanism in cold spray process is based on adiabatic shear instability causing localized (in the order of micrometer) deformation of the particle. This plastic deformation results in creation of mutually confirming surfaces to create features with high cohesive or adhesive strengths. During impact the particle on to the substrate the kinetic energy of the particle is converted to thermal energy which results in heating of the particle. This causes a localized softening of the powder and results in plastic deformation (Figure 2.11).



**Figure 2.11: (a) Adiabatic shear localization phenomena (b) and (c) deformation under complete and adiabatic localization [25]**

The ultra-high strain rate undergone by the powder during impact is believed to result in the plastic deformation. The mechanism of deposition of cold spray is widely accepted to be related to adiabatic shear instability or shear localization. While the material work-hardens proportionally with increasing shock pressure, beyond a certain threshold this is insufficient time for heat dissipation during plastic deformation. This results in adiabatic conditions causing local temperature rise and related softening resulting in a reduction in yield strength.

Hence the velocity of the particle is a determining factor to predict successful deformation.

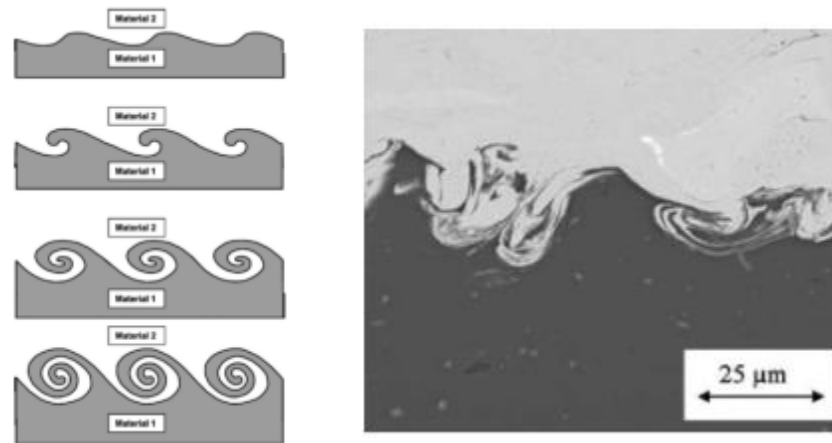


**Figure 2.12 (A) Schematic of instability based evolutions of the particle/substrate interface and accompanying formation of interfacial roll-ups and vortices (B) BSE image of Copper coating on aluminum [25]**

Vleck [55] et al have applied shock studies, equation of state and rankine hugoniot theory to understand cold spray deformation. They calculated that melting cannot occur during deformation of pure metals as the localized temperature is conducted into a global particle temperature. Due to plastic deformation playing a key role in deformation, there is a widely accepted notion that only ductile materials can be deposited. Yet, materials like tantalum, niobium which has high melting point and not necessarily ductile deposit easily. This is because of lack of strain rate hardening in tantalum. Tantalum is also denser hence has higher momentum at impact. In terms of determining spray ability, Vleck suggested that peierls stress and stacking fault energy of the material play a key role in determining eligibility of a material for deposition. The peierls stress stresses determines the force required moving dislocation and the stacking fault represents an estimate of how easy it is to move the dislocation or dislocation density. The mechanism of material eligibility proposed by Vleck is shown in Figure 2.13

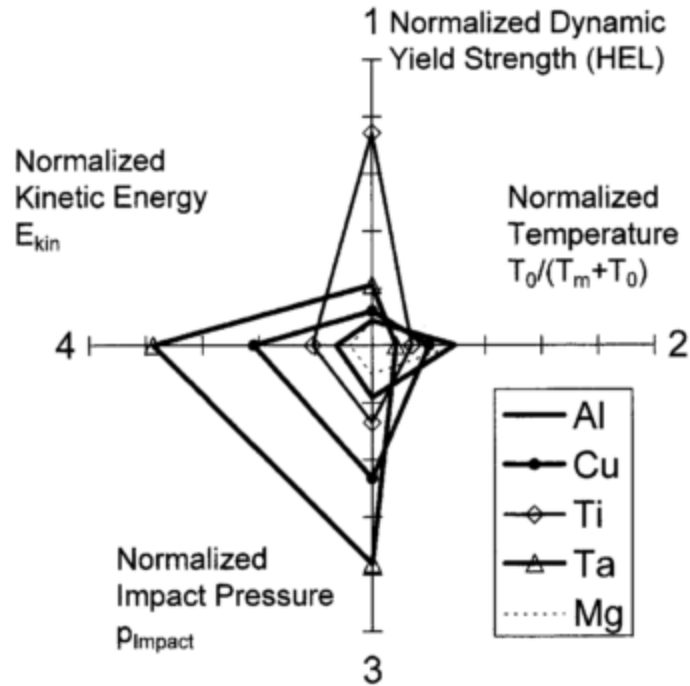


**Figure 2.13: Parameterization using a normalized process grid that combines the discussed characteristics of high-velocity impact, dynamic yield strength, impact pressure, the material bond through the melting temperature of the material sprayed [55]**

Microstructure characterization of cold sprayed coatings (SEM, TEM, Diffraction, EBSD)

In cold spray, due to high-velocity impact, the particles experience very large strains (up to 10) and strain rates (up to  $10^9/s$ ) in the interfacial regions, leading to work hardening, i.e. the generation of dislocations and other defects. At the same time, the temperature rises, leading to the restoration processes of recovery and recrystallization. Recovery involves the reduction of the dislocation density without any other change in the microstructure. Dynamic recovery occurs concurrently with dislocation generation, i.e. during plastic deformation, whereas static recovery occurs after deformation when the metal is in the unloaded condition. Dynamic recovery happens in metals with high stacking fault energy (SFE) such as aluminum. Recrystallization leads to dislocation free structures by the formation of new grains by nucleation and growth into the deformed or recovered microstructure. In materials with low or medium SFE such as copper or stainless steel, in which recovery processes are relatively slow, dynamic recrystallization could take place during the deformation. As implied from the above description of recovery,

recrystallization can occur dynamically, or statically. Static recrystallization can also occur during post-deformation heat treatment, i.e. annealing [56]

The evolution of grains and subgrains within the particle during cold spray using TEM has been reported in several studies. Borchers et al [56] have observed highly non uniform features in nickel and copper particles. They notice elongated and equiaxed grains and sub grains with grain size ranging from a few microns to a few hundred nanometers. These reveal a dynamic recrystallization (region B) occurring in the form of grain refinement as shown in Figure 2.14. Evidence of static recrystallization can also occur as shown in region D

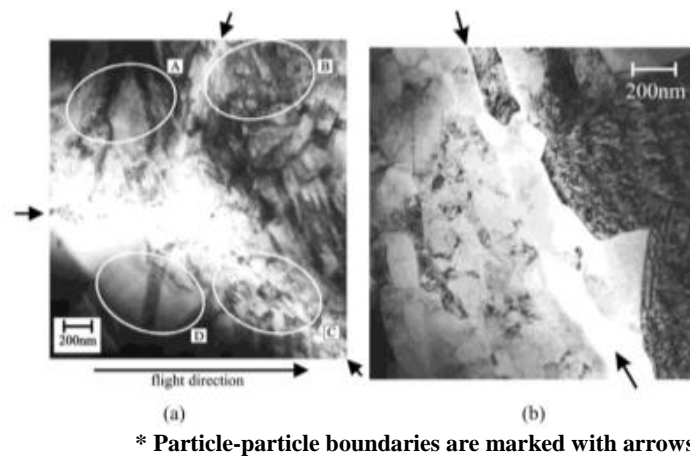


**Figure 2.14: TEM micrograph of an inter-particle triple point in a CS copper coating showing typical microstructural features [13]; (b) TEM micrograph of a CS Ni coating**

Comparing pure copper, nickel and aluminum samples processed, respectively, by cold spray [56], cold rolling, hot rolling, and equal channel angular pressing (ECAP), it was found that the microstructure of cold sprayed samples have the following characteristics: 1) non-uniform microstructures (grain sizes ranging from a few microns to a few hundred nanometers, and elongated and equiaxed grains and sub grains); 2) smaller minimum grain size (~100 nm in copper and nickel); 3) very weak crystallographic texture (preferred grain orientation); 4) deformation twinning could occur in cold sprayed copper; 5) amorphization could occur at impact interface of cold sprayed aluminum particles. In short, it is now recognized that a broad range of structural differences from conventional plastic deformation processing is possible in the cold sprayed coatings. However, no systematic comparison between cold- spray deformation and other thermo-mechanical processing methods has been done to date.

Effect of annealing – static recrystallization:

Annealing has been done to cold spray coatings in order to study the effect of grain growth and relaxation on cold spray coatings. It is seen that despite extended duration of annealing hours, the cold spray coatings don't completely recover completely due to high dislocation density and entanglement. McCune et al [57] have seen that the oxide layer after deposition prevents and curtails grain growth during annealing. The high SFE metal Al has a low dislocation density in the feedstock powder, and a low dislocation density after spraying, and exhibits recovery rather than dynamic or static recrystallization. Medium and low SFE metals Ni and Cu achieve high dislocation densities and undergo dynamic recrystallization with considerable grain refinement down to submicron scale, and to some extent show static recrystallization, where the local microstructure of Ni coatings is uniform on a scale of microns, which is not the case for copper.



### **3. Iron manganese alloy development: Effect of alloying composition on wear and corrosion property**

Abstract: Conventional alloying techniques such as casting and powder metallurgy have inherent limitations. Phases with higher melting points are difficult to melt; cooling of alloy is slow and results in segregation and separation of constituent phases. Although this can be resolved to particular with atomized powders, it increases cost and development time. In laser cladding, laser provides a clean source of thermal energy with high power density. It can produce homogenous microstructures and can adapt well to automated alloy development through variation of precursor delivery rate. Through laser cladding, various combinations Iron manganese (Fe-Mn) alloys are developed. Testing is conducted to examine galvanic current density and wear property. Results indicate that the alloy possesses excellent wear and abrasion properties and serves as a good base matrix for further development.

#### **3.1 Introduction:**

High manganese steel alloys (>10wt%) such as Hadfield steels exhibit unique combination of properties such as high strength, toughness resulting in high impact and wear resistance. The steels are well suited to applications such as railroads, grinding mill liners, crusher jaws and cones, impact hammers and bullet-proof helmets. The mechanical properties of Hadfield steel vary with both carbon and manganese contents. The tensile strength and ductility reach a maximum limit at about 1.2% C content and then decrease steadily as the carbon content is increased [12], [20]. At high levels of manganese (upwards or 25%wt) the austenitic phase can be completely retained. Thus these alloys were coined as ‘poor man’s stainless steel’ as they could mimic without the presence of nickel. Manganese although reduces the corrosion resistance of the alloy. Hence improvement in corrosion property of this alloy has been of significant interest as potential replacement of stainless steel [16]–[18], [35]. To this end,

Aluminum and chromium have most substantial effect on improving corrosion in chloride environment

In this study laser cladding is used to rapid manufacture alloys of desired composition. Typically, powder is fed into a molten pool created by a high power laser beam to form an overlay. The powder is usually a single material but mixtures can be used. The high temperature gradients and resulting surface tension ensure adequate mixing (marangonic convection) during cladding process [58]. The width of the track is several orders of magnitudes larger than dimensions of properties-controlling microstructural features such as wear, hardness and corrosion can be reliably measured. The rapid solidification nature of the process results in claddings that are representative of such solidification rate such as welding, and gas atomization of powders. Vilar et al and others [59], [60] have used laser cladding in a similar combinatorial approach to develop wear resistant iron alloys.

Literature on cladding of Fe-Mn-C ternary and Fe-Cr-Mn-C quaternary systems is limited [61]–[63]. Mazumder et al [61] focused on the evolution of carbide precipitates in these alloys. Resulting microstructures consisting of ferrite, martensitic, retained austenite and fine dispersion of different carbides have been found (M<sub>23</sub>C<sub>6</sub>, MC<sub>3</sub>, M<sub>6</sub>C, etc.) Tjong et al [62] have performed a laser surface melting of Fe-26Mn-7Al-0.9C alloy. They reported the alloy to undergo spinodal decomposition following solution treatment and aging. They observed the presence of ferritic and  $\beta$ -Mn phases after prolonged aging treatment. The presence of aluminum in Fe-Mn alloys has shown to suppress the nucleation of carbides. Data on wear resistance, corrosion property evolution on laser clad Fe-Mn Alloys is non-existent. In the present chapter, combinations of laser clad Fe-(15, 25, 35) Mn-(2, 6) Al-(2,4)Cr-(0.2)C(wt%) are evaluated for wear and corrosion resistance. Additionally, through a miniaturized punch test setup, shear strength evolution in these alloys is studied.

The objectives of this study are as follows:

Understand phase and property evolution with varying elemental concentrations: Outline the discrepancy on effect of aluminum to retain austenite. Claddings will reveal phase evolution in this quaternary system. Property will be investigated through testing described above.

Verify that lower differences in corrosion potential reflect on galvanic corrosion: Simple potential matching alone does not testify against galvanic corrosion. Actual testing in galvanic environment will reveal further artifacts that might arise during electrochemical reaction

Identify failure modes on laser cladding of Fe-Mn alloy on aluminum: Cladding of Iron alloys on aluminum will lead to formation of intermetallics and cracking. The process is difficult and unreliable. Nevertheless an effort is made to assess the possibility.

## **3.2 Experimental**

### **3.2.1 Precursor preparation:**

Experimental alloys were obtained by cladding physically mixed composition using pure Iron, electrolytic manganese, commercially pure aluminum and a 420 stainless steel powder (for chromium). Additionally for comparison, conventional stainless steel 316 powder and a pre-alloyed Fe-Mn-Al-Cr powder were clad. 12 Alloy combinations: three levels of manganese 15, 25 and 35wt% and two levels of Aluminum (2, 6 wt. %) and Chromium (2, 4 wt. %) were studied. A 1018 mild steel and aluminum A356 alloy were used as substrate.

Additional experiments with Nickel (1,2 and 4wt%), annealing of the cladding (900°C followed by furnace cooling) and evaluation with gas atomized stainless steel alloy powder (sulzer metco) was performed and presented as required.

### **3.2.2 Cladding onto 1018 mild steel.**

Cladding was performed on a Nuvonyx DMD 105D installation. This machine is equipped by a 1 kW continuous wave diode laser, a coaxial cladding head, and a CNC five-axis. The laser beam with TEM00 power density distribution is focused on the substrate at 13.5 mm distance from the nozzle tip to produce a 2mm beam spot diameter. Experiments were carried out with scanning speed  $S = 600\text{mm/min}$ , laser power  $P = 550\text{W}$ , powder feeding rate  $F = 8\text{g/min}$ . The coating was produced by overlapping successive laser tracks with a spacing  $p = 3\text{ mm}$ . Cladding parameters are listed in Table 3.1. Post annealing process: Annealing was carried out in a carbolite tube furnace at 900degC for 12hrs and furnace cooled in a Ar 5%h2 atmosphere.

**Table 3.1: Laser clad deposition parameters**

<b>Parameter</b>	<b>Values</b>
<b>Laser power (W)</b>	550
<b>Powder feed rate (gms)</b>	8
<b>Shaping gas (Ar, SLPM)</b>	6
<b>Nozzle gas (Ar, SLPM)</b>	7
<b>Nozzle gas (He, SLPM)</b>	5
<b>Cover gas (Ar, SLPM)</b>	5
<b>Carrier gas (Ar, SLPM)</b>	5
<b>Rapid speed (mm/min)</b>	600
<b>Transition speed (mm/min)</b>	600
<b>Deposition speed (mm/min)</b>	800

### 3.2.3 Cladding on to aluminum alloy:

Based on initial finding, alloy with specific composition (35%Mn, 2%Al, 4%Cr, 0.5%C) was clad onto A356 substrate. Identical cladding parameter was utilized. To reduce the formation of intermetallic at the bond line and delamination, a preheating technique was used[64]. Substrates were heated and maintained at said temperature using a hot-plate arrangement. SS316 powder was also deposited to improve understanding of the process.

### 3.2.4 Microstructure characterization:

Initial characterization of as sprayed cladding was done with scanning electron microscopy (SEM/BSE) on a Hitachi S-2600N SEM to determine the quality in terms of homogeneity, porosity and cracks. Samples used for SEM studies were prepared following standard metallographic procedures. Composition of the coatings was determined with energy dispersive X - ray analysis (EDX) in SEM and back scattered electron imaging was done to obtain composition contrast. For the phase analysis and crystal structure determination, X – ray diffraction (Rigaku MiniFlex, Cu K $\alpha$  radiation with  $\lambda = 1.5402$  0A) study was conducted. Microstructural characterization was done by transmission electron microscopy (TEM) on a JEOL 2010F at EMAL, University of Michigan – Ann Arbor, MI, USA. The TEM samples were prepared by cutting 3 mm diameter discs from the coatings after initial mechanical thinning. To

achieve electron beam transparency, final thinning was done using a Fischione twinjet Electropolisher model 110 at -25 °C. The electro polishing agent employed was 5% HClO<sub>4</sub> + 95% CH<sub>3</sub>OH solution.

### 3.2.5 Electrochemical test:

The corrosion behaviors of the as-received and annealed claddings were evaluated by using an AMETEK Princeton Applied Research (PAR) Flat Cell model K103. The surface of the corrosion specimens was slightly ground on 1200-grit emery paper, cleaned with distilled water and alcohol prior to corrosion testing. Prior to the polarization scan the samples were kept in solution to establish the free corrosion potential ( $E_{corr}$ ). Anodic polarization tests were carried out in a 0.5-wt. % NaCl solution which was prepared using analytical grade reagents. The initial pH value of the solution was 5.7 and the initial temperature of the solution was at 20°C. The specimen was driven from an  $E_{corr}$  of -1 to 2V (vs ref) at a scanning rate of 1.66 mV/s to produce potentiodynamic polarization plots. All potentials were measured with reference to a standard saturated calomel electrode (SCE). Zero Resistance Ammetry (ZRA) technique was employed to evaluate the galvanic coupling current between the claddings and A356 alloy. Tests were also run with A356 against SS316 cladding and itself. The evolution of current density with time was recorded.

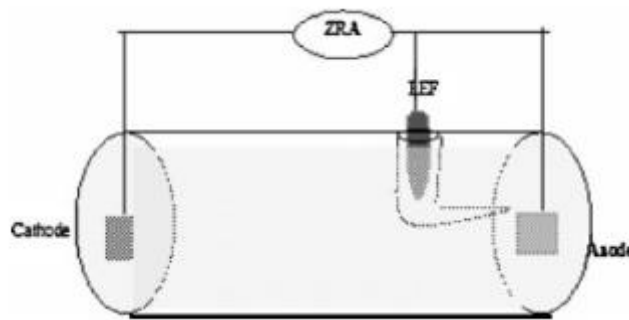


**Figure 3.1: Experimental setup for Zero Resistance Ammetry (ZRA) study**

### 3.2.6 Wear characteristics:

The tribological behavior of the claddings was studied at temperatures at room temperature (RT, ~25 °C) using a CSM high-temperature ball-on-disc tribometer. Dry sliding tests were conducted in ambient air under a load of 6 N and a sliding speed of 35mm/s for a total of 12,000 cycles. Initially both tests were done with alumina balls of 6mm diameter. Due to high wear rate

of the ball at room temperature, tests were conducted with tungsten carbide balls of identical diameter. Wear tracks and debris were analyzed using SEM/EDS.

### 3.3 Results and Discussion

#### 3.3.1 Microstructure and phase characterization on 1018 steel substrates:

Figure 3.2 presents the BSE and EDS analysis cladding deposited with mechanically mixed powder. The microstructural features are representative of a typical laser clad deposition. The low dilution with substrate and homogenous alloying of elements are apparent in the EDS map. Table shows the results of EDS analysis for various alloys. There no significant loss of manganese in the cladding, the overall variation in obtained composition is acceptable as no two compositions are similar to each other.

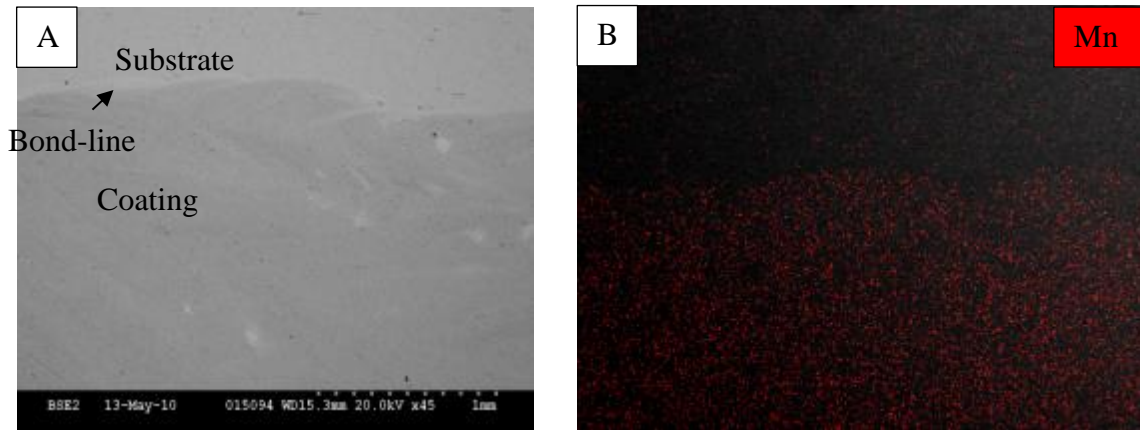


**Figure 3.2: Cross-section microstructure of the Fe-25Mn-6Al-4Cr-0.2C %wt Specimen (A) BSE Image bringing out compositional contrast (B) EDS map showing with Mn (red dots) showing minimum dilution with base alloy**

Phase analysis using XRD is presented in Figure 3.3. At 15%Mn, austenite could not be completely retained a mild ferritic peak is observed even at low Aluminum and Chromium concentrations, At 25%Mn and 35%Mn there was no or minimal presence of martensite. 15%Mn Alloy with 6%Al and 4% Cr showed the maximum martensite content and is shown in the figure.

The rapid solidification rates in laser cladding increases the amount of retained austenite. After annealing, the alloy compositions are in in agreement with the Schaeffer plot (Ni –Cr equivalency diagram). For the purposes of this study, evaluation on as received claddings is continued as planned.

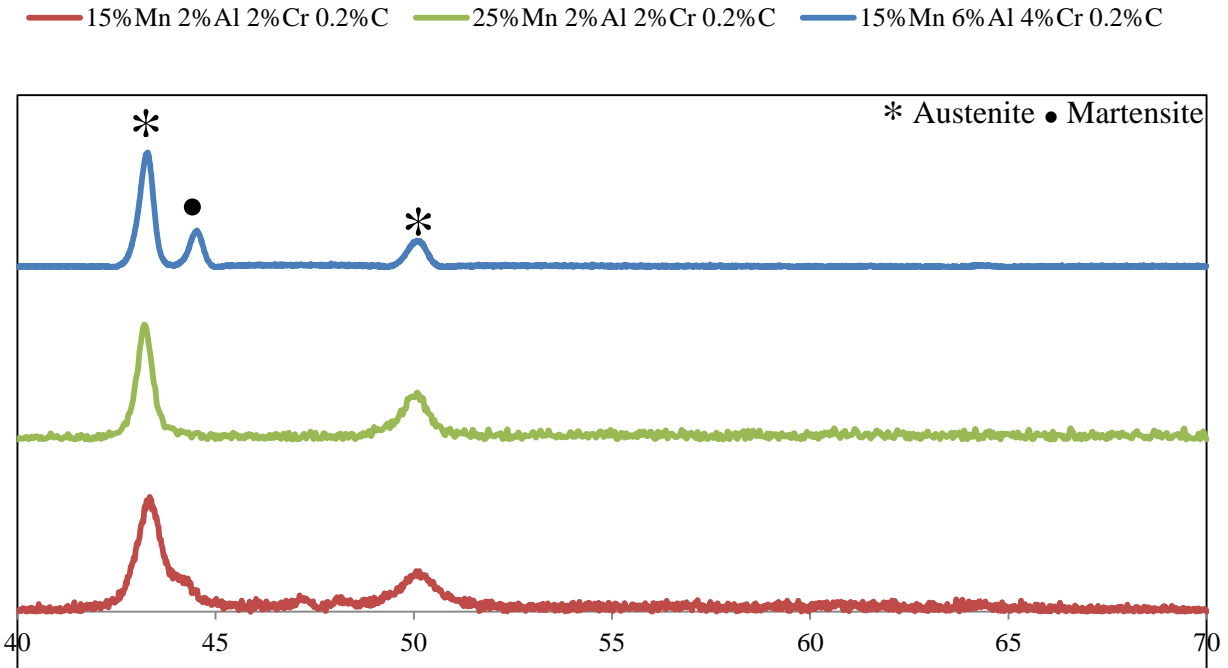


**Figure 3.3: X-ray diffraction data of select Fe-Mn Alloys**

### 3.3.2 Microstructure and phase characterization Aluminum 6061 substrate:

Initial deposition parameters were translated from experiments on steel substrates. Then, the deposition power and scanning velocity were increased to compensate for the lower melting point of the A356 substrate. This prevented the substrate from excessive distortion and melting. The poor solubility of steel in Aluminum alloy results in formation of brittle intermetallic and poor bond line. Additionally, EDS revealed presence of higher aluminum content in these claddings. The solution to preheat the substrate was adopted from previous literature [64]. For a substrate size of 50mm by 50mm by 12mm crack free deposition was observed between preheating temperatures of 350 and 400deg C. EDS revealed more than desired levels of Aluminum in the cladding. Hence there was significant dilution of the substrate. Further reduction of laser power and increase in scanning velocity yielded poor deposition. Hence aluminum content in the precursor material was reduced to compensate for excess levels.

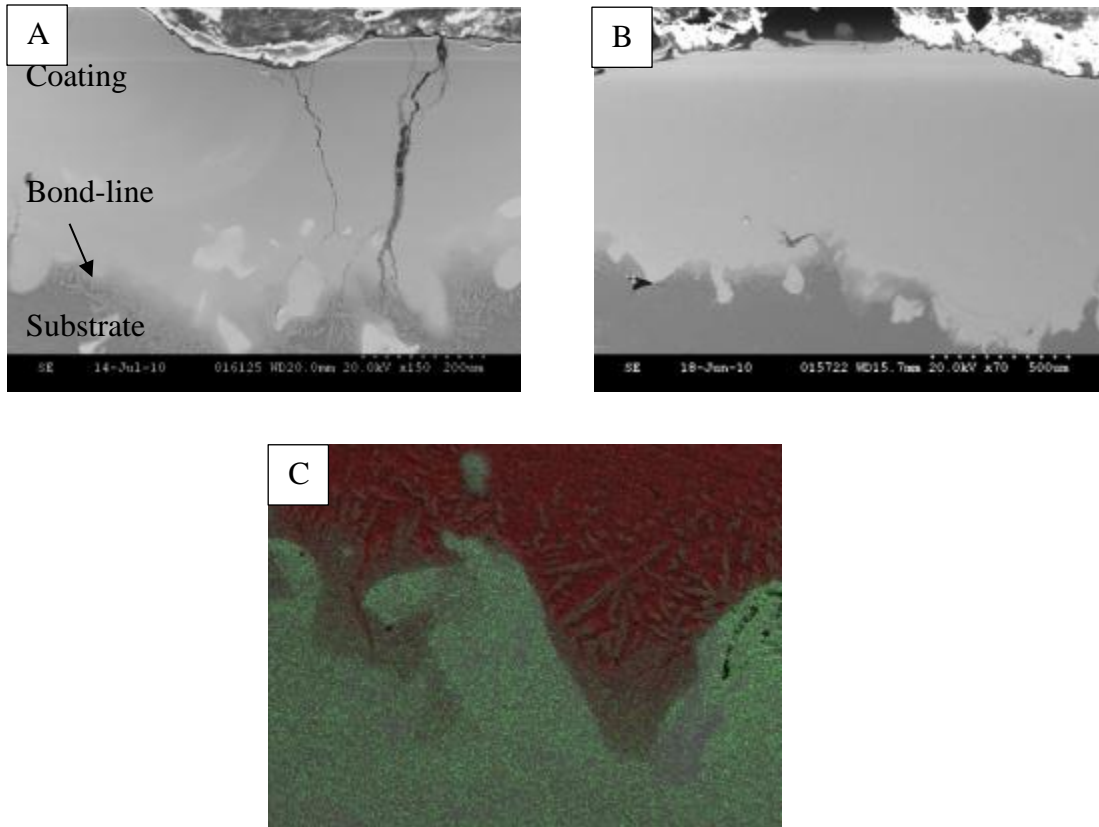


**Figure 3.4: (A) Cladding on aluminum substrate (B) Improved cladding on aluminum after preheating (C) EDS Map shows dilution in the Clad/Aluminum interface**

For as deposited alloys onto A356, austenitic phase couldn't be preserved. A356. Hence we attribute higher quench rates undergone in A356 alloy. It was also observed with XRD that with use of increasing preheating, martensite fraction dropped. Hence phase preservation in Fe-Mn alloys could stem from the following reasons: 1) Premixed powders do not mix well enough 2) Change in time-temperature history due to Aluminum substrate. To probe further, prealloyed austenitic stainless steel was clad onto aluminum alloy. The result was similar and complete austenitic phase could not be preserved. Hence, phase preservation was caused by the aluminum substrate itself. Since preheating reduces the ferritic phase, faster quench rates, leading to insufficient time during solidification could be probable reason. Claddings on aluminum alloys are not only susceptible to cracking and intermetallic formations but also suffer from phase preservation. Due to uncontrolled phase evolution in aluminum substrates further evaluation of coatings were discontinued.



### 3.3.3 Electrochemical characterization

#### 3.3.3.1 Short term open circuit potential measurements

The open circuit potential in 0.5% NaCl solution is plotted in Figure 3.5 and 3.6. The results are split into effect of manganese concentration with that of aluminum at constant 2wt% chromium level and between manganese and chromium at constant 2wt% aluminum level. Increase in aluminum and chromium increases the OCP to nobler potentials. The effect of manganese does not follow a linear trend. The OCP value at 35% Mn has a negative influence at high concentrations of Al and Cr. At lower concentrations of 2wt% Al and chromium, 25% Mn gives the lowest OCP values.

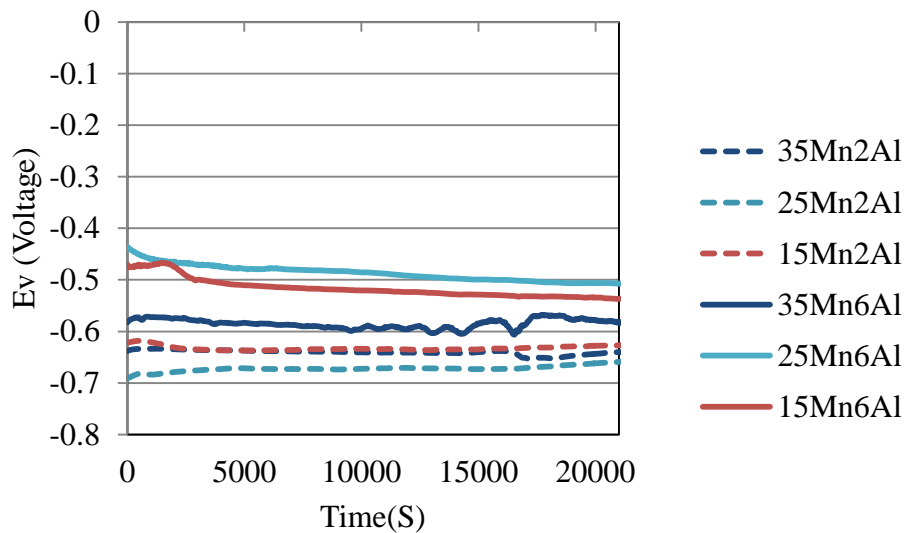


**Figure 3.5: Open circuit potential of Fe XMn YAl 2Cr. Solid lines- 6 Al, Dashed- 2 Al.  
Blue-35%Mn, Teal-25%Mn, Red-15%Mn**

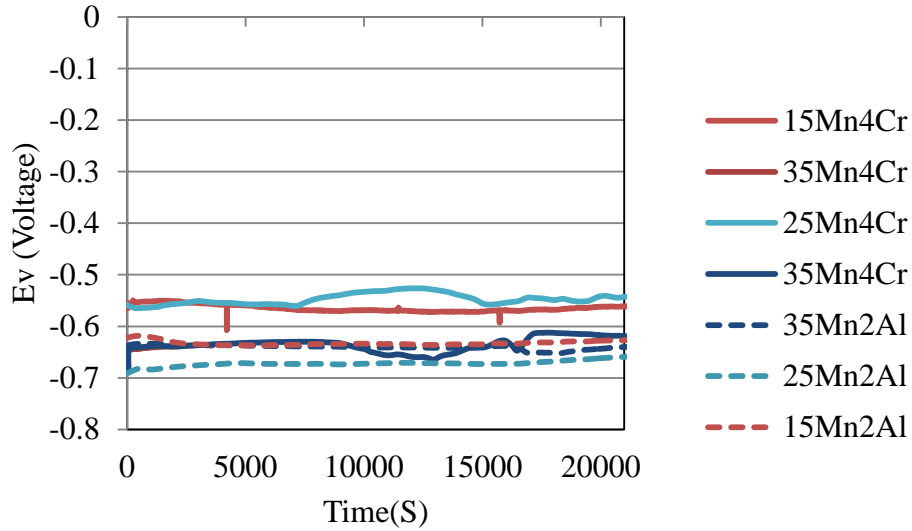


**Figure 3.6: Open circuit potential of Fe XMn 2Al YCr. Solid lines- 4 Cr, Dashed- 2 Cr. Blue-35%Mn, Teal-25%Mn, Red-15%Mn**

### 3.3.3.2 Long term open circuit potential measurements

Open circuit potential of Fe-35Mn-2,4,6Al-4Cr-0.2C (wt%) alloys measured for a period of 7 days is shown in Figure 3.7. The OCP of aluminum 356 alloy is also plotted for the same duration. The corrosion potential for all the alloys exhibited a slow decreasing trend. There was no instability observed. The addition of aluminum resulted in higher potentials similar to that observed in the short term tests.

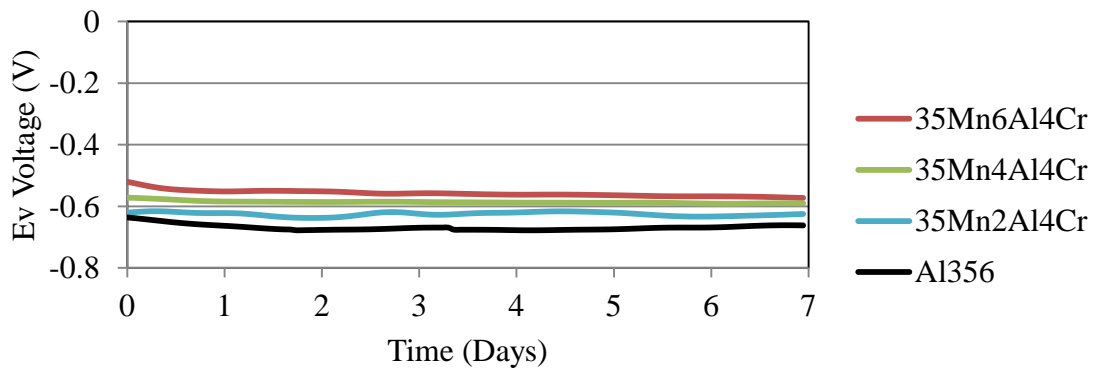


**Figure 3.7: Open circuit potential data of Aluminum 356 Alloy (Black) Fe-35Mn-2Al-4Cr (Cyan) Fe-35Mn-4Al-4Cr (Green) Fe-35Mn-6Al-4Cr (Red)**

### 3.3.3.3 Electrochemical Study – Potentiodynamic Analysis:

Figure 3.8 presents the typical potentiodynamic polarization behavior of selected alloy combinations and that of A356. For specimens with higher concentrations of Aluminum and Chromium multiple tafel slopes were obtained. The disappearance of these artifacts after annealing can be attributed to homogenization of the alloy. This effect is in agreement with X ray diffraction peaks. The tafel characteristics of annealed deposit show similar data to conventional materials. The  $E_{corr}$  and  $I_{corr}$  value computed are shown in Table 3.2. The addition of nickel has the highest weighted response to improvement in corrosion resistance. In doing so, the alloy develops substantial difference in potential with respect of A356 alloy. The addition of aluminum and chromium increase the  $E_{corr}$  value, while there is no significant change in  $I_{corr}$  value. The cathodic slope of the alloys does not show any significant passivation region with current density plateauing at 2mA above 1V w.r.t to ref.

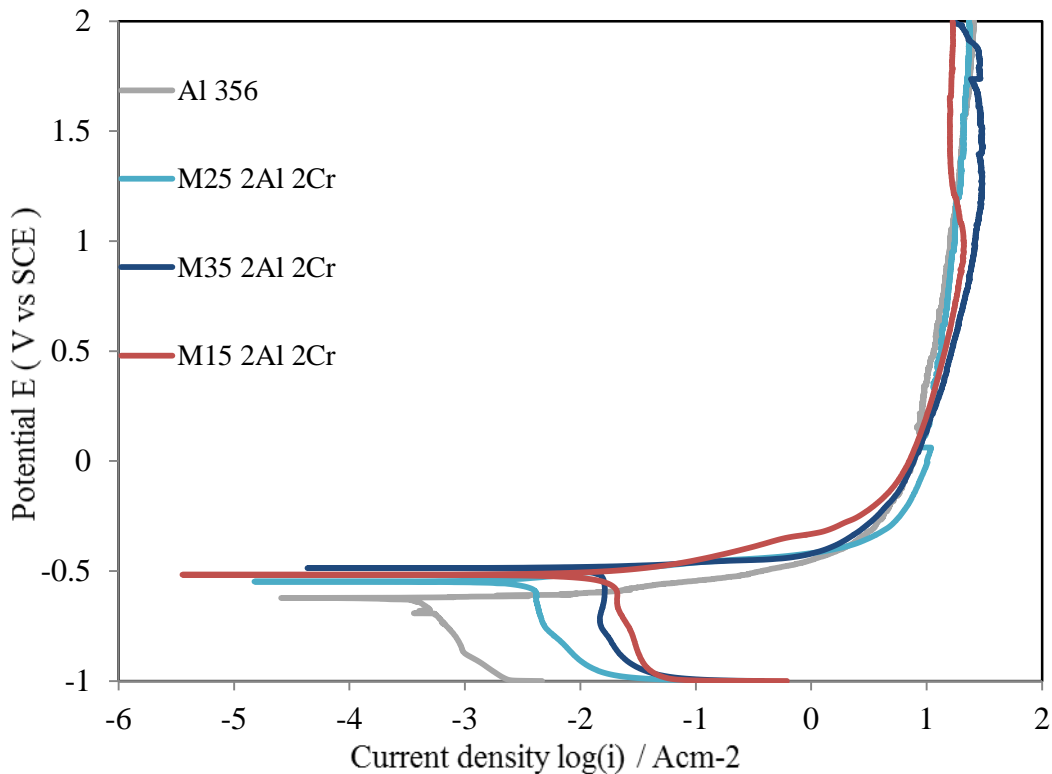


Figure 3.8: Potentiodynamic plot of Fe-Mn Alloys in 0.5wt% NaCl solution

**Table 3.2: Ecorr and Icorr obtained from polarization curves by Tafel extrapolation method**

Alloy		Ecorr mV	Icorr $\mu$ A	
Al356		-622.06	0.361	
35% Mn	2% Al	2% Cr	-482.3	7.773
		4% Cr	-422.09	6.083
	6% Al	2% Cr	-423.31	10.117
		4% Cr	-413.11	12.15
25% Mn	2% Al	2% Cr	-534.01	2.602
		4% Cr	-398.87	4.422
	6% Al	2% Cr	-346.94	5.792
		4% Cr	-244.44	1.034
15% Mn	2% Al	2% Cr	-516.95	12.115
		4% Cr	-315.4	1.799
	6% Al	2% Cr	-379.42	2.469
		4% Cr	-128.75	0.058

**3.3.3.4 Electrochemical Study – ZRA results:**

Galvanic corrosion is not necessarily dictated by potentials alone [65] Hence direct galvanic current measurements were conducted to supplement the results of open circuit potentials. Figure 3.9 shows current density levels across various samples with A356 alloy after a 1hr stabilization period. Alloy with lowest amount of Al and Cr shows anodic behavior with reverse corrosion current density. To eliminate errors due to incomplete phase transitions during laser cladding, results were verified with the annealed sample. Annealed samples also presented identical results. Stainless steel shim stock was also tested. This produced significantly higher corrosion current densities as can be seen.

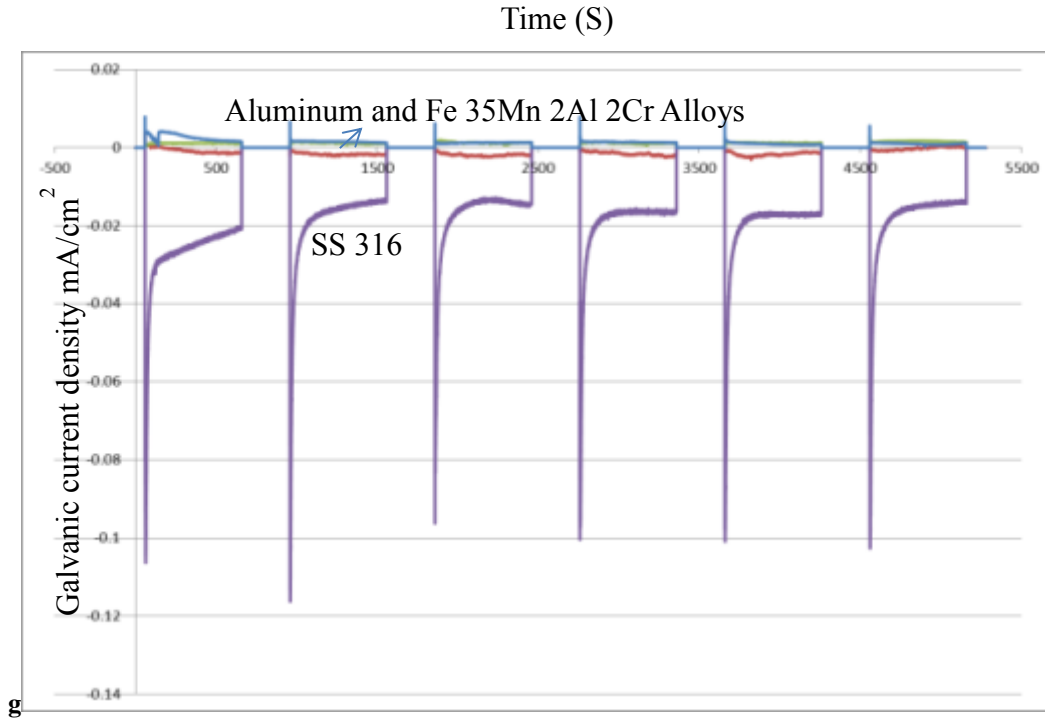


**Figure 3.9: ZRA current density evolution of various samples against aluminum as cathode**

### 3.3.4 Wear testing:

High Manganese iron alloys have well-known abrasive wear characteristics. Coefficient of friction curves for samples is shown in Figure 3.10. Coefficient of friction values measured during each of tests showed an initial period of rapid change before settling down into a steady state. This is the ‘break in’ phase and variations present here arise from the initial surface finish of the specimen. The duration of the phase typically lasts for <500 laps and is a typical characteristic of the wear test itself. Following this period a debris start to form, oxidation occurs, causing increase in friction or false brinelling. The oxidized debris starts to micro cut and fret the surface. The 15% Mn alloys gave the most stable frictions values indicating least influence from the debris. Wear tracks were then measured with profilometer and is presented in Figure 3.11. 15% Mn coatings present the lowest wear track volume with 25 and 35%wt Mn with decreasing wear resistance. Hence the presence of martensite enhances wear resistance of the material.

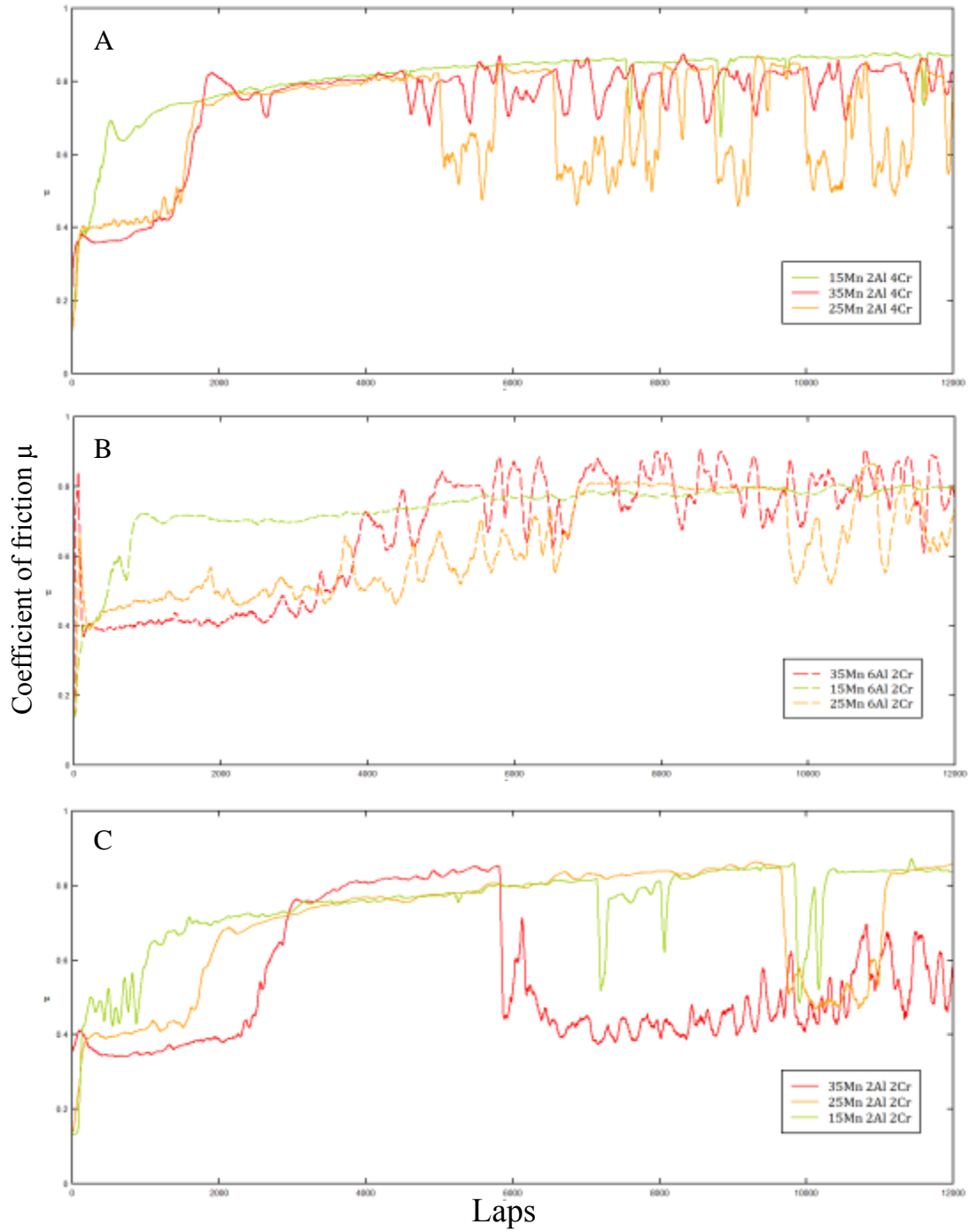
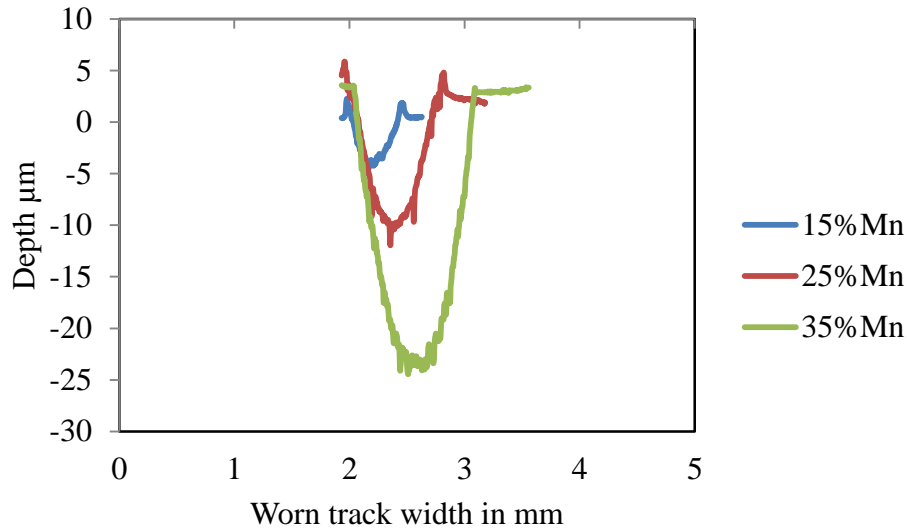


Figure 3.10: Coefficient of friction curves for various alloys A) Fe-Mn-2Al-4Cr (B) Fe-Mn-6Al-2Cr (C) Fe-Mn-2Al-2Cr. Red-35%Mn, Orange-25%Mn, Green-15%Mn



**Figure 3.11: Depth profiles of the worn sections of Fe-XMn-2Al-2Cr-0.2C alloy after wear test**

### 3.4 Summary

The goal of the study was to create a low cost wear resistant coating material for aluminum alloys. High manganese iron alloys present a potential solution and can be adapted to suit this application. Fe-Mn-Al-Cr-C alloys were laser clad onto mild steel substrates with minimum dilution. A microstructure property evolution of these alloys was then performed to study the effects of alloying elements. The findings are summarized below:

- At least 25% by wt. Mn was required for complete preservation of austenitic phase
- Aluminum and Chromium enhance corrosion potential of the alloy but in doing so also increase galvanic potential which will lead to higher corrosion rate.
- 15% Manganese alloys percent manganese alloys exhibit highest wear resistance due to presence of martensite. Lower manganese content also increases corrosion potential
- Hence a tradeoff lies between general corrosion property and wear resistance against galvanic coupling.
- Effective use of preheating improved cladding onto aluminum substrate but cannot preserve complete austenitic phase.

#### **4. Coating development strategies**

Table 4.1 lists the possible deposition techniques tested to generate Iron manganese (Fe-Mn) coatings on Aluminum alloy. Other thermal spray techniques were also tested but resulted in excessive oxidation and loss of manganese due its low vapor pressure. Twin wire arc and Hybrid deposition process are described elsewhere [66]. Both these techniques require ‘wire’ feed stock.

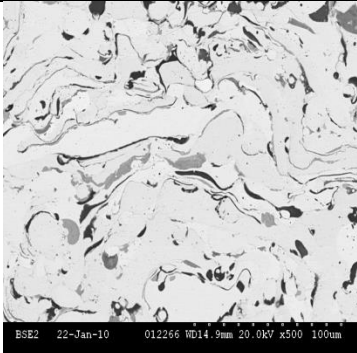
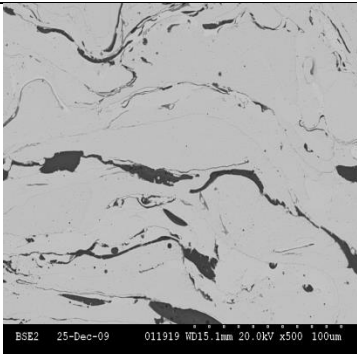
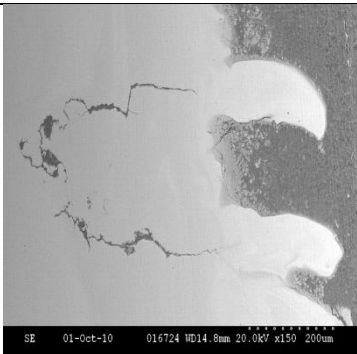
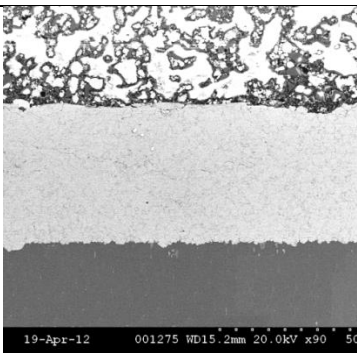
Due to the inability to feasibly draw Fe-Mn alloys into wires, cored wires with necessary composition were fabricated. Due to the high solidification rates, homogenous coating could not form. These are evident from the backscattered electron (BSE) images.

Laser cladding was also used to generate coating both from physically mixed powders and gas atomized powders. The higher power densities of the laser along with marangonic convection result in homogenous coatings. A draw back of the process is the formation of unwarranted intermetallic phases that result in delamination of coating interface unless deposited with preheated conditions (see Chapter 3).

Cold gas dynamic spray (or cold spray) process is a non-thermal approach to deposit Fe-Mn coatings. The process relies on high strain rate adiabatic deformation of the coating material ( in the form of powders ). The solid-state approach to coating development overcomes the drawbacks of oxidation, manganese evaporation and intermetallic formation posed by thermal based processes. Initial trials with gas atomized powders demonstrated dense homogenous coatings metallurgical bonded to the aluminum to form a well adhered interface. Cold spray was hence used for further development of Fe-Mn coatings.



Table 4.1: Deposition routes to achieve iron-manganese coatings on aluminum

Deposition Style	Feedstock	Crosssection	Comments
Twin wire Arc (TWA) sprayed From cored wire	Cored wire		High deposition rate but inhomogeneous coatings
Hybrid (TWA + HVOF) sprayed From cored wire	Cored wire		High deposition rate but inhomogeneity not fully solved
Laser cladding	Physically mixed or Gas atomized powders		Homogenous coating but intermetallic formation in interface
Cold sprayed from powder	Gas atomized powders		Dense, homogenous coating

## **5. Cold spray process development of Iron manganese alloys: Numerical modeling and experimental validation**

### **5.1 Introduction**

The cold spray nozzle: The supersonic gas streams required for cold gas dynamic spray are obtained using a convergent divergent nozzle (de Laval nozzle) [27], [67], [68]. When the temperature and pressure of a gas exceed certain conditions in the convergent section (i.e the stagnation conditions), sonic conditions are reached at the throat of the nozzle. At this point forward the nozzle flow shifts from a venturi to a supersonic regime. As the stagnation conditions are further increased a shock wave moves further downstream along the divergent section of the nozzle. To form a coating, desired powders are accelerated upon introduction into the supersonic gas stream. The maximum particle velocity is hence determined by gas velocity and particle gas contact duration. Hence successful nozzle design is a combination of the expansion ratio and length. A further caveat is that the nozzle geometry is optimized only for designed pressures and temperatures. Altering the gas conditions will affect the transition or shock zone where the high velocity gas meets the ambient.

A discussion is presented on various aspects of cold spray nozzle design. Most of these factors are interdependent and a concise summary of the factors is then portrayed in a block diagram (Figure 5.3)

#### **5.1.1 Expansion ratio:**

This is the ratio between exit area ( $A_e$ ) to that of the throat ( $A^*$ ). This dictates the Mach number of the nozzle, large ratios will lead to higher gas velocities and vice versa. For a given pressure and temperature, as this ratio expands from unity, the nozzle operates in three distinct regimes: under, normal, and over expanded modes. Under and Over expanded modes are exact opposite,

in an under expanded mode, the gas pressure meets the ambient further the nozzle exit. Jodoin [69] has pointed out that too low expansion ratios result in higher temperature of exit gas annulling the benefit of cold spray process. Too high exit Mach numbers will result in excessive shock affecting particle velocity. While several studies are presented on the ideal nozzle expansion ratio and its operating regime, there is ambiguity on the nozzle operating regime – over expanded vs perfect expanded flow. Grujic et al [70] claim perfect expansion, while Li et al claim slight over expanded regime[71]. While maximum velocity plays a key role in improving deposition efficiency other influencing factors such as exit temperature of the gas stream[69] and particle velocity distribution across the nozzle cross-section [54].

#### 5.1.2 Nozzle throat:

The throat of the nozzle which is characterized by smallest cross-section diameter determines the flow rate of the accelerating gas. A larger throat permits higher gas flow rates through the nozzle. Higher flow rate enables heavier particle loading and thus increases deposition rate.

#### 5.1.3 Nozzle length:

The length of the nozzle increases the velocity of the powder due to its increased dwell time in the nozzle. Also extending the nozzle adds resistance to flow and an effect similar to reducing expansion ratio is obtained[68].

#### 5.1.4 Standoff distance:

Particle size, density, shockwave determine the standoff distance. Pattison [72] has split the standoff zone into three regions (see Figure 5.1). For this reason the amount of powder that can be loaded is not indefinite [73]. This loading effect can be realized with stokes number. The ratio of particle response time over a time scale related to fluid flow. Li et al [74]describes this with stokes number.

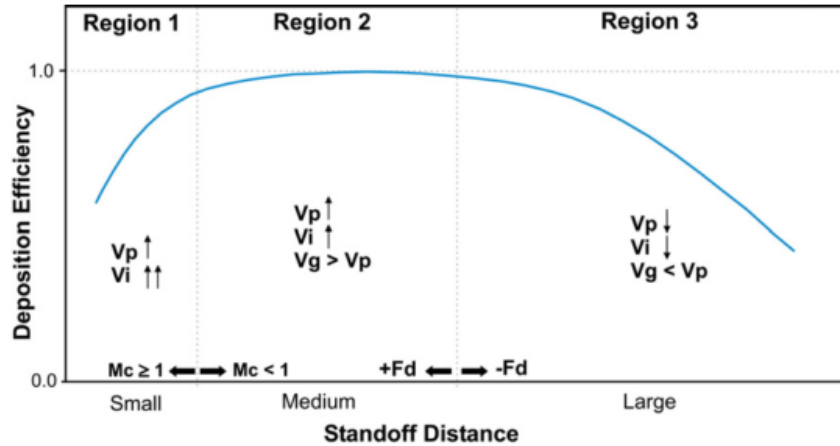


Figure 5.1: Non dimensional chart showing the effect of standoff distance on deposition efficiency [72]

#### 5.1.5 Nozzle crosssection geometry:

Alkimov [54] had tested different geometries and concluded that rectangular nozzles give a uniform velocity distribution, while circular nozzles result in Gaussian profile, with peak velocities much higher than those obtained with rectangular nozzles(see Figure 5.2). A more homogenous coating can be deposited with rectangular nozzles with wider coverage.

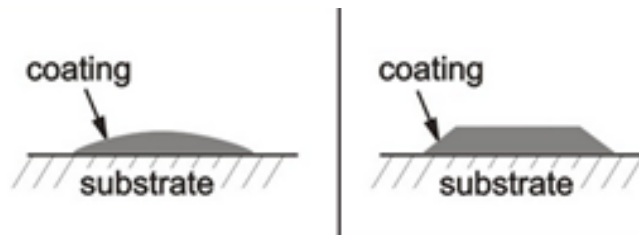


Figure 5.2: Deposition profiles with circular and rectangular nozzles

#### 5.1.6 Nozzle wall friction:

With prolonged deposition, nozzle wall is prone to wear and increase in roughness. Han et al[75] have shown the effect of nozzle roughness on deposition process. A roughness value of 100  $\mu\text{m}$  can reduce particle velocity by 80 m/s. Hence this must be factored during nozzle design and development.

### 5.1.7 Powder injection:

Precursor powder can be introduced either upstream (UI) in the stagnation region or downstream (DI) where the gas is expanding. Both techniques have their advantages and limitations. In UI the particles are introduced axially, they heat up for a brief period prior to accelerating. While the increase in particle temperatures is beneficial, UI nozzles are prone to fouling and throat wear. Further, UI limits maximum stagnation temperature required for materials that require severe processing conditions, as this would accelerate fouling of the throat. The DI scheme is typically used to take advantage of lower injection pressures required to inject the precursor particles at an angle at the beginning of the downstream region. Further, there is no affect in throat diameter.

### 5.1.8 Nozzle contour:

The expansion path of a nozzle can be linear or contoured. Contoured nozzles or bell shaped nozzle can help weaken the shock state of the gas jet as it exits the nozzle into ambient conditions. Contoured nozzles can be developed through a set of partial differential equations known as the method of characteristics (MOC). These equations were originally used to develop shortest possible nozzle with large expansion ratio used for propulsion. Stoltenhoff et al. [23] have shown a variation from 38 to 72% in deposition efficiency with four nozzles with different expansion ratios (6 or 9), contours (conical and bell), and lengths.

### 5.1.9 Computational Fluid Modeling and Visualization:

Literature is available on the systematic numerical study of the nozzle using 1D isentropic model, 2D and 3D models[47], [76]–[82]. 1D model are capable of generating a fairly good estimate of the gas and powder velocities. Commercially available CFD software fluent has been used to generate accurate predictions. Computational analysis of supersonic jets occurring in the cold spray nozzle involves the following prevailing equations:

- Reynolds averaged Navier-stokes equations: Conservation of mass and momentum for compressive turbulent flow field

- Energy conservation equation
- Closure relations for the above equations: For cold spray process K-e, RNG KE, Realizable k-e and rsm models are frequently used.
- Ideal gas law and Sutherland's law for temperature dependent gas viscosity.
- An ideal gas model with RANS based solver such as K- $\epsilon$  or Reynolds stress model (RSM) has been used.

Computations of the flow field through the nozzle have been accurately reproduced by Reynolds averages navier stokes turbulence models. While K- $\epsilon$  model has been widely used, the realizable K- $\epsilon$  model or the RSM scheme is preferred as it accounts for rotation flow. Coupled or segregated solver and Quick discretization have been used to successfully predict the flow field. Various drag models have been developed [83]–[85] to predict particle acceleration. Stochastic model, discrete random walk, cloud tracking have been utilized with coupled K- $\epsilon$  or RSM (internally coupled) based models. As Biot number of the powder is low, particle heating is neglected[86]. Grujicic et al [70] have predicted a maximum particle loading rate of 3%, particle carrier flow rate of 10%.

Objectives of present investigation:

In this study the development of an optimized rectangular divergent nozzle with downstream injection for deposition of iron-manganese powders is presented. The effect of nozzle with varying expansion ratios through the following operating regimes – under expanded – perfect expanded and over expanded regimes is numerically calculated followed by experimentally verification. Goals of this chapter are as follows:

- Settle ambiguity by experimentally verifying the effect of nozzle expansion ratio and resulting particle velocities and gas temperatures on deposition efficiency.
- Determine numerically, the effect of injection angle on downstream injected nozzles.
- Determine effect of traverse velocity and particle size distribution on deposition efficiency.

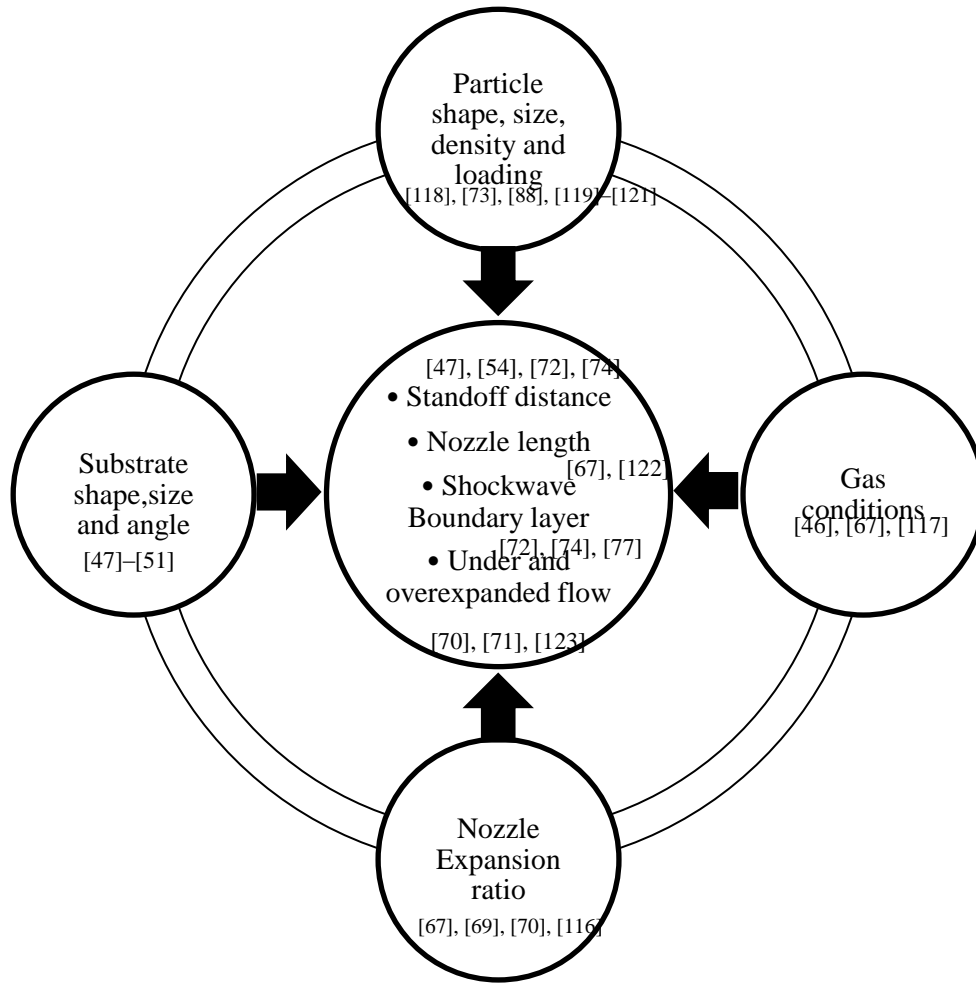


**Figure 5.3: Parameters that affect particle acceleration and cold spray deposition efficiency**

## 5.2 Experimental

### 5.2.1 Geometry and Preliminary particle injection evaluation

Four different nozzle geometries (Table 5.1) and three different injection schemes are evaluated in the present study. Figure 4.1 presents the schematic of the nozzle geometry used in this study. The nozzle has a conical convergent and rectangular divergent cross section. Geometry of Nozzle10 is chosen to evaluate the particle injection location. Nozzle UI, injects particles 50mm upstream from the throat. Nozzle DI-90, DI-45, DI-25 injects particles at a 90,45 and 25 degree angle 6.35mm downstream from the throat. The choice of injection location is based on manufacturing feasibility. The feed port diameter is kept constant in Nozzle DI-90 and DI-45 at 2.54mm. DI-25 nozzle has a smaller feed port (1.27mm) to make physical room for the small injection angle.

**Table 5.1: Nozzle geometries evaluated in this study**

Name	Expansion ratio	Aspect Ratio	Injection
Nozzle7	7.10	2.5	Downstream 45°
Nozzle8/DI-45	8.15	2.5	Downstream 45°
Nozzle9	8.75	2.0	Downstream 45°
Nozzle10	10.65	2.5	Downstream 45°
DI-90	8.15	2.5	Downstream 25
DI-25	8.15	2.5	Downstream 90°
Axial	8.15	2.5	Axial

### 5.2.2 Computational domain:

Numerical modeling was performed using commercial software Ansys Fluent (V14.0). Nozzles A and C could be run as a quarter model with two symmetric planes while Nozzle B was halved with one plan of symmetry to reduce the computational time. The domain was meshed using Ansys Workbench meshing tools with quadrilateral cells. For the quarter model total number of elements were 200,000 which was further refined using region adaptation in fluent to a total of 264,000 elements. This way element could be concentrated at the region of interest which is around nozzle exit. The nozzle inlet is treated as pressure inlet with a pressure of 2.7 MPa and a temperature of 873K. A mass flow inlet was later used to improve convergence. The injection port was treated as mass flow inlet and kept at 10% of flow in the nozzle. A pressure outlet boundary was applied to surfaces directly in front of and above the nozzle. The heat transfer process between the gas and the nozzle wall is not considered.

Nitrogen is employed as the gas phase and governed by the ideal gas law which takes the compressibility effects into consideration. The Sutherland coefficient is applies to consider change in viscosity with temperature. A pressure based solver is used to perform the simulation at steady state. The model is run initially with RNG run with realized k-e model and then converted to RSM model to avoid divergence error and reduce computation time. A quick discretization scheme was used for momentum and density pressure to get well defined shocks. 2nd order was used for pressure.



DPM model is used to inject particles into the model. The mass flow rate of the particles was tested at 1 and 3g/s maintained at 3% of the mass flow rate of nozzle gas. Two-way coupling is accounted for in the RSM scheme. In addition discrete random walk model was used to account for stochastic prediction. A particle inlet velocity of 5m/s was used in all cases.

Experimental verification and further optimization: Numerical modeling was followed by experimental testing for validation. Different nozzle geometries were fabricated with constant throat diameter of 2mm and 270mm expansion length. The nozzle was run at stagnation conditions of 400psi and 6000C, identical to that used in the numerical model. Nozzle geometry optimization was carried out with Stainless Steel 316 powder (Praxiar, Indianapolis). Deposition parameters such as standoff, nozzle scan velocity and powder size distribution was carried out with Fe-Mn<sub>2</sub> Powder. The compositions of both powders are listed in Table 5.2

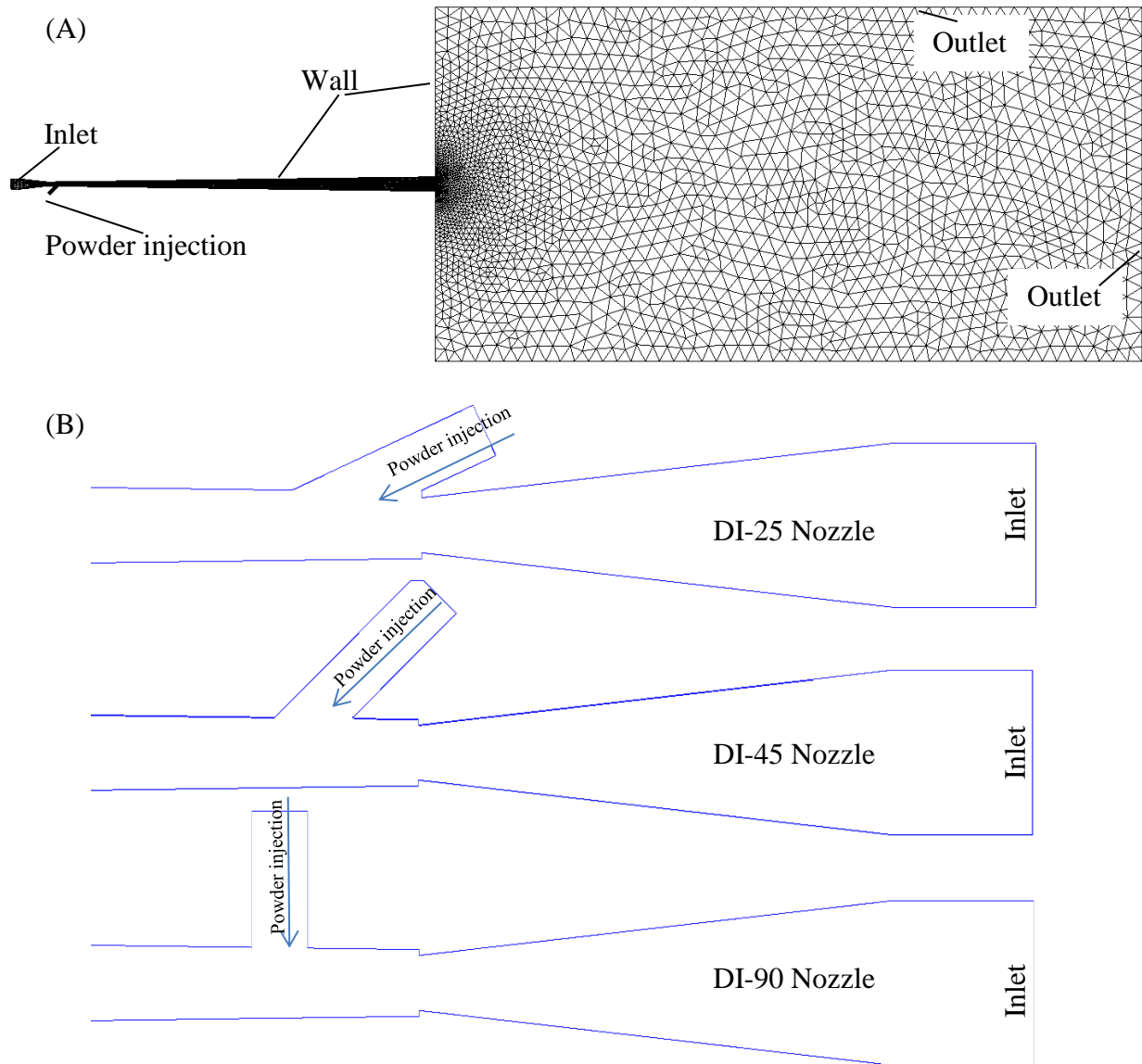


Figure 5.4: (A) Schematic of the computation flow domain (B) Injection geometries evaluated in this study

Table 5.2: Composition of Fe-Mn powders (balance Fe)

	C	Si	Mn	P	S	Ni	Cr	Mo	Al
<b>SS-316</b>	0.026	0.88	0.15	0.02	0.007	11.3	16.2	2.3	-
<b>Fe-Mn2</b>	.2	-	35	-	-	-	2	-	4

### 5.2.3 Microstructure characterization

Initial characterization of as sprayed cladding was done with scanning electron microscopy (SEM/BSE) on a Hitachi S-2600N SEM to determine the quality in terms of homogeneity,

porosity and cracks. Samples used for SEM studies were prepared following standard metallographic procedures. Composition of the coatings was determined with energy dispersive X - ray analysis (EDX) in SEM and back scattered electron imaging was done to obtain composition contrast. For the phase analysis and crystal structure determination, X – ray diffraction (Rigaku MiniFlex, Cu K $\alpha$  radiation with  $\lambda = 1.5402 \text{ \AA}$ ) study was conducted

#### 5.2.4 Surface temperature

A CSL high speed pyrometer was used to detect real time non-contact surface temperature measurements. The pyrometer reads a wavelength of 2.5 to 5 $\mu\text{m}$  which is away from the 1.03 $\mu\text{m}$  wavelength of the laser. The default emissivity value supplied with the sensor was used. Data from the pyrometer was logged with nation instruments lab view software using usb-daq acquisition hardware.

#### 5.2.5 Wear characteristics

The tribological behavior of the coatings was studied at temperatures at room temperature (RT,  $\sim 25 \text{ }^\circ\text{C}$ ) using a CSM ball-on-disc tribometer. Prior to testing, samples were polished with 1200 grit SiC polishing paper to avoid excessive tangential loads during testing. Dry sliding tests were conducted in ambient air under a load of 6 N and a sliding speed of 3.25cm/s for a total of 12,000 cycles. A SS316 ball (McMaster-Carr) was used as a static friction partner.

#### 5.2.6 Bond strength measurements

Standard ASTM C633 adhesion strength tests consist of gluing the cold sprayed samples to grit 24 alumina blasted mild steel cylinders with FM1000 epoxy glue (Cytec Industries, Woodland Park, NJ) followed by a destructive tensile test which measures the coating-substrate adhesion strength. Prior to gluing the cold sprayed samples to the mild steel cylinders, the epoxy glue was first heat treated in an air furnace at  $90 \text{ }^\circ\text{C}$  for 3 h. In order to ensure proper adhesion between the glue and the metallic surfaces, the samples were heat treated in an air furnace at  $200 \text{ }^\circ\text{C}$  for 3 h and then air cooled at room temperature. All ASTM C633 adhesion strength tests were performed using an Instron 4469 universal testing machine (Burlington, Ontario, Canada) with a 50 kN dynamic load and a constant speed of 0.5mm/min

### 5.3 Results and discussion:

A grid independence study was conducted and axial gas velocity was recorded with model comprising 264K elements and refined into 384, 428 and 496K elements. The gas velocity profile was identical and simulation was hence study was conducted with 264K elements (Figure 5.5).

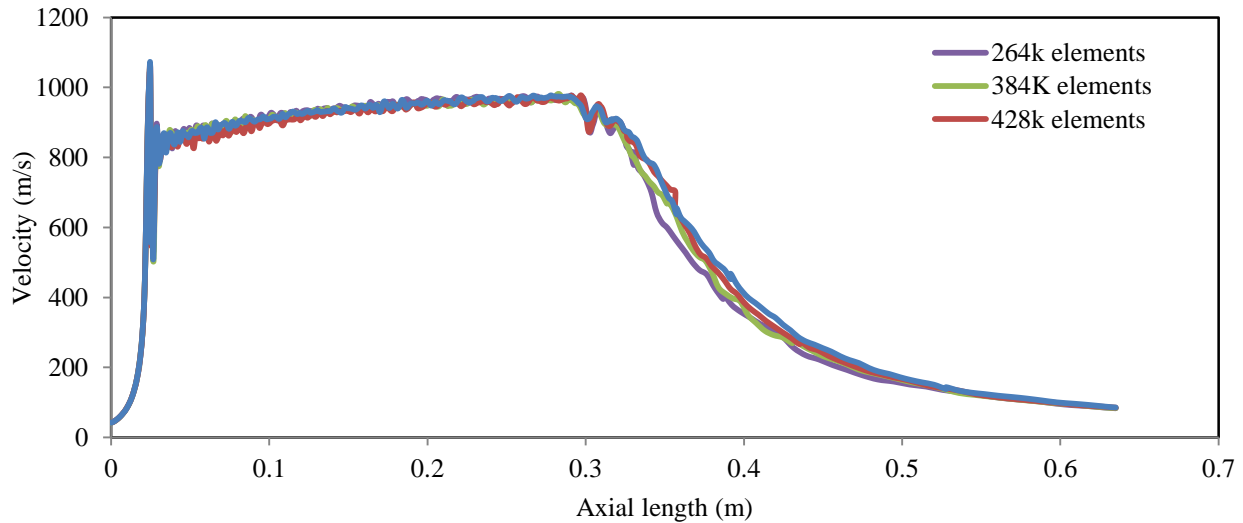


**Figure 5.5: Grid independence study**

The gas velocity and temperature along its axis for the various nozzle geometries are presented in Figure Given, the lowest expansion ratio in Nozzle 7, it experiences least ‘shock’ at the exit of the .5.6 nozzle. The velocity contours at nozzle exit (Figure 5.7) portray the effect of expansion ratios on the shockwave wave. Particle data was collected at 10mm plane from nozzle exit. The particle velocity distribution is plotted in Figure 5.8. The velocity distribution is across a lower spread for Nozzle 7 and comparable for the other nozzles.

The effect of injection angle on particle velocity is shown in Figure 5.9. Here the distributions of particles from the three different injection angles are mapped at a 10mm plane from the nozzle exit. The velocity of the particles is highest at the center of the nozzle. The 90° and 25° injection angle result in particles preferentially distributing towards and away from the injection side of the nozzle. The 45° injection angle results in slight even distribution of particles near the axis of the nozzle. This results in a tighter velocity distribution as listed in Table 5.3. The injection angle also determines the carrier gas pressure with 90° injection requiring lower effort.

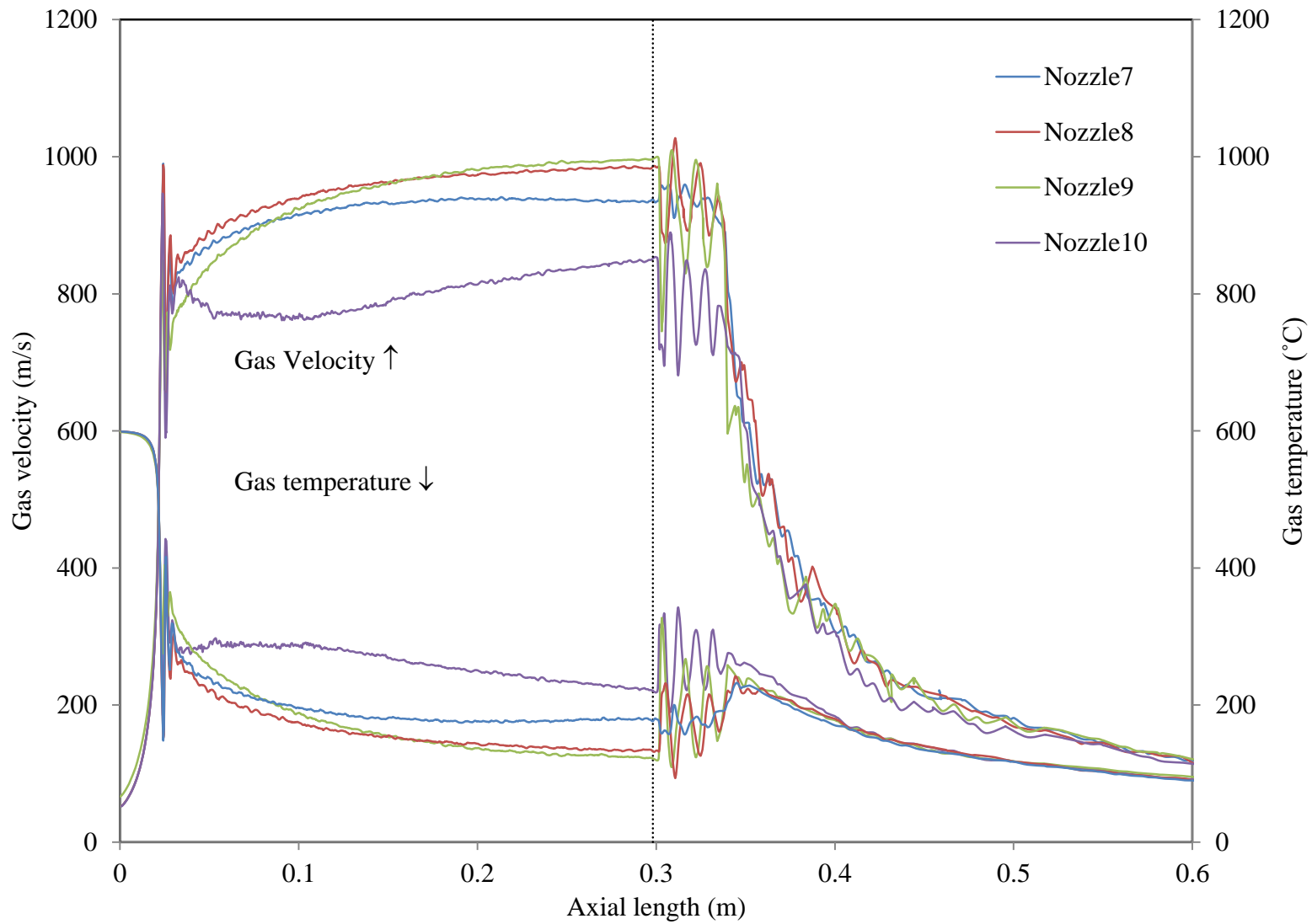


**Figure 5.6: Axial gas velocities and temperature profiles across the length of the deposition system**

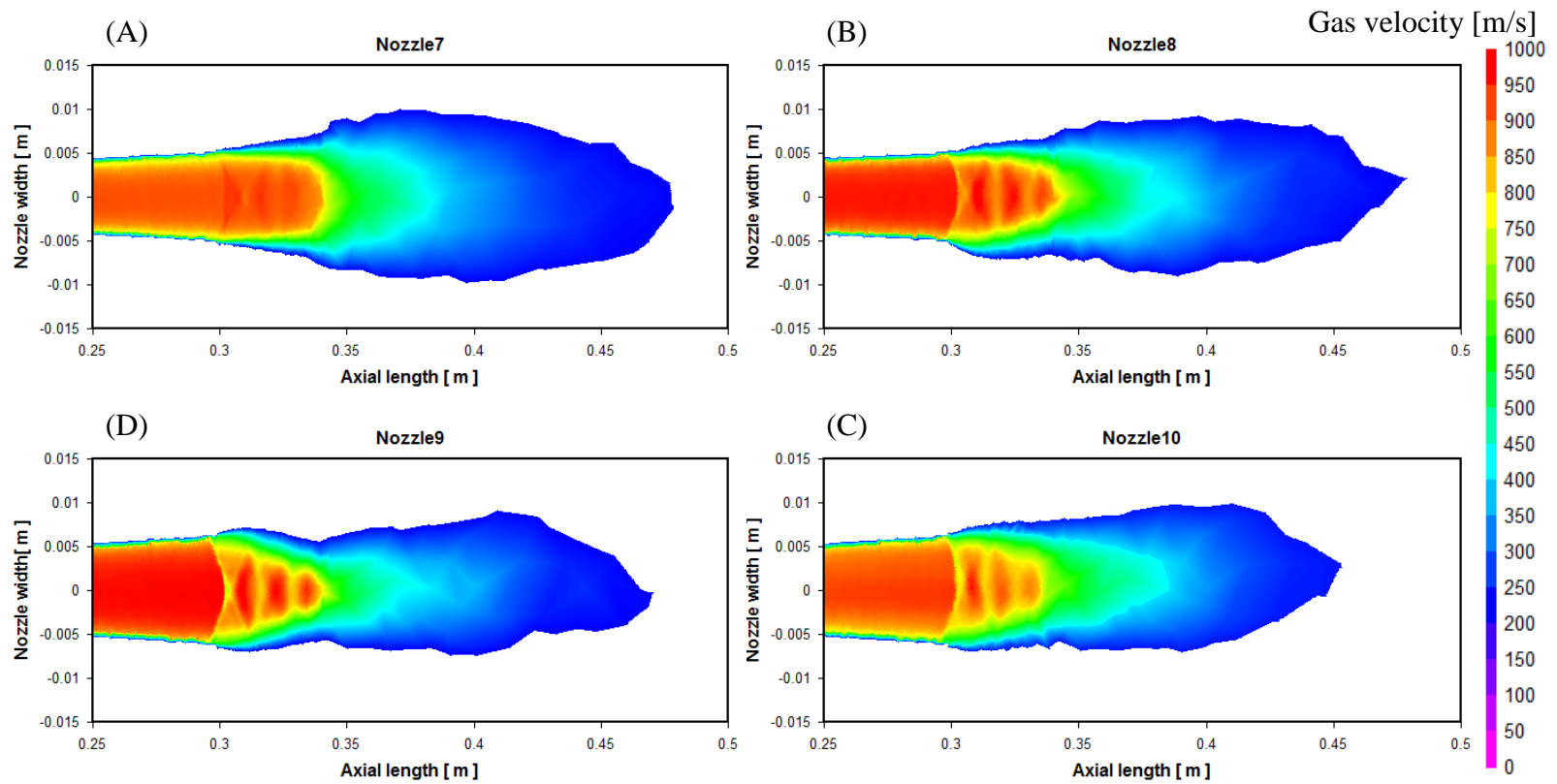


**Figure 5.7: Gas velocity contours (clipped >200m/s) at nozzle exit indicating the operating modes of the nozzle from perfectly expanded to over expanded regimes (A to D)**

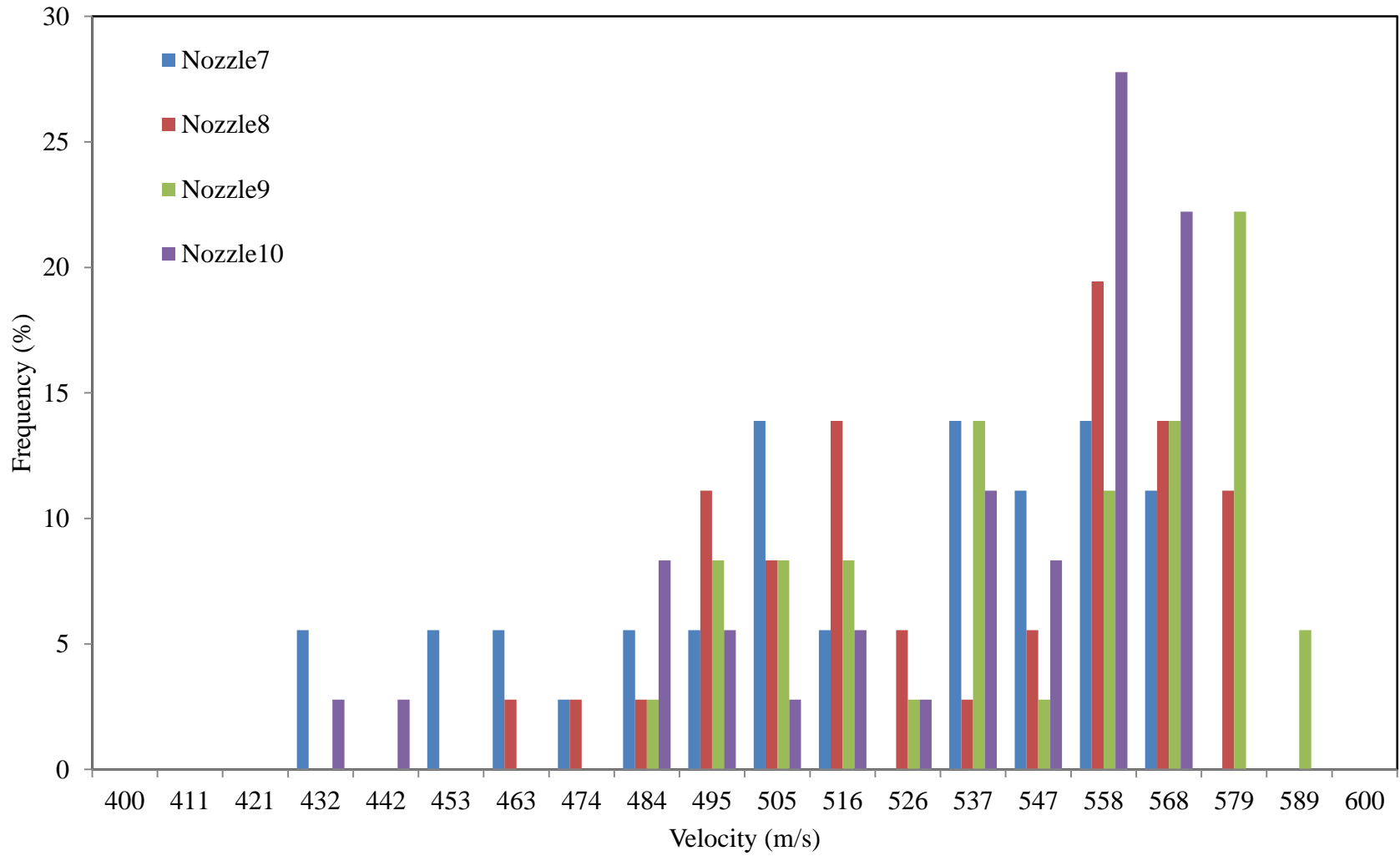


**Figure 5.8: Particle velocity distribution achieved at 10mm standoff from various nozzles.**

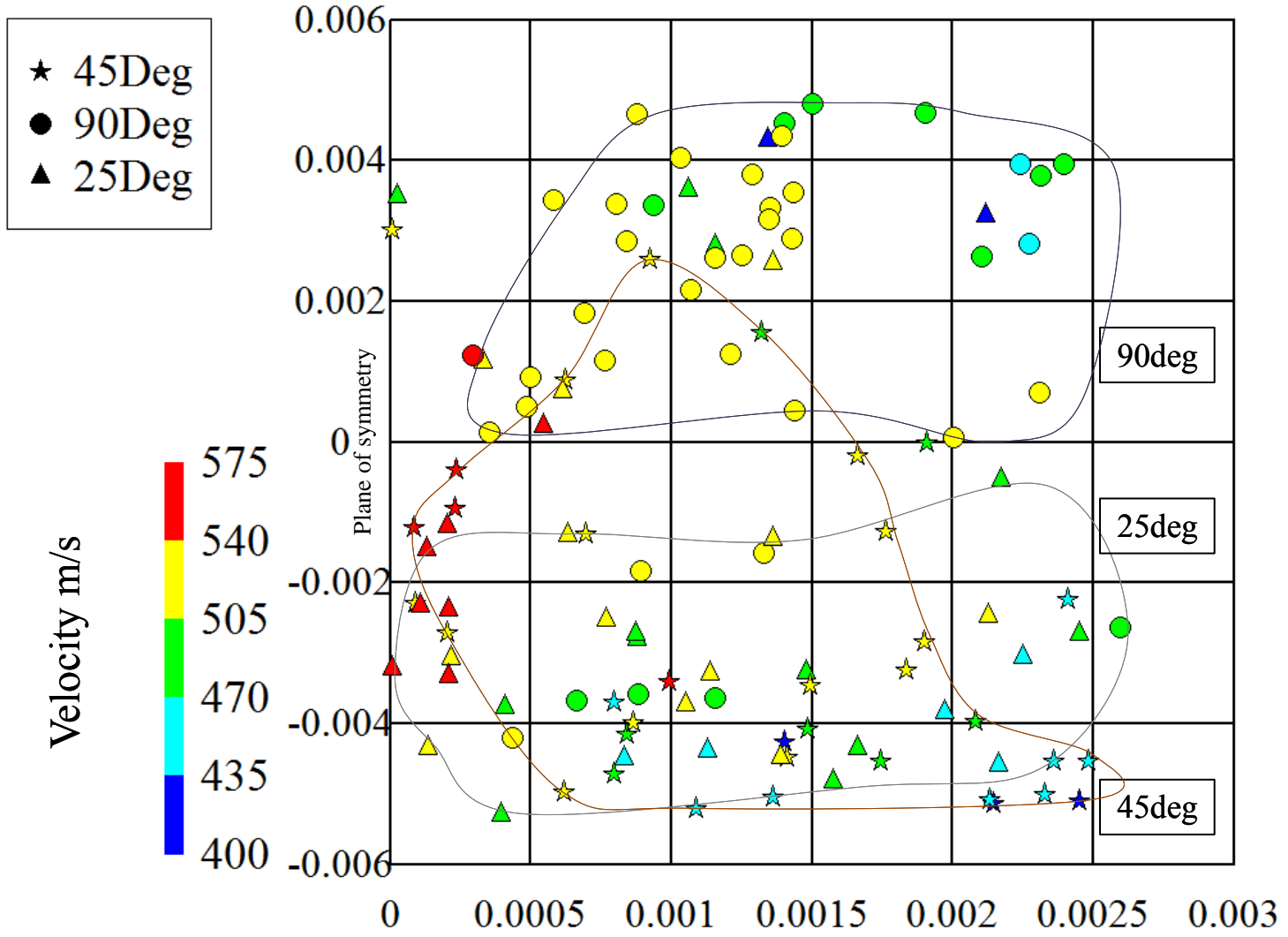


Figure 5.9: Spatial velocity distribution of particles from different injection angles at 10mm plane from nozzle exit



**Table 5.3: Comparison of injection pressure and obtained velocity**

Nozzle	Carrier gas mass flow rate (g/min)	Injection Pressure required for 1 scfm flow rate (psi)	Particle velocity mean (m/s) $\pm$ Std. dev
DI-25	30	185	501 $\pm$ 38
DI-45	30	135	493 $\pm$ 16
DI-90	30	90	510 $\pm$ 24
UI-Axial	30	415	549 $\pm$ 8

### 5.3.1 Experimental verification

In order to substantiate the numerical findings, deposition was conducted on all four nozzles with 45° injection geometry. Crosssection of deposition with SS316 powder is shown in Figure 5.10. Of all the nozzles, deposition achieved with Nozzle8 was significantly thicker. This is also reflected in its deposition weight (Figure 5.11) Hence a combination of expansion ratio of 8.25 with an aspect ratio of 2.5 is a sweet spot to achieve thick coatings.

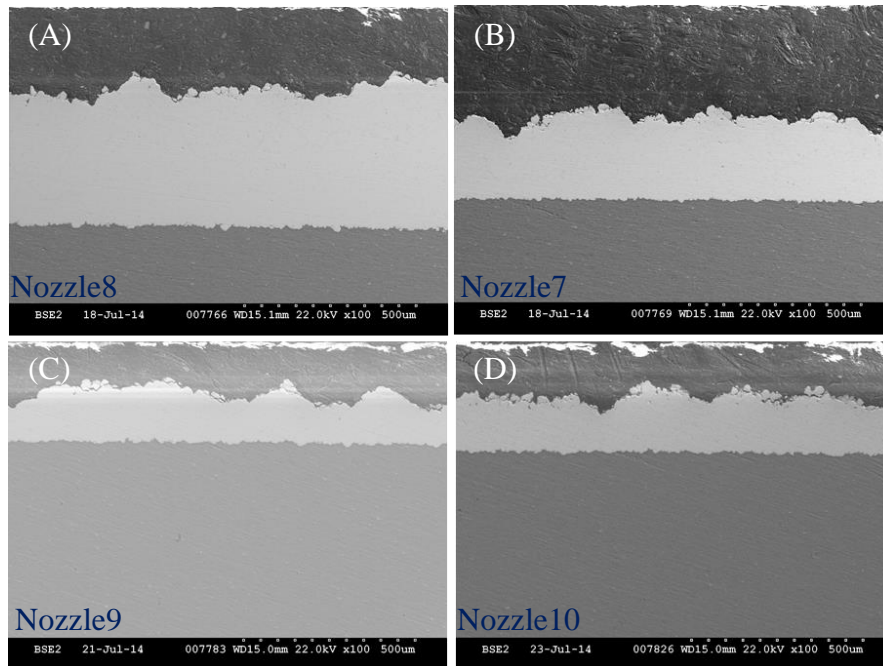


**Figure 5.10: Crosssection of deposition with nozzles listed in Table 5.1**

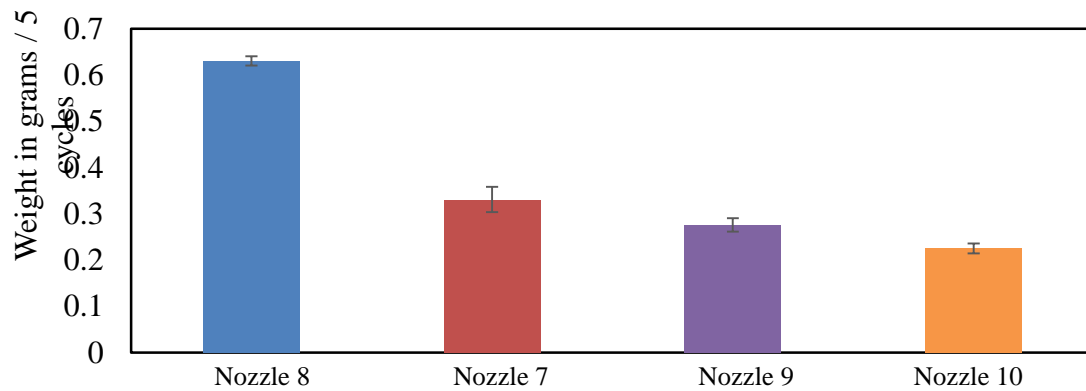


**Figure 5.11: Deposition weights of SS316 alloy with different nozzle geometries**

The XRD peaks of the coatings are shown in Figure 5.12. Based on phases present, the coatings can be split into three categories –completely austenitic, austenitic with some ferrite and ferritic with some austenite: Nozzle9 with deposits that fall into the first category, Nozzle7 &10 with some ferrite and Nozzle8 with some austenite. The phase transformation could be linked to particle velocities, temperature and resulting strain rates. Thus higher particle velocities from Nozzle8 results in higher strain rate leading to phase transformation.

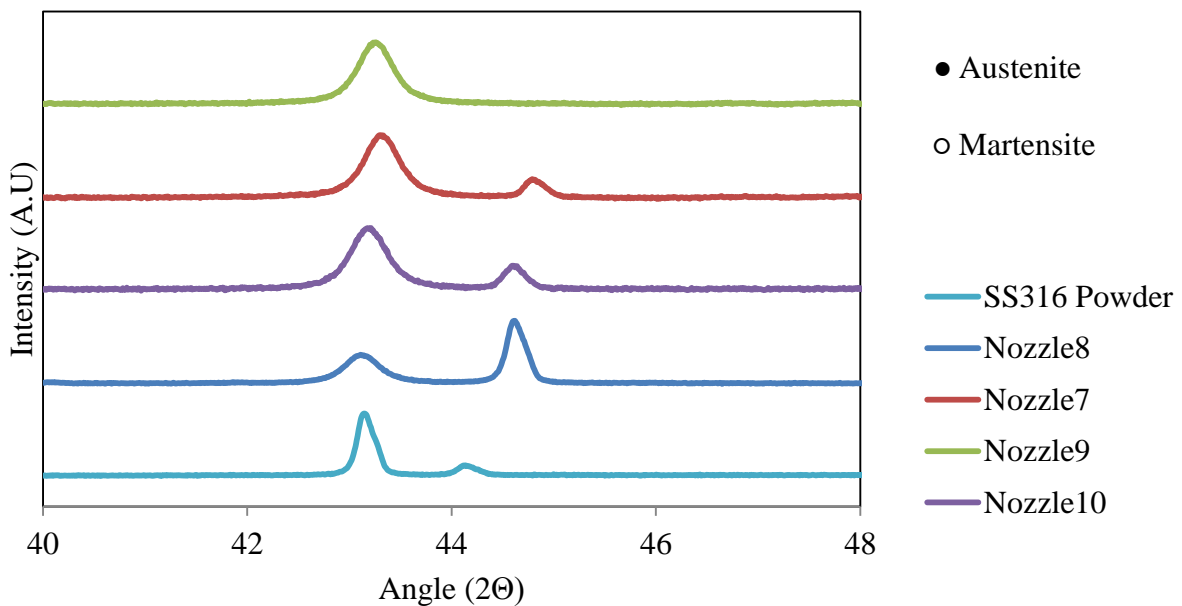


**Figure 5.12: XRD data of SS316 coatings with deposited with different nozzle geometries**

In addition to microstructure analysis, coatings were put to mechanical wear tests with coefficient of friction data plotted over 12 thousand cycles in Figure 5.13. Coatings from Nozzle7&10 present a uniform friction after initial break in period. Nozzle8 coating friction is noisy but uniform and Nozzle10 coating friction is not reliable. To gain more understanding, the profiles of the worn tracks are measured and plotted in Figure 5.14. Despite similar frictional characteristics, Coatings with Nozzle7 and Nozzle10 showed the least and most worn depths respectively. While on the outset worn section progressively follows the expansion ratio of the nozzle and does not seem to be affected by the phase of the material, the excessively uneven frictional characteristics of Nozzle8 coatings could have resulted in higher wear rate

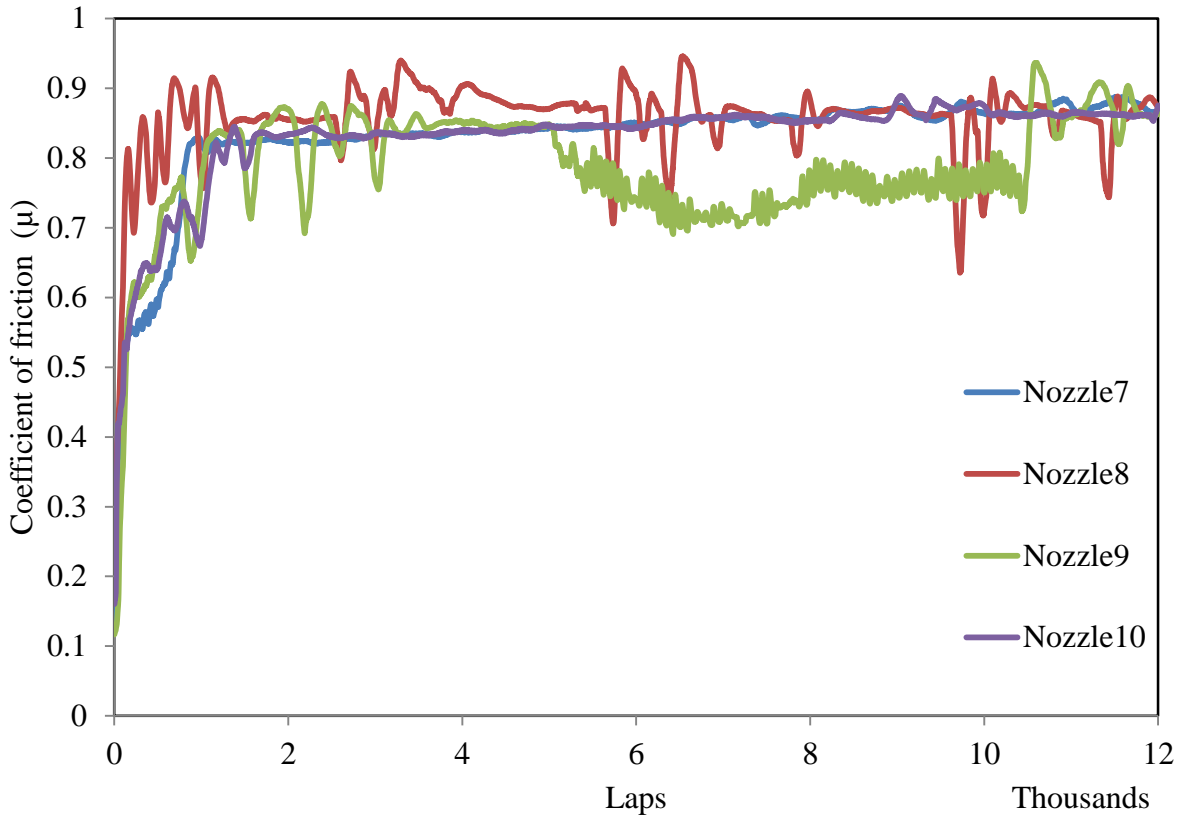


**Figure 5.13: Coefficient of friction of SS316 coatings deposited with the nozzles in Table 5.1**

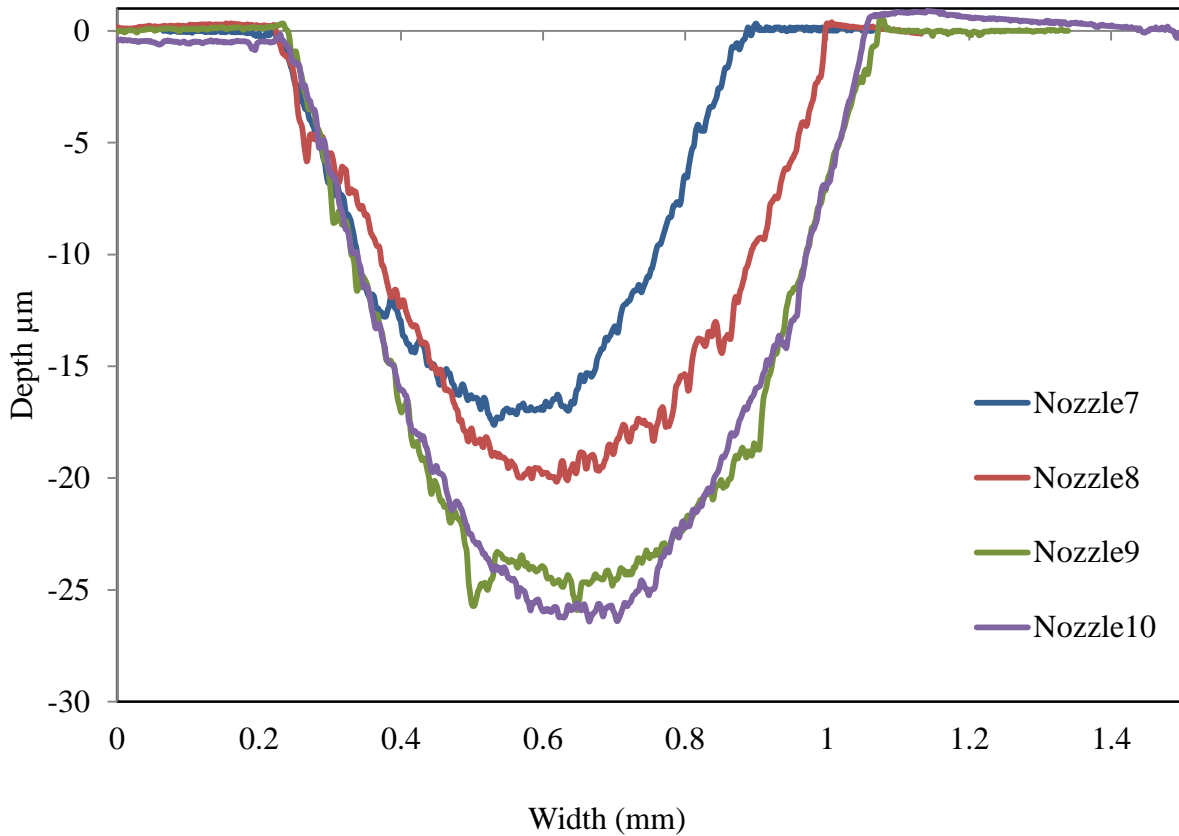


**Figure 5.14: Worn track profile of SS316 coatings deposited with the nozzles listed in Table 5.1**

### 5.3.2 Fe-Mn Deposition parameter optimization:

In order to improve deposition efficiency, the effect of particle size and nozzle traverse rate was studied. Figure 5.15 shows cross sections of deposits sprayed with two different particle sizes. Clearly smaller sized powder showed higher deposition efficiency. This result agrees well with literature and is due to higher particle velocities achieved by the smaller powders. The deposited weight is plotted with respected total spray duration (cycles) and is shown in Figure 5.16. For the initial layers during deposition the weight difference is negligible. This is because of similar deposit efficiency of both powder sizes on aluminum substrate. Beyond the initial deposition layer the increase in deposition weight of smaller sized powders is evident. With increasing number of cycles, there is further reduction in deposition weight with regular size powders. Larger sized powders although below critical velocity, have momentum. This could result in erosive action. Hence -25um or 500mesh powders works best of Fe-Mn alloys.

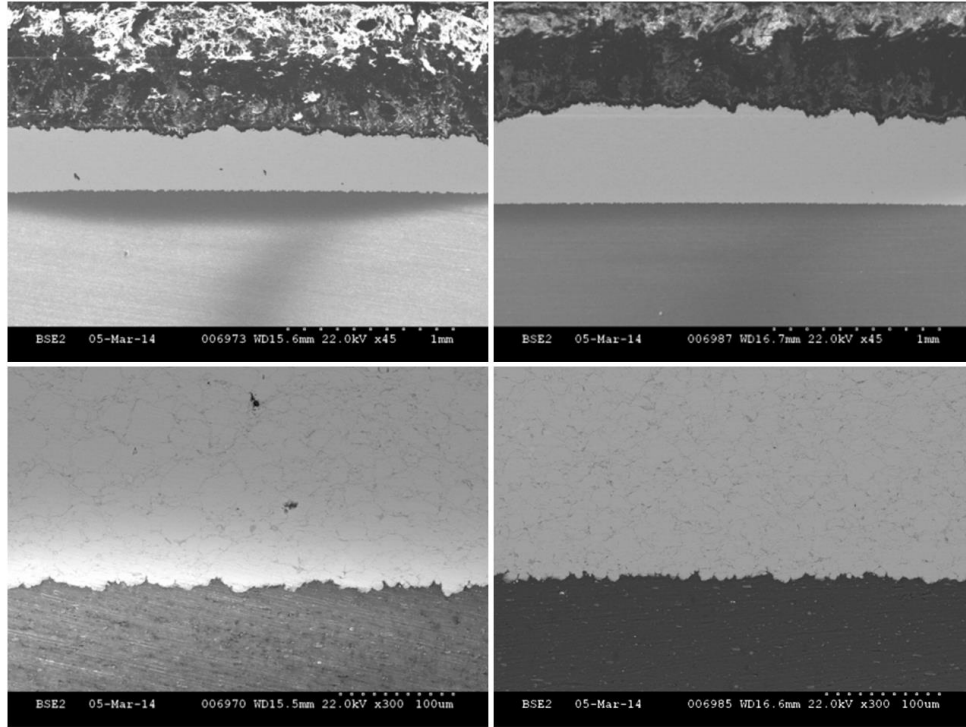


**Figure 5.15: Crosssection of Fe-Mn<sub>2</sub> alloy cold sprayed coatings sprayed with A) -325mesh and B) -500mesh powder**

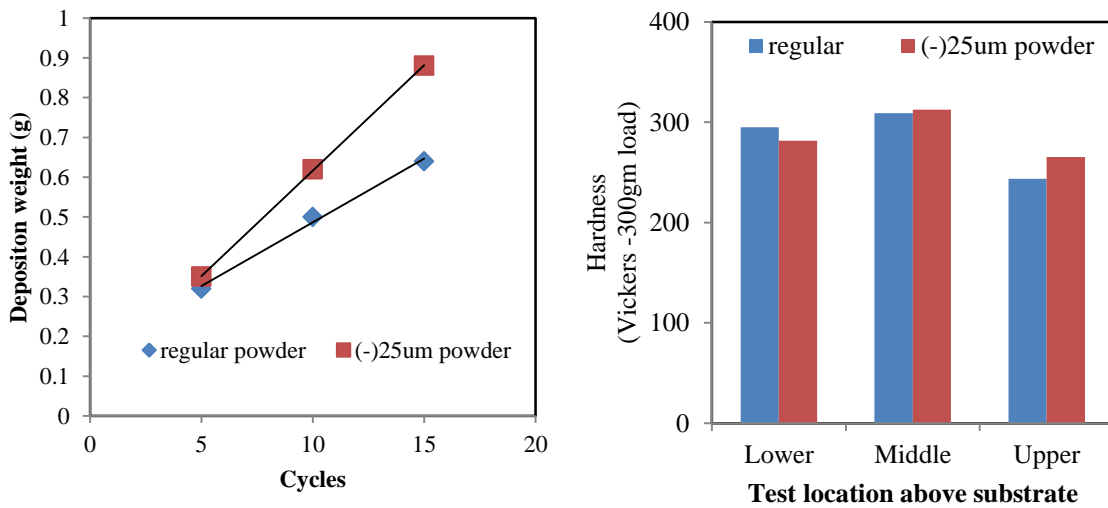


**Figure 5.16: Deposition weight and hardness levels of Fe-Mn<sub>2</sub> coatings deposited with as received powder and that sieved with 500mesh.**

The effect of robot traverse velocity on deposition is presented in Figure 5.17. There was no noticeable difference in crosssection between various traverse rates:- 5, 20, 30 and 50 mm/s. The

deposited weights were also similar. The bond strength of the coating is shown in Figure 5.18. The decrease in bond strength is not evident through deposited weight or microstructure. As the velocity of the particles is significantly higher than transverse velocity, the reduction in bond strength must stem from other reasons. One explanation could be reduced induction time required for deposition to occur. The concept of induction time was introduced by Karimi and co-workers[87]. They noticed that increasing the deposition time resulted in significant increase in deposition rate. Additionally Jordan's lab [88] pointed out that lower scan velocity might results in an annealing action due to higher temperature of exit gas. The surface temperature plot for nozzle scan velocities at for 10 and 50mm/s is shown in figure 4.10. A significant difference in substrate heating can be observed. Higher scan velocities results in more uniform heating at considerably lower temperatures. Hence lower scan velocities could raise the particle impact temperature and ensure higher degree of bonding.

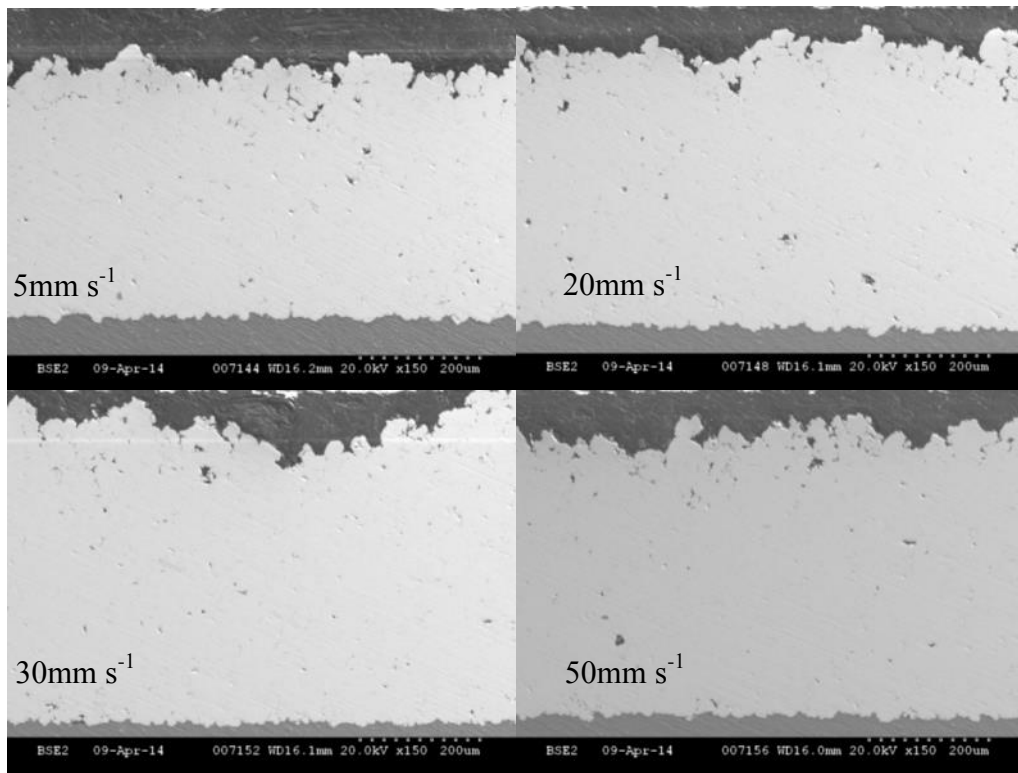


**Figure 5.17: Crossection of Fe-Mn<sub>2</sub> coatings deposited at different traverse velocities**

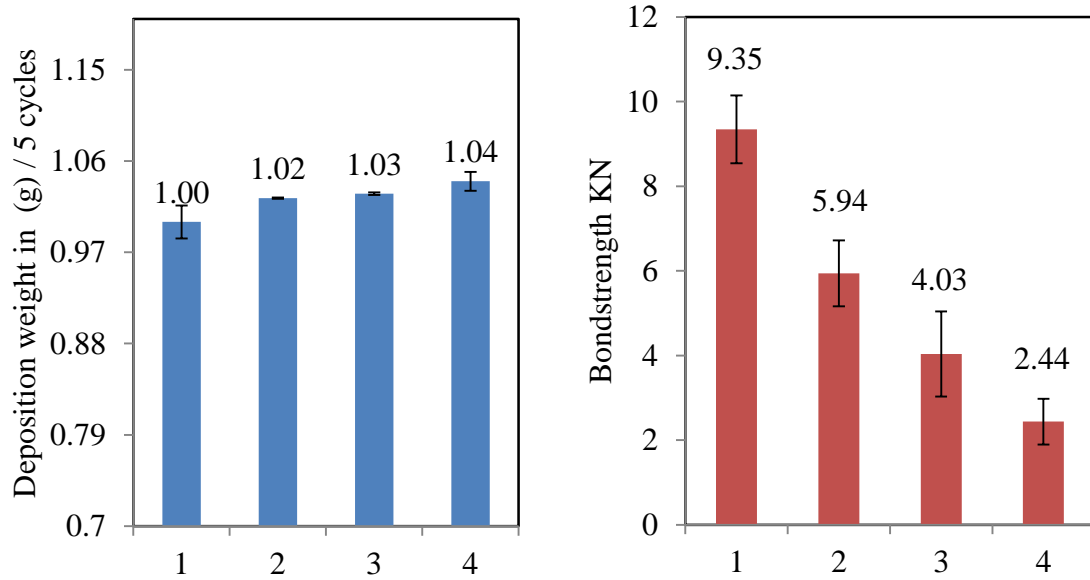


**Figure 5.18: Deposition weight and bond strength of Fe-Mn<sub>2</sub> coatings deposited at 1→5mm/s,2→10mm/s,3→30mm/s and 4→50mm/s**

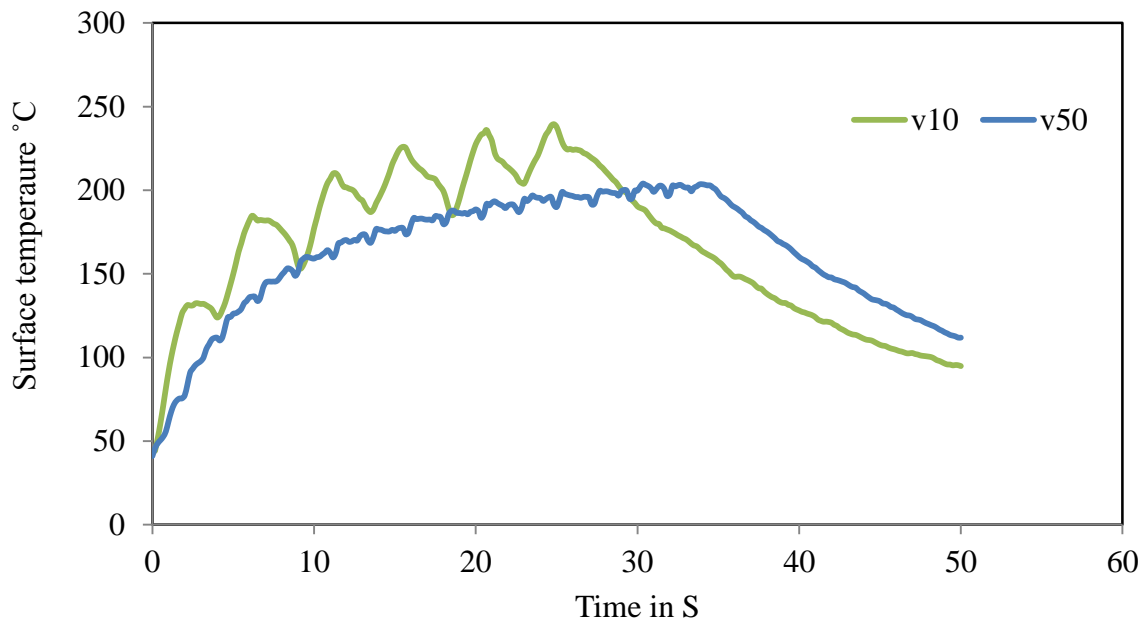


**Figure 5.19: Surface temperature evolution profile during cold spray deposition of Fe-Mn<sub>2</sub> at scan speed of 10 and 50mm/s**

#### 5.4 Summary:

In this study CFD model was verified with experimental study. While high particle velocities were obtained with Nozzle10; Nozzle8 with slight lower expansion ratio gave the best deposition

efficiency. This could be related to higher gas exit temperatures which could help recover cold work on previously deposited layer.

Lower injection angles created lower disturbance in supersonic plume and higher particle velocity. A tradeoff lies between injection pressures and particle velocity distribution.

The best deposit efficiency achieved with Stainless steel powder during nozzle performance study underwent phase change to ferritic lattice. Hence it will be useful to repeat the study with material systems with more tolerant phase systems.

Fe-Mn powder particles above 22microns did not deposit due to lower velocity. These powders hence eroded the coating and are hence undesirable for the process. In general the lower hardness of top layers of the strengthen theory of the tamping effect of subsequent layers during deposition

Lower bond strength at higher nozzle scan velocity must be due to lack of annealing effect to lower cold work or could be due to lower impact temperatures which are detrimental to bonding.



## **6. Cold spray deposition of Fe-Mn coatings for wear resistant applications: Alloying, Microstructure and Property evolution**

### **6.1 Introduction**

High Manganese Iron alloys fall under advanced high strength steels. TWIP (TWinning Induced Plasticity) steels in particular are unique and exhibit high strengths (700-1500 MPa) with good ductility (30-60%), good wear and corrosion resistance [13], [32]. Numerous studies exist on wear and corrosion resistance of these alloys. Choi & Mazumder [89], and Tjong et al [62] found Laser clad Fe-Mn alloys to contain fine grained ferrite and complex carbide precipitation giving rise to significant wear properties. Kim et al [90] tested high temperature wear properties of Fe-XMn-20Cr-1Si alloy. They found at least 10wt% of Manganese was required to improve wear properties. They observed austenite to e-hcp-martensite transformation to be beneficial. Huang and Chuang [19] studied erosion and wear corrosion behavior of Fe-Mn-Al alloys in chloride environment. They concluded acceptable corrosion resistance in mild to moderate conditions. Given the potential features of the high manganese iron alloy system, there is a scope of application for these alloys as wear resistance coating materials.

Cold gas dynamic spray process (CS) is an emerging solid state coating technique. The coating material in the form of powder is accelerated towards the substrate through a supersonic gas stream. Travelling upwards of 500m/s, these powders experience a 'shock state' during the sudden deceleration onto the substrate. It is during the state that an adiabatic softening overcomes the cold working in the material to create necessary plasticity to 'splat' and adhere to the substrate [24], [25]. A series of splats a layered or lamellar interface is created provided sufficient kinetic energy is imparted to the powder. Lack of melting and low to moderate deposition temperatures permits CS to process materials that could not with conventional thermal spray techniques.

While, CS is suitable technique to process high manganese iron alloys by preserving manganese from oxidation and evaporation, its mechanical property is realized through its unique microstructure. In CS the deposited material experiences excessive strain rates ( $> 10^8 \text{ s}^{-1}$ ) as a consequence of shock loading. This creates unique microstructures with high dislocation density and entanglement that retard annealing [23]. Hence the actual performance of high manganese iron alloys will depend on its post deposited microstructure.

The effect of high strain rate on deformation mechanism in Fe-Mn alloys is complex and interesting. In the present study, the material experiences strain rates of upto  $10^8 \text{ s}^{-1}$ . As no literature exists for these materials at these strain levels, review is presented with intermediate strain rates ( $10^3 \text{ s}^{-1}$ ) using Hopkinson bar based methods: Grassel et al. [14] performed tests on a Fe-(15,20,25,30)Mn-(2,3,4)Si-(2,3,4)Al steels and studied its behavior at strain rates of up to 1000/s. They concluded that these steels continue to exhibit high strain hardening behavior combined with a high ability to deform without necking up to very high strain rates. They did not observe any phase transformation with higher manganese steels. Sahu et al. [91] considered the adiabatic temperature rise during dynamic deformation of TWIP steel with and without Aluminum. Using EBSD they observed that at lower strain rates aluminum stabilizes austenite from phase transformations. At higher strain rates Austenite phase was stabilized by dynamic recrystallization and did not depend on Aluminum alloying. Furthermore, the temperature rise leads to an increase of the SFE [92], [93] Therefore, as the temperature of TWIP steel increases, the tendency to twin is expected to decrease. Yet Li et al. [94] reported an increase in the density of generated twins as the strain rate increased. As for studies at even higher strain rates, extensive studies have been performed on Hadfield steels (~12%Mn, 1%C). Chu et al. [95] studied the effect of laser shock processing (LSP) on Hadfield steels. They proposed that the LSP creates e-hcp martensitic plates and widely separated partial dislocations bounded stacking faults which is responsible for the strengthening mechanism. The present material system has not yet been investigated under high strain rate conditions present during cold spray deposition

The main objectives of the current study are to investigate the microstructural characteristics of cold sprayed Fe-Mn-Al-Cr-C alloy (Fe-Mn alloy hereafter). Additionally, cold sprayed stainless steel 316 alloys are studied to contrast the high strain rate behavior of austenitic iron

based alloys. Annealing the powder, as a stress relieving operation prior deposition is explored as a means to improve deposition efficiency.

## **6.2 Experimental**

### **6.2.1 Feedstock, substrate and deposition system**

Gas atomized Fe-Mn powders were used in this study (Praxair, Indianapolis -45um particle size distribution) having a near spherical morphology (Figure 6.1) was used in this study. The basis for the choice of Fe-Mn powder having -45um range was premised on the fact that this particle size range is typical for cold spraying powders. The alloying composition is shown in Table 6.1. Three variations were tested at 25 and 35 wt% Mn levels.

The base material used in this work was 6061 Aluminum alloy with dimensions of 50.8 mm × 25.4 mm x 3.125 mm. Before deposition, the surfaces of base material were polished to 1200 grit and acetone cleaned in an ultrasonic bath for 30 minutes. The powder was then sieved using a 500-mesh vibratory sieve shaker and sprayed onto polished Al-6061 substrates. The cold sprayed system used in this study was developed at the University of Michigan. The system utilizes a rectangular diverging nozzle section with expansion ratio of 8.75 and a diverging length of 275mm (Figure 6.2). A downstream peripheral powder injection scheme is utilized. A conventional thermal spray powder (150psi) Thermach AT1200HP powder feeder is used due to the advantage of lower operating back pressure.

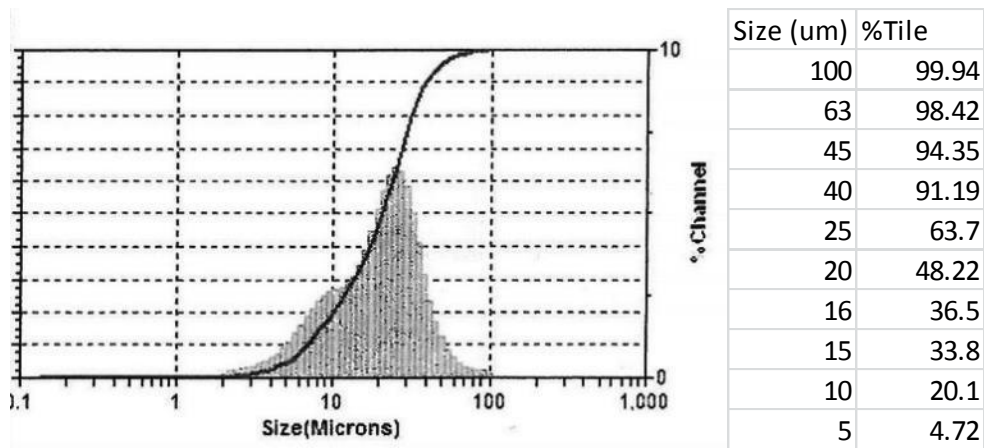
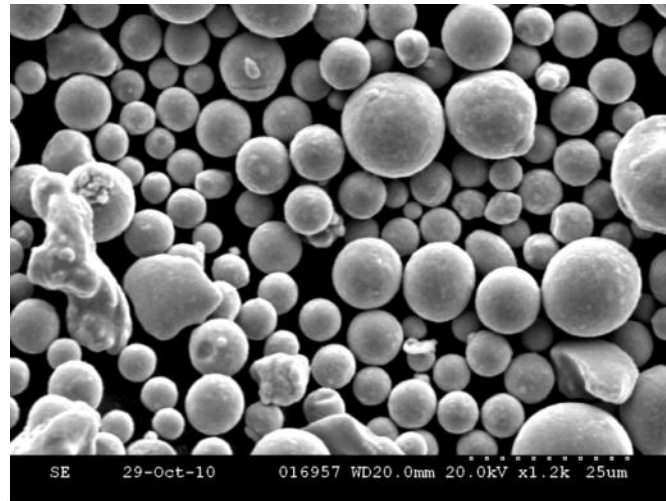
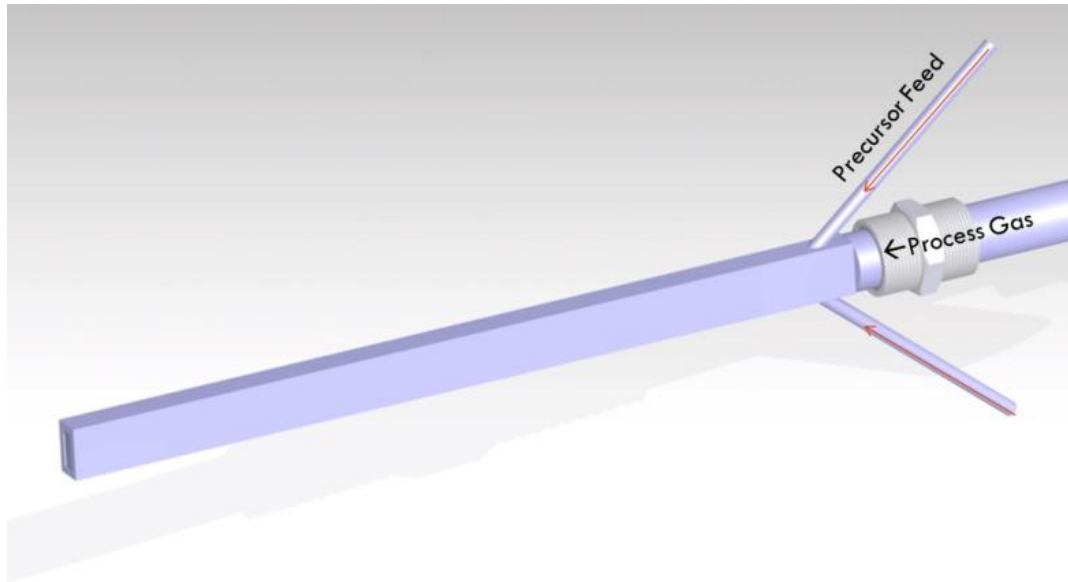


Figure 6.1: Microstructure and size distribution of the powders

Table 6.1: Composition of Fe-Mn powders (balance Fe)

%wt	Mn	Al	Cr	C
Fe-Mn1	25	6	4	-
Fe-Mn2	35	4	2	0.2
Fe-Mn3	25	2	2	0.1



**Figure 6.2: The U of M cold spray nozzle.**

The cold spray processing conditions were previously optimized for this material system. The stagnation conditions of 400psi and 600degC was used. The standoff distance of 10 mm and a traverse feed of 5mm/s was used. Carrier gas was set at 80psi with a powder feed rate of 10g/min.

#### 6.2.2 Stainless steel deposition and feedstock annealing:

Austenitic stainless steel powder (316SS) was deposited to delineate the characteristic of Austenitic Fe-Mn alloy. Further Fe-Mn<sub>2</sub> precursor was annealed in order to assess the effect of stress relieving or grain coarsening on deposition efficiency. The precursor powder was annealed prior to deposition in a fluidized bed at 850degC for 6hours followed by furnace cooling. Argon + 10% Hydrogen gas was used to prevent oxidation of the powders. Table 6.2 lists the chemical composition of the powder before and after annealing process.

#### 6.2.3 Microstructure characterization

Initial characterization of as sprayed cladding was done with scanning electron microscopy (SEM/BSE) on a Hitachi S-2600N SEM to determine the quality in terms of homogeneity, porosity and cracks. Samples used for SEM studies were prepared following standard metallographic procedures. Composition of the coatings was determined with energy dispersive X - ray analysis (EDX) in SEM and back scattered electron imaging was done to obtain

composition contrast. For the phase analysis and crystal structure determination, X – ray diffraction (Rigaku MiniFlex, Cu K $\alpha$  radiation with  $\lambda = 1.5402$  Å) study was conducted. TEM Analysis was carried out on a Hitachi HT7700 microscope. Samples for TEM were thinned in dual beam FIB station (FEI Nova Nanolab)

In order to regulate the powder annealing process, a thorough chemical analysis and size distribution measurements were conducted on sprayed powders before and after heat treatment. A CNO analysis was conducted on the annealed powders using a LECO combustion analyzer. The powder size distribution was measured using micro-trac laser particle size analyzer. This will reveal coalescence of powders during heat treatment.

#### 6.2.4 Wear characteristics

The tribological behavior of the coatings was studied at temperatures at room temperature (RT,  $\sim 25$  °C) using a CSM ball-on-disc tribometer. Prior to testing, samples were polished with 1200 grit SiC polishing paper to avoid excessive tangential loads during testing. Dry sliding tests were conducted in ambient air under a load of 6 N and a sliding speed of 3.25cm/s for a total of 12,000 cycles. A Tungsten carbide 6.25mm ball (McMaster-Carr) was used as a static friction partner. Wear tracks, debris and were analyzed using SEM/EDS.

#### 6.2.5 Electrochemical Corrosion test

The corrosion behaviors of the as-received and annealed claddings were evaluated by using an AMETEK Princeton Applied Research (PAR) Flat Cell model K103. The surface of the corrosion specimens was slightly ground on 1200-grit emery paper, cleaned with acetone in a ultrasonicator and alcohol prior to corrosion testing. Tests were carried out in a 0.5-wt. % NaCl solution which was prepared using analytical grade reagents. The initial pH value of the solution was 5.7 and the initial temperature of the solution was at 20°C. Prior to the polarization scan the samples were kept in solution to establish the free corrosion potential ( $E_{corr}$ ). Anodic polarization tests were carried out in a 0.5-wt. % NaCl solution which was prepared using analytical grade reagents. The initial pH value of the solution was 5.7 and the initial temperature of the solution was at 20°C. The specimen was driven from an  $E_{corr}$  of  $-1$  to 2V (vs ref) at a scanning rate of 1.66 mV/s to produce potentiodynamic polarization plots. All potentials were measured with reference to a standard saturated calomel electrode (SCE).

### 6.3 Results and discussion

Optimization of the cold spray deposition of Fe-Mn alloys is discussed in chapter 4. A closer look at the phase and property evolution of cold sprayed Fe-Mn coatings is the focus of this study. SEM images of three alloys are shown in Figure 6.3. Dense coatings are obtained for these alloys. EDS analysis reveals compositional tolerance with actual powder specification.

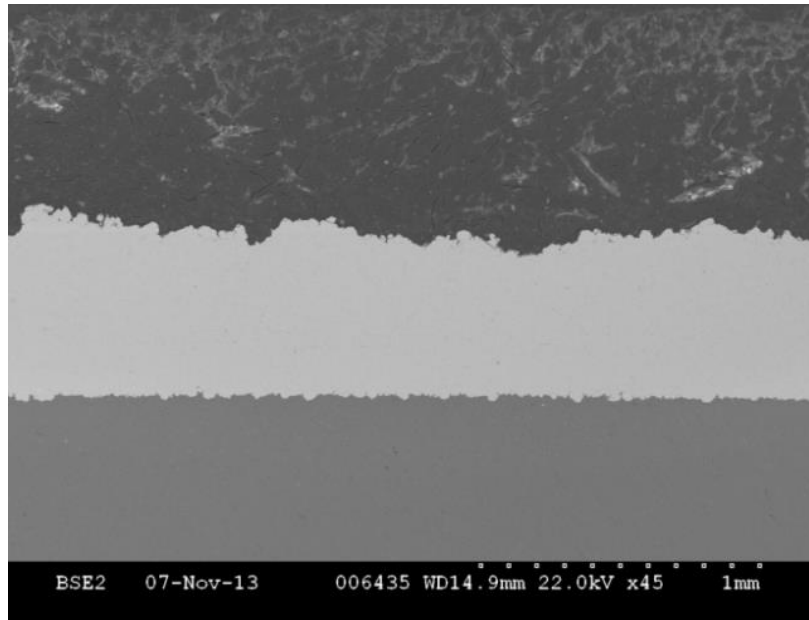


**Figure 6.3:** Cross section BSE image of cold sprayed Fe-Mn alloy coatings

Figure 6.4 shows TEM bright field image of the deposited coating. The direction of coating build up is demonstrated with the direction of the arrow. A change in grain size is observed across the deposition indicating relaxation and recovery of cold work with progressive deposition.

Change in phase is more evident in the X-ray diffraction (XRD) patterns. The results of phase characterization are more interesting due to significant phase change observed in deposited powder. While phase preservation is a distinctive characteristic of cold spray, with the high strain rate nature of the process it is not un-common to observe phase transformation. The XRD pattern of the as received powders and that of deposited coatings are presented in Figure 6.5. A majority of austenite phase with significant ferritic phases is seen for coatings sprayed at identical deposition condition.

Similar phase change is observed in cold sprayed SS316 powders. Hence the transformation could be related to stability of austenitic phase at high strain rates. Borchers et al [96] have shown that during explosive welding of stainless steel powders a mild amount of hcp martensite is formed.

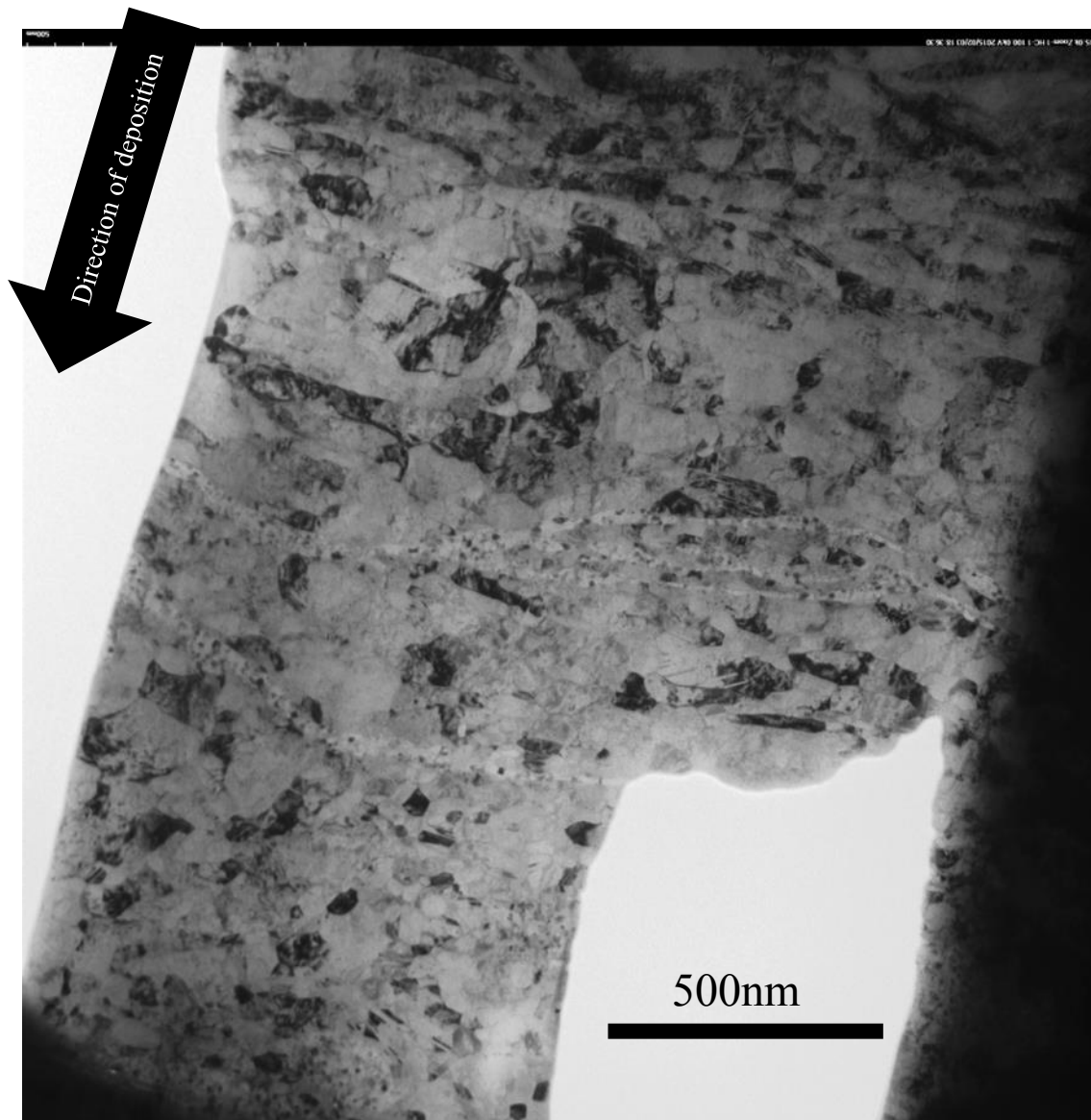


**Figure 6.4: Bright field TEM image of cold sprayed Fe-Mn<sub>2</sub> alloy coating**



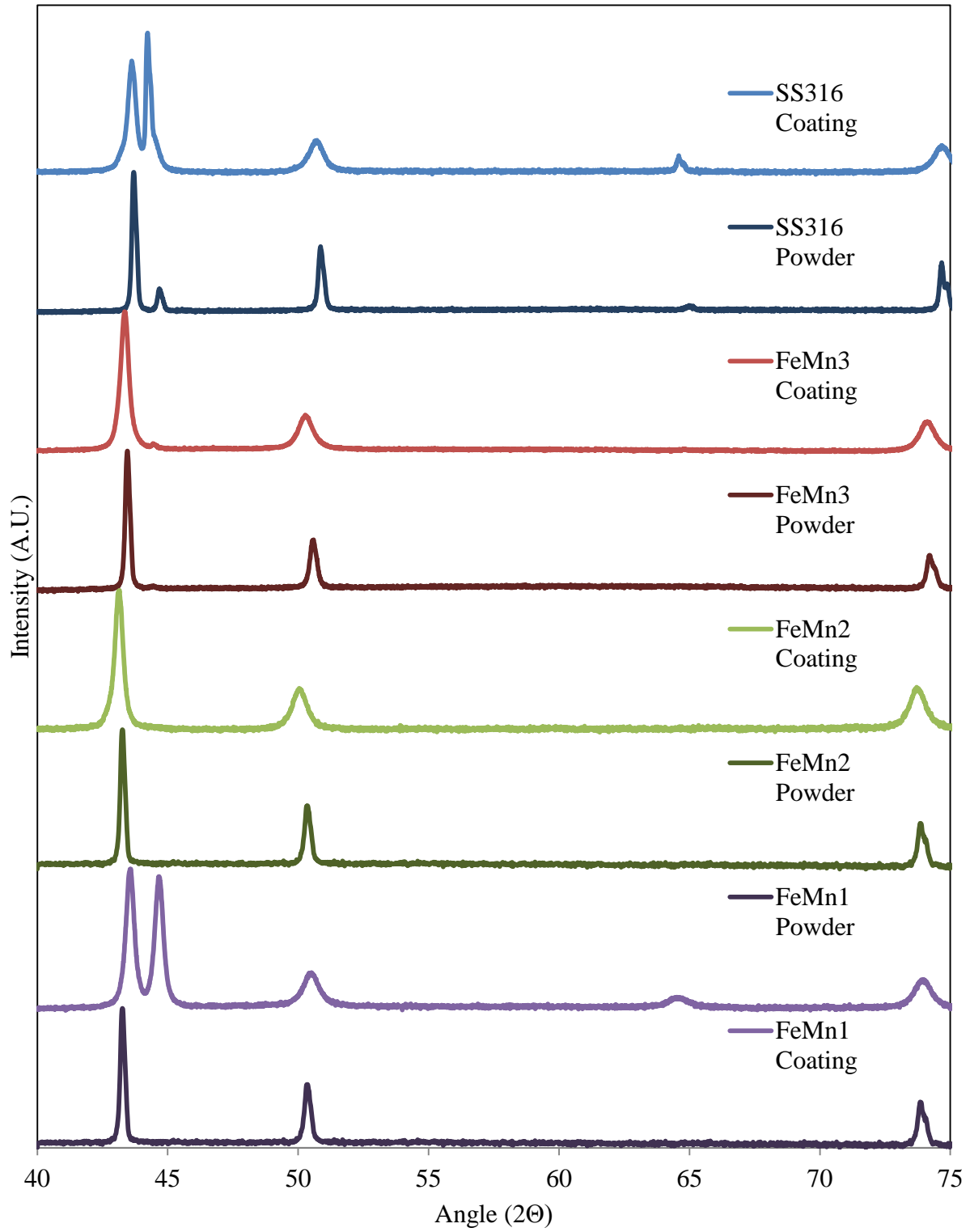


Figure 6.5 XRD patterns from Fe-Mn and SS316 precursor powder and deposited coatings

### 6.3.1 Annealing treatment on powders:

The variation in Carbon Nitrogen and Oxygen (CNO) are presented in Table 5.2. There was significant reduction in oxygen content which is beneficial during cold spray deposition [97]. No changes were observed in both interstitial alloying elements – Carbon and nitrogen.

**Table 6.2 CNO analysis results of the Fe-Mn<sub>2</sub> Alloy powder**

	As-received	Annealed
<b>Carbon</b>	0.21	0.21
<b>Nitrogen</b>	0.0098	0.011
<b>Oxygen</b>	0.18	0.097

During heat treatment, the powders could coalesce increasing their sizes. The increase in size of powders will affect deposition efficiency. The results of size distribution analysis of the powder before and after annealing treatment and micro hardness of the powders are presented in Figure 6.6.

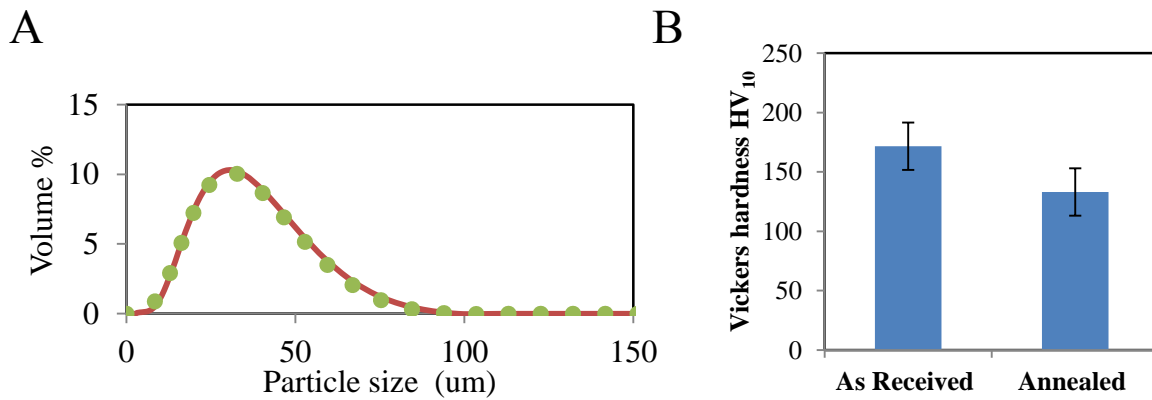


**Figure 6.6: Size distribution (A) and micro hardness (B) of Fe-Mn<sub>2</sub> powders before and after (dotted) annealing**

The effect of annealing treatment on the powders is also presented with the XRD peaks. The coating microstructure is similar to that of non-treated powders Figure 6.7. The phase on the other hand reveals a whole new story. The secondary and tertiary peaks are absent in coatings deposited with heat treated powders. While phase transformations in cold sprayed stainless steel

deposits are beyond the scope of this chapter, it is interesting to note the contrasting effect of heat treatment on the two different austenitic material systems.

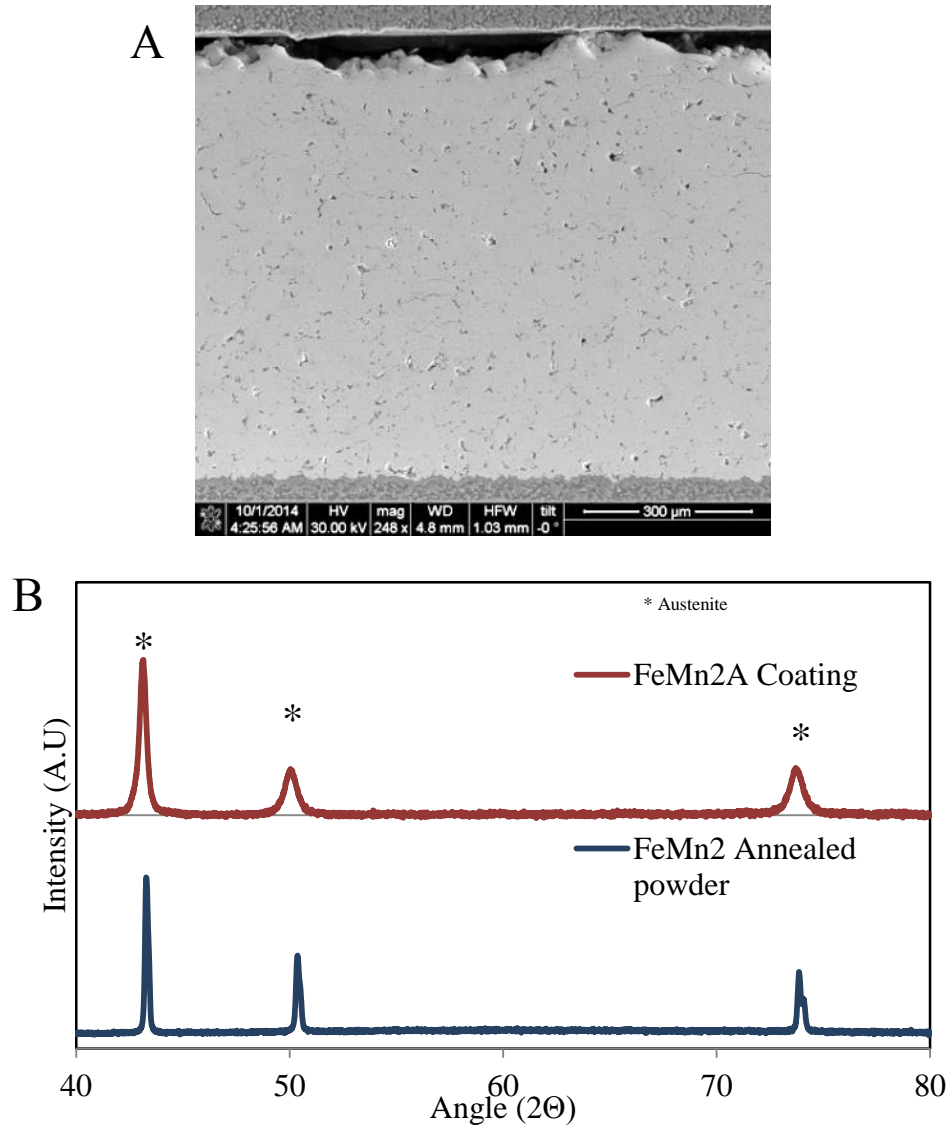
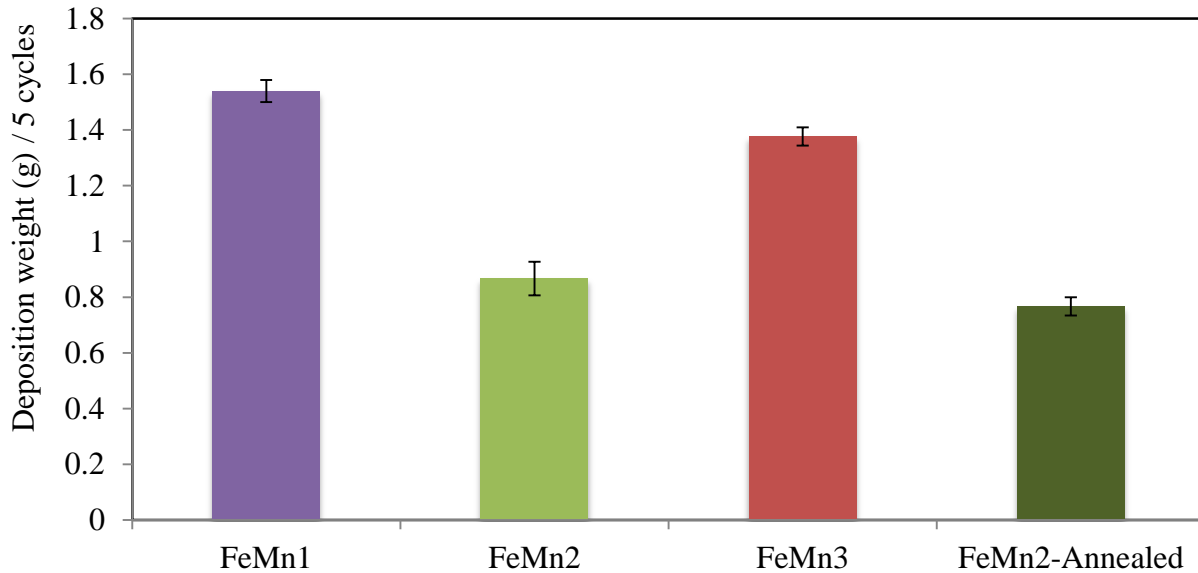


Figure 6.7: SEM (A) and XRD (B) of Fe-Mn2 coatings deposited with annealed powders

### 6.3.2 Deposition efficiency:

The deposition rate of the three different alloys is shown in Figure 6.8. Fe-Mn1 showed highest deposition efficiency as well as maximum phase change during deposition, therefore inducing austenitic to ferritic phase change could be beneficial with respect to deposition. Although the reduction in oxygen levels and hardness might appear favorable for deposition, the deposition

efficiency is slightly lower for annealed powders. A further investigation is needed as to understand the reason for reduction in deposition efficiency.



**Figure 6.8: Deposition rates of various powders**

### 6.3.3 Wear testing:

The friction force was recorded continuously during wear test and the evolution of the coefficient of friction (COF) is plotted in Figure 6.9. The Fe-Mn1 alloy exhibits the highest friction levels of about ~0.9. The Fe-Mn2 and Fe-Mn3 exhibit similar frictional levels of around 0.8. The coating deposited with annealed powder is presents highest COF. Both Fe-Mn2 and 3 alloys exhibit a delayed stabilization with Fe-Mn3 taking longer than Fe-Mn2. The worn profile (Figure 6.10) reveals further on the wear resistance of these alloys. Fe-Mn1 shows highest wear rate which could have resulted in the increase in COF. Worn sections of Fe-Mn2 and 3 are relatively similar. Unlike laser clad Fe-Mn alloys, the wear rate seems related to the deposition efficiency. Alloys with higher deposition efficiency had higher wear rates.

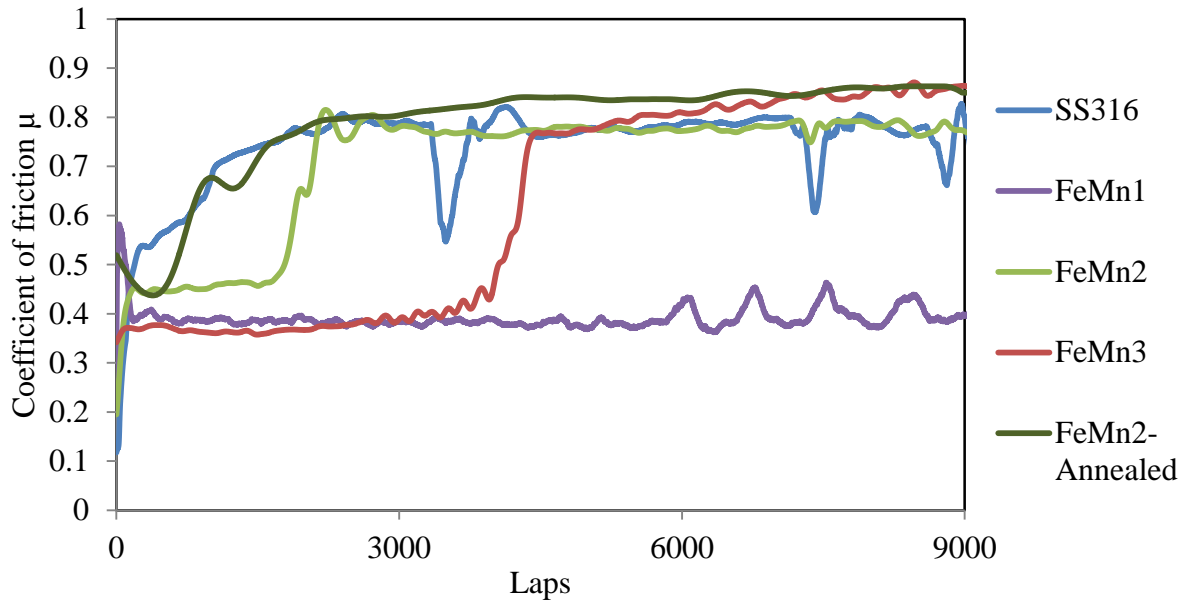


**Figure 6.9: Coefficient of friction of Fe-Mn alloys**

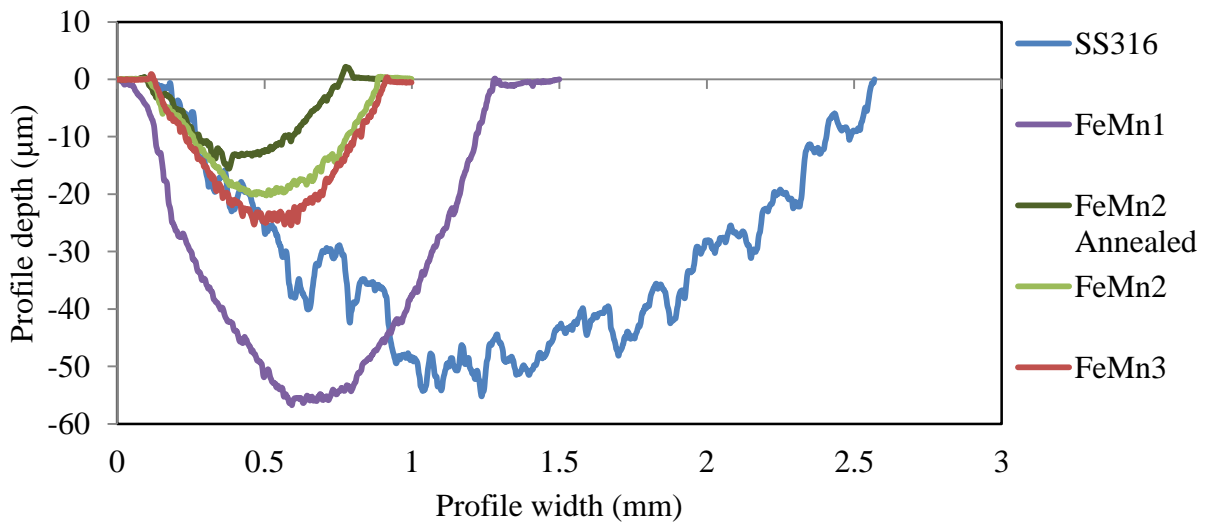


**Figure 6.10: Surface profile of worn track section after wear tests**

#### 6.3.4 Open Circuit Potential - Time Measurements

Corrosion studies were performed on Fe-Mn1, 2, 2A, 3 and SS316 coatings. The open circuit potential (OCP) – time plots are shown in Figure 6.11. In all samples, the OCP was drooping with time and dropped  $\sim 0.01\text{V}$  within one hour. This steady reduction in OCP could be due to

lack of passivation of the alloys in Chlorine environment [22]. The OCP of Fe-Mn3 was closest to that of A356. The OCP of A356 Aluminum alloy was fairly stable within the hour but has a much lower potential value.

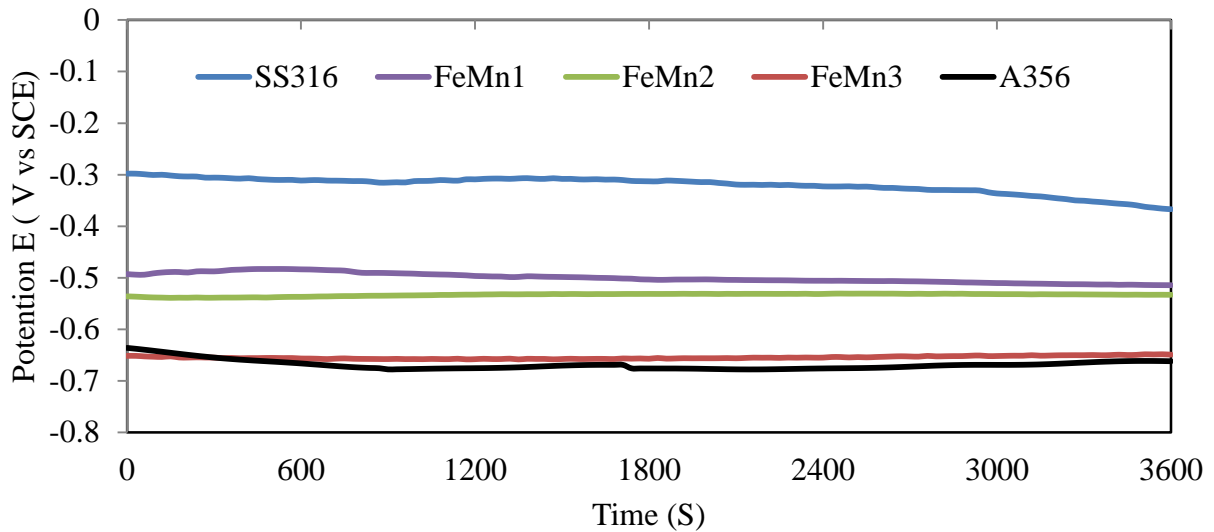


Figure 6.11: Open circuit potentials (OCP) of Fe-Mn alloys in 0.5% NaCl solution

### 6.3.5 Potentiodynamic Polarization

The typical Potentiodynamic polarization behavior of pure A356 Aluminum substrate and deposited coatings are shown in Figure 6.12. The interpolated corrosion potentials and current densities are presented in Table 6.3. SS316 exhibits passivation which clearly delineates from Fe-Mn specimens. The absence of passivation behavior of the Fe-Mn alloys is similar to that found prior literature [22]. Fe-Mn1 alloy exhibited superior corrosion characteristics to stainless steel 316 alloy. This could be due to presence of multiple phases in the coatings which is absent in conventional stainless steel materials which are completely austenitic. Fe-Mn3 alloy and A356 alloy had similar corrosion potentials which could reduce galvanic coupling. A cross-section of the specimens after testing is shown in Figure 6.13. All the coatings have lost similar amount of material. The only difference was that in Fe-Mn1 alloy, there were islands of unaffected material. These islands did not show any compositional contrast in the back scattered electron images. The stainless steel coating exhibited least amount of material loss after testing's but there was evidence of crevice corrosion which occurred through to the coating – aluminum interface.

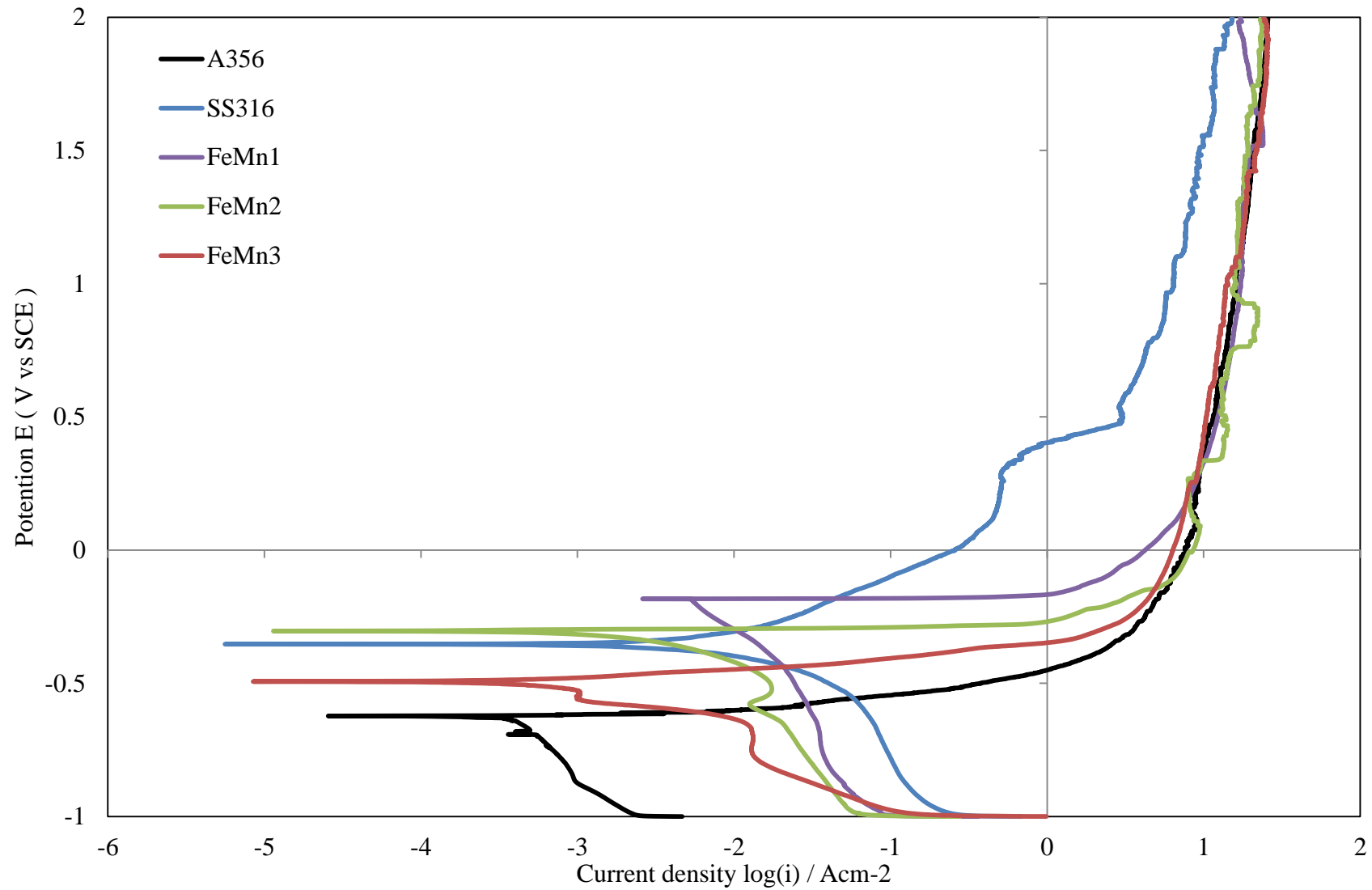
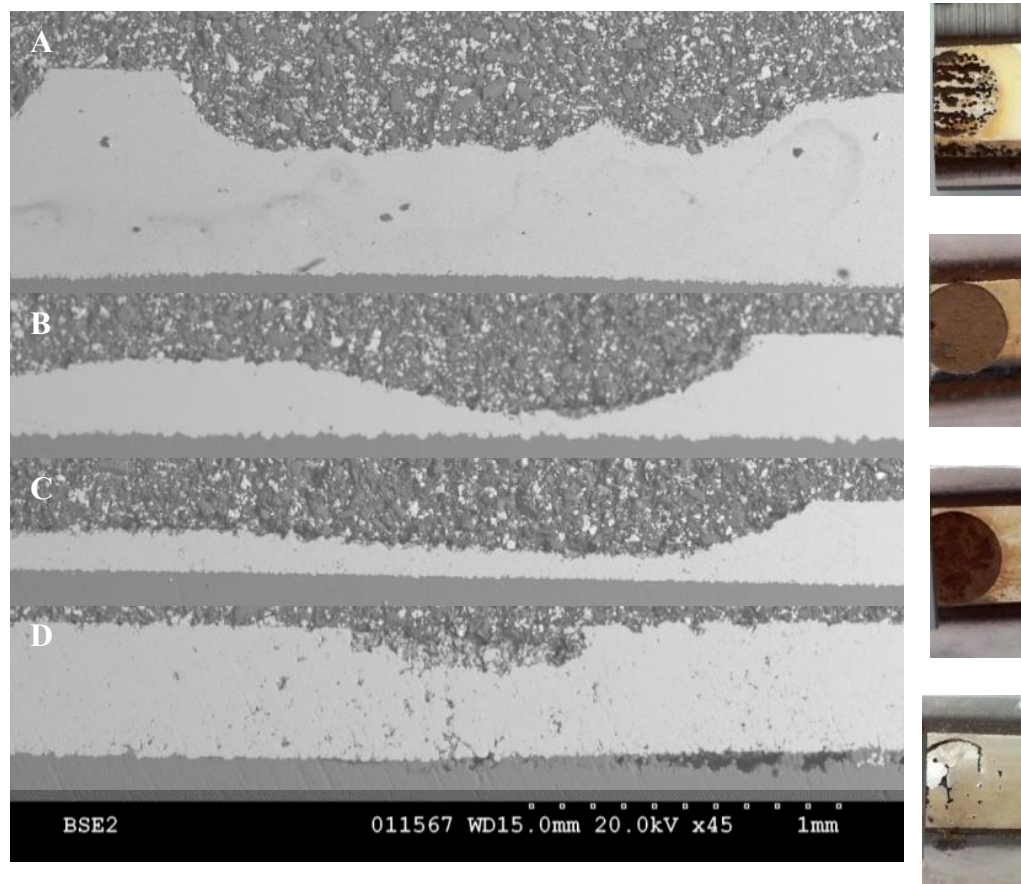


Figure 6.12: Potentiodynamic polarization plot of Fe-Mn alloys in 0.5% NaCl solution

**Table 6.3: Tafel interpolated corrosion potential and corrosion current density**

	<b>E<sub>corr</sub> (mV)</b>	<b>I<sub>corr</sub> (<math>\mu\text{A cm}^{-2}</math>)</b>
<b>Al356</b>	-615.588	0.412
<b>SS316</b>	-341.341	9.961
<b>Fe-Mn1</b>	-207.292	12.032
<b>Fe-Mn2</b>	-316.302	3.992
<b>Fe-Mn3</b>	-507.647	0.556



**Figure 6.13: Crosssection of samples after Potentiodynamic testing Fe-Mn1 (A) Fe-Mn2 (B) Fe-Mn3(C) and SS316 (D)**



## 6.4 Summary

Novel Fe-Mn cold sprayed coatings were deposited. Three different Fe-Mn compositions were tested and analyzed. In addition annealing of the powders was performed as a means to improve deposition rate. A higher level of manganese will result in lowering of the stacking fault energy which arrest dislocation movement. This is not preferred for cold spray deposition. This translated into lower deposition rates with this material compared to convention Fe based materials. Increase in Mn content results in that a larger number and wider stacking faults which inhibits the movement of dislocations during the cold work process. Accordingly, it would be rational to assume that cold worked Fe-Mn alloys will be significantly harder and crystallite size will be significantly smaller than those values found in laser clad samples (Chapter 3). The following conclusions can be derived from this study:

Dense Fe-Mn coatings were obtained with cold spray deposition. There was a phase change observed from austenite to martensitic and or ferritic phases at lower manganese contents. A similar phase change was observed in deposited stainless steel 316 coatings. Hence phase transformation could have resulted from the high strain rates experienced by the material during deposition.

- Annealing of the powders did not help to increase deposition efficiency. Hence increase relaxation and increase in grain size that accompanies with the heat treatment was detrimental for cold spray deposition.
- Wear performance of coatings was independent with respect to manganese content or phase of the material. Instead, coatings with higher deposition efficiency exhibited poor wear resistance. Hence wear resistance could be directly related to degree of cold work or recovery in the coatings.
- The corrosion resistance of the alloys did not follow the same trend as laser clad alloys. The corrosion was more susceptible to Al and Cr levels than that of Mn. The presence of dual phase in Fe-Mn1 alloy enhanced its corrosion resistance and was superior to SS316 cold sprayed coating.

## **7. Coaxial laser assisted cold spray deposition of Fe-Mn Alloys: Microstructure characterization – process development**

### **7.1 Introduction**

Cold gas dynamic spray or simply Cold Spray (CS) is a unique solid state deposition process. In this process a high strain rate plastic deformation helps bind metal or plastic powder particles to form a coating. A combination of particle size and velocity helps adiabatic softening overcome strain rate hardening. These results in mutually confirming surfaces to form a coating, although cold working –residual strength-fairly advantageous it may not be suitable for many materials. Harder materials do not and require higher velocities The temperatures reached in the material are fairly low and presents an ability to deposit a materials that were require inert/vacuum environment.

A serious problem faced by the cold spray process is its dependence on material property of both the deposited material and target. Newer coating material formulations such as amorphous and max phase materials still suffer low deposition rates when deposited with high performance cold spray systems [98]. These materials which contain complex alloying to preserve its property fail to yield at fast time scales imposed during cold spray operation. Target materials such as cast iron, stainless steel, nickel and titanium alloys present challenges due to lack of compliance during particle impact. These factors limit cold spray commercialization to niche applications where material preservation from oxidation and thermal degradation are paramount. In order in to penetrate the main stream coating industry, the coated-material dependence of cold spray process must be decreased.

A limitation of the process has been carefully expressed in terms material eligibility by Vlcek et al [55] (also described in the literature review chapter). In that the success of the process is largely dependent on the ability of both the coating material and the substrate to form confirming surface [25]. Hence understanding the mechanical property of the material under cold spray

conditions is paramount. The accelerating gas velocity is limited by the maximum temperature and pressure it achieves at the inlet. For hard materials these numbers are often insufficient. Systems can be built to withstand higher pressure and temperature but this inevitably affects the cost of the system. Vleck has proposed that a materials peierls stress and its stacking fault energy will determine its ability to deform during cold spray. The effect of high strain rate sensitivity is not considered.

In the cold spray domain, an increase in spray ability corresponds to a higher fraction of the particles travelling beyond critical velocity. Hence reducing the critical velocity or threshold for deposition, holds the key for improving deposition at a given gas stagnation pressure and temperature. Assadi [24] and Schmidt [40] have experimentally derived empirical formulae to estimate this velocity as described in the literature review section.

$$v_{cr} = 667 - 14\rho + 0.08T_m + 0.1\sigma_u - 0.4T_i \quad \text{Eq 7.1}$$

where  $\rho$  the mass density in g/cm<sup>3</sup>,  $T_m$  is the melting temperature in °C,  $\sigma_u$  is the ultimate strength in MPa, and  $T_i$  is the initial particle temperature in °C.

Careful review of existing literature confirms all techniques used to improve deposition efficiency falls into modifying these two factors. In one, the powders undergo thermal treatment via heating of the carrier gas or by increasing dwell time in the stagnation region of the cold spray nozzle [30], [31], [42]. Here the powder is annealed and experiences an in-flight softening enhancing deposition. The process requires precise control of particle temperature often fouling and clogging the nozzle orifice. In the second category, the substrate temperature is increased and increase in deposition rate has been recorded in several investigations [29], [99], [100].

While softening the material is the objective in both cases, the difference lies in when it occurs. Success in softening of the coating which is post deposition is limited by material being deposited. In larger parts, Laser Power Intensity, Absorptivity and Thermal conductivity of the coated material will dictate the overall efficiency. Softening of the in-flight particles which is prior –deposition overcomes these advantages as at any given time, the Laser will soften a pre-determined amount of precursor. A suitable balance between laser power and particle velocity will ensure successful deposition.

In this study, the role of laser assisting techniques on temperature rise is investigated. Laser assisting technologies are becoming increasingly prevalent for coating production [101]–[107].

Lasers result in electromagnetic energy is used to vibrate atoms in the lattice causing heating. The strength of the electromagnetic energy attenuates to near surface levels resulting in localized and instantaneous rise in temperature. Temperature is then conducted through the rest of the substrate. Based on spatial and temporal intensity of the laser beam, this temperature rise, viz the heat affected zone could be negligible. The use of laser is beneficial in two routes. The first one is the actual deposition temperature that reduces critical velocity and improves deformation rate and bonding (cohesive and partly adhesive). The second is the ablation of surface contaminants such as oxides and residue from cutting fluids. This also enhances bond strength. The PROTAL process shown in Figure 7.1 is one of earliest available literatures on the use of lasers with a cold spray process.

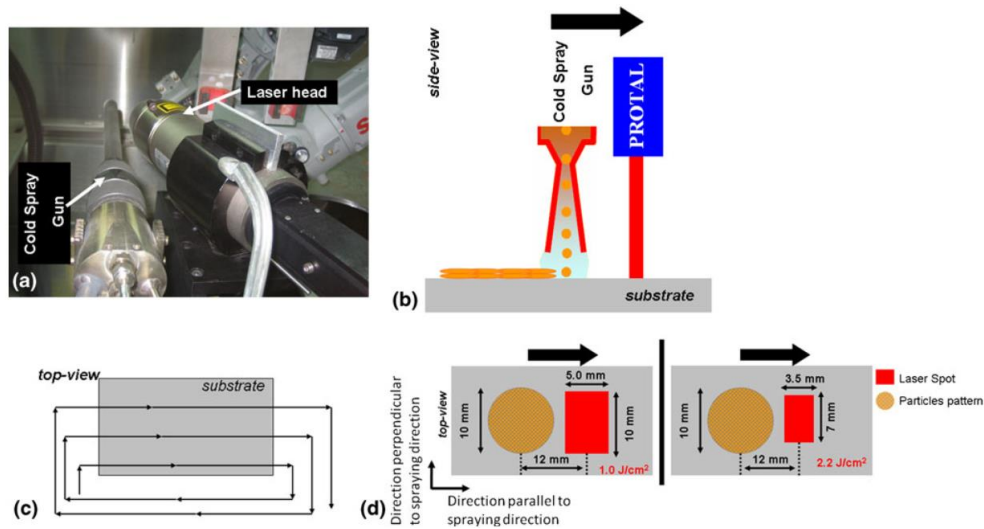


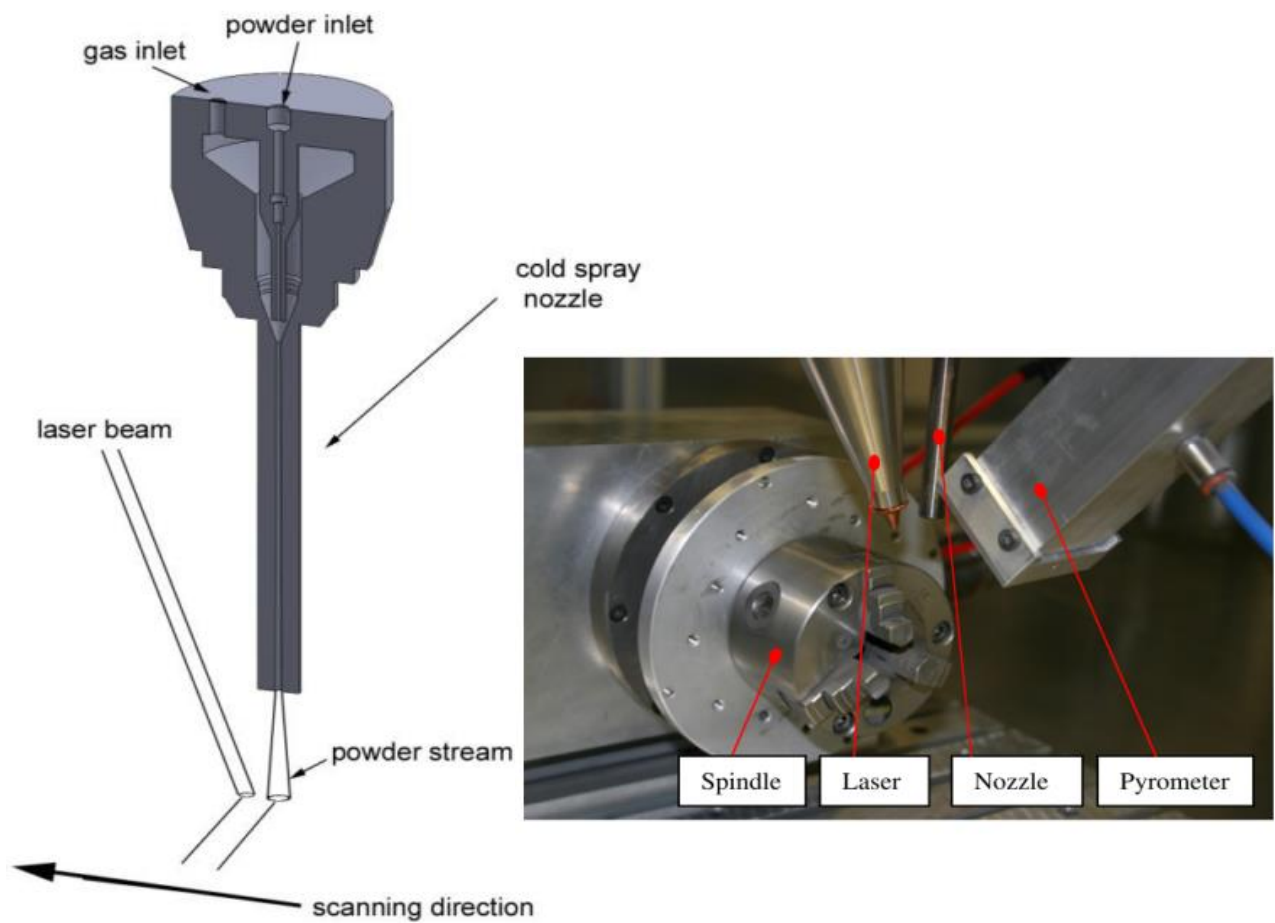
**Figure 7.1: (a) Experimental set-up, (b) side view of experimental set-up, (c) movement geometry of coupled cold-spray gun-laser head and (d) top view of the pattern of both cold-sprayed particles and laser spot [101]**

Several strategies like the one shown above can be applied with respect to positioning the laser beam with respect to the deposition footprint. It can be external (leading, trailing or concentric) or axial internal through the system as in laser cladding. While external laser integration constitutes simple alignment of various components, there is considerable rework as the alignment only holds well for preset standoff distances. Secondly it limits deposition rate per

pass to account for shadowing effect of the deposited layer as presented in figure. Finally, the deposition route has to be specific path to ensure identical laser beam –substrate interaction.

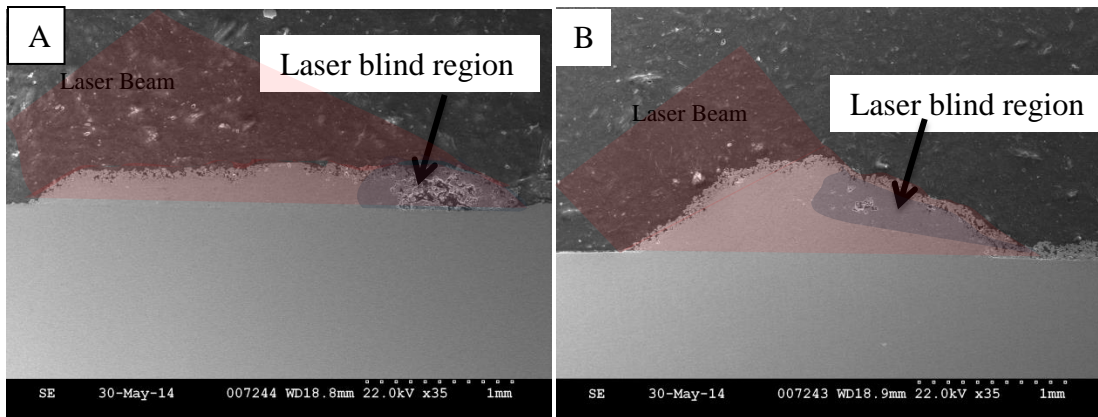
Yet another externally oriented strategy is available in literature from a research group in Cambridge, UK [20, 21].

Figure 7.2 depicts a schematic of their process. In this system a 1KW diode laser is installed such that it softens every layer of the deposit. This improves the deposition efficiency as it creates better conditions for particle adhesion in the subsequent layer.



**Figure 7.2: External laser assisted cold spray process [108]**

In the present study a novel coaxial laser assisted cold spray process is developed. Unlike existing externally aligned laser – cold spray systems, the shadowing effect of the beam attenuation is circumvented with the current technology (Figure 7.3)



**Figure 7.3: Limitation of external laser assisted cold spray process: Beam path obstruction**

The internal strategy of the present innovation results in a compact system, where the laser and cold spray nozzle can be mounted together in a unified housing. Further the laser beam is always irradiating the surface and there is no shadowing. The laser beam, transmitted through the inner passage of a cold spray nozzle enhances deposition that is challenging with conventional process. Through a sequence of optical lenses, the beam is converges at the throat of the nozzle later expanding to follow the inner profile of the nozzle (Figure 7.4). This arrangement results in unobstructed irradiation of the deposited foot print. The axial integration of the two systems permits a homogenous increase in target temperature. At an optimum laser power for a given precursor feed and nozzle traverse rate, a multifold improvement in bond strength is observed. In addition to heating the target, the laser beam is also scattered by the powder stream. The effect of the laser beam on the powder stream characteristics will be studied through individual swipe tests. FIB cross section of the particles will be performed to understand the effect of axial laser beam on the deposition. The objective of this study is as follows:

- Determine the contribution of laser power at non-optimal cold spray conditions
- Benchmark contribution of laser with homogenous powders through annealing pretreatment
- Micro-dissect individual ‘splats’ to distinguish features of laser irradiated deposition

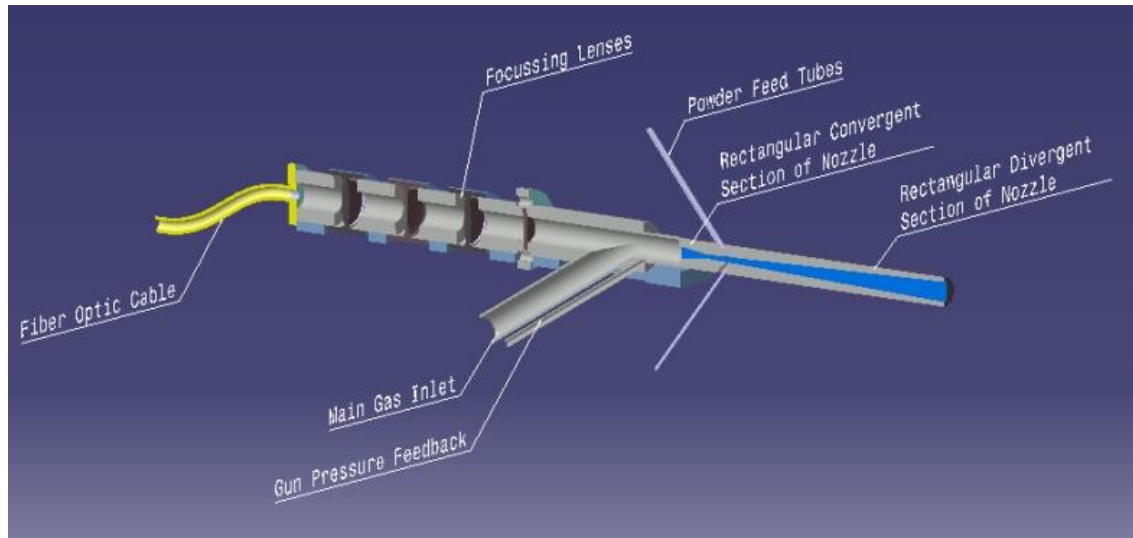


**Figure 7.4 The U of M Coaxial laser assisted cold spray nozzle [109]**

## **7.2 Experimental**

### **7.2.1 Deposition hardware**

The Fe-Mn<sub>2</sub> and Fe-Mn<sub>3</sub> feedstock presented previously (Chapter 4, 5) are chosen in this study. The powder was then either used in as-received and in sieved condition using a 500-mesh sieves and sprayed onto polished Al-6061 substrates. The cold sprayed system used in this study was developed at the University of Michigan. The system utilizes a rectangular diverging nozzle section with expansion ratio of 10 and a diverging length of 275mm. A downstream peripheral powder injection scheme is utilized. A conventional thermal spray powder (150psi) Thermach AT300 powder feeder is used due to lower operating pressures. A laser beam is directed axially through the nozzle to irradiate both inflight particles and substrate. A Trumpf 1KW disk laser with a wavelength of 1030nm is used as the laser source for the process. The laser beam was shaped to fill the inner chamber for the cold spray nozzle and axial emanate from the nozzle exit (Figure 7.5)

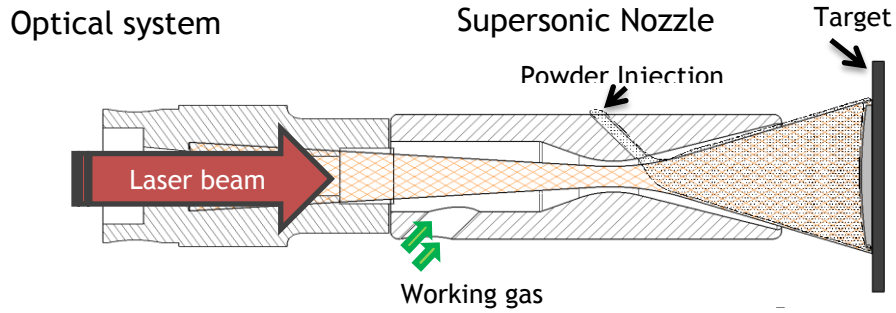


**Figure 7.5: Schematic of Coaxial laser assisted cold spray process used in this study**

Feedback: A CSL high speed pyrometer was used to detect real time temperature measurements. The pyrometer reads a wavelength of 2.5 to 5um which is away from the 1.03um wavelength of the laser. The default emissivity value supplied with the sensor was used. Data from the pyrometer was logged with nation instruments lab view software using usb-daq acquisition hardware.

### 7.2.2 Experimental matrix

The reader is referred to chapter 6 for more details on the experimental section. The deposition parameters including laser power are presented in Table 7.1. Deposition was carried out at three different precursor feed rates:- 1rpm, 2rpm and 6rpm.

**Table 7.1: Deposition parameters used in this study**

Feed rate (rpm)	Laser Power (watt)		
1	0	50	150
2	0	50	150

**Table 7.2: Composition of Fe-Mn alloys used in this study**

%wt	Mn	Al	Cr	C
Fe-Mn2	35	4	2	0.2
Fe-Mn3	25	2	2	0.1



### 7.2.3 Microstructure characterization

Initial characterization of as sprayed cladding was done with scanning electron microscopy (SEM/BSE) on a Hitachi S-2600N SEM to determine the quality in terms of homogeneity, porosity and cracks. Samples used for SEM studies were prepared following standard metallographic procedures. Composition of the coatings was determined with energy dispersive X - ray analysis (EDX) in SEM and back scattered electron imaging was done to obtain composition contrast. For the phase analysis and crystal structure determination, X – ray diffraction (Rigaku MiniFlex, Cu K $\alpha$  radiation with  $\lambda = 1.5402 \text{ \AA}$ ) study and differential scanning calorimetry (TA Instruments Q600 model) studies were conducted. Auger spectroscopic analyses were conducted with a Physical Electronics Scanning Auger Nanoprobe 680 equipped with a field emission source, Everhart-Thornley secondary electron detector, cylindrical mirror analyzer, and an eight-channel detector. Sputtering depth profile experiments were performed with a PHI model 06-350E Ar+ source biased at 1 keV. The experimentally determined Si sputtering rate on this instrumental geometry was  $14 \pm 3 \text{ nm min}^{-1}$ . To assess the basic mechanical properties of the coatings, Vicker's hardness tests were done on a Future Tech FM1-E hardness tester with a 300gm load for a dwell time of 10 seconds.

Splat analysis: FIB Nanolab helios 650 was used to make crosssection. In FIB (focused ion beam) applications, ion beam (Ga+) assisted Pt deposition is commonly used as a protection layer for subsequent milling for cross-section or TEM sample preparation. To ensure no damage to the particles during Pt deposition, the electron beam was used prior to ion beam to deposit the Pt layer.

### 7.2.4 Laser Power measurement:

The actual laser fluence was measured using a Coherent FieldMax power/energy meter (Coherent, Portland, OR). Figure 7.6 shows the schematic to quantify attenuation that could occur from beam clipping within the nozzle and scattering due to the powders.

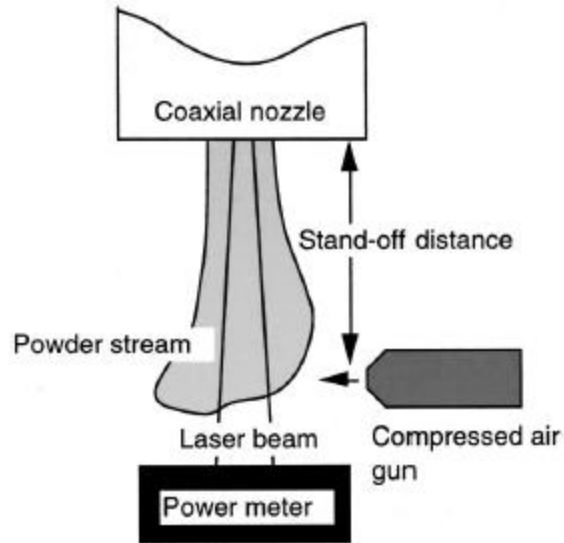


Figure 7.6: Laser power attenuation measurement due to powder stream [110]

#### 7.2.5 Shear Punch Test:

SPT is a small scale specimen testing procedure in which thin disc samples are punched through a die hole while driving the punch at a constant speed. During the process, load on the punch and punch displacement are measured simultaneously. More details on the SPT procedure can be found in the literature [13-16]. The advantage of SPT lies in the amount of material required for testing. Being a small scale specimen testing procedure it requires only few hundreds of microns thick disc samples. A newly built SPT setup in our laboratory was employed for the current experiments. The diameters of the punch and die employed were 1.51 and 1.54 mm, respectively. Testing was conducted on the coatings that were peeled off from the substrate. Prior to the testing, coatings were thinned down to 200 – 450 microns thickness range with metallographic grinding procedures. The specimen thickness range was chosen based on the die-punch clearance employed as well as the earlier studies conducted by Guduru et al. [13]. An Instron 4469 was used to conduct the experiments. The load was measured by the load cell whereas the punch displacement was recorded from the Instron crosshead displacement. The punch was driven at a constant speed of 4.12 mm/s throughout the test.

#### 7.2.6 Wear characteristics:

The tribological behavior of the claddings was studied at temperatures at room temperature (RT, ~25 °C) using a CSM ball-on-disc tribometer. Prior to testing, samples were polished with 1200

grit SiC polishing paper to avoid excessive tangential loads during testing. Dry sliding tests were conducted in ambient air under a load of 6 N and a sliding speed of 3.25cm/s for a total of 12,000 cycles. A tungsten carbide 6.25mm ball (McMaster Carr) was used as a static friction partner.

#### 7.2.7 Electrochemical Corrosion test

The corrosion behaviors of the as-received and annealed claddings were evaluated by using an AMETEK Princeton Applied Research (PAR) Flat Cell model K103. The surface of the corrosion specimens was slightly ground on 1200-grit emery paper, cleaned with acetone in a ultrasonicator and alcohol prior to corrosion testing. Anodic polarization tests were carried out in a 0.5-wt. % NaCl solution which was prepared using analytical grade reagents. The initial pH value of the solution was 5.7 and the initial temperature of the solution was at 20°C. The specimen was driven from an Ecorr of -1 to 2V (vs ref) at a scanning rate of 1.66 mV/s to produce Potentiodynamic polarization plots. All potentials were measured with reference to a standard saturated calomel electrode (SCE).

#### 7.2.8 Bond strength measurements

Standard ASTM C633 adhesion strength tests consist of gluing the cold sprayed samples to grit 24 alumina blasted mild steel cylinders with FM1000 epoxy glue (Cytec Industries, Woodland Park, NJ) followed by a destructive tensile test which measures the coating-substrate adhesion strength. Prior to gluing the cold sprayed samples to the mild steel cylinders, the epoxy glue was first heat treated in an air furnace at 90 °C for 3 h. In order to ensure proper adhesion between the glue and the metallic surfaces, the samples were heat treated in an air furnace at 200 °C for 3 h and then air cooled at room temperature. All ASTM C633 adhesion strength tests were performed using an Instron 4469 universal testing machine (Burlington, Ontario, Canada) with a 50 kN dynamic load and a constant speed of 2.54mm/min

### **7.3 Results and discussion:**

Given the coaxial nature of deposition, scattering of the laser power due to the powder stream was studied using power meter similar to the method used to study attenuation of laser beam in a cladding process. The result of different precursor loading rates on laser power available at deposition foot print is shown in Figure 7.7. Higher rpm is representative of increasing feeding rates with 1.5rpm equivalent to 7g/min and 6rpm to that of 30g/min. As is evident, the beam attenuation at feed rates used in the present study is negligible and is hence not accounted.

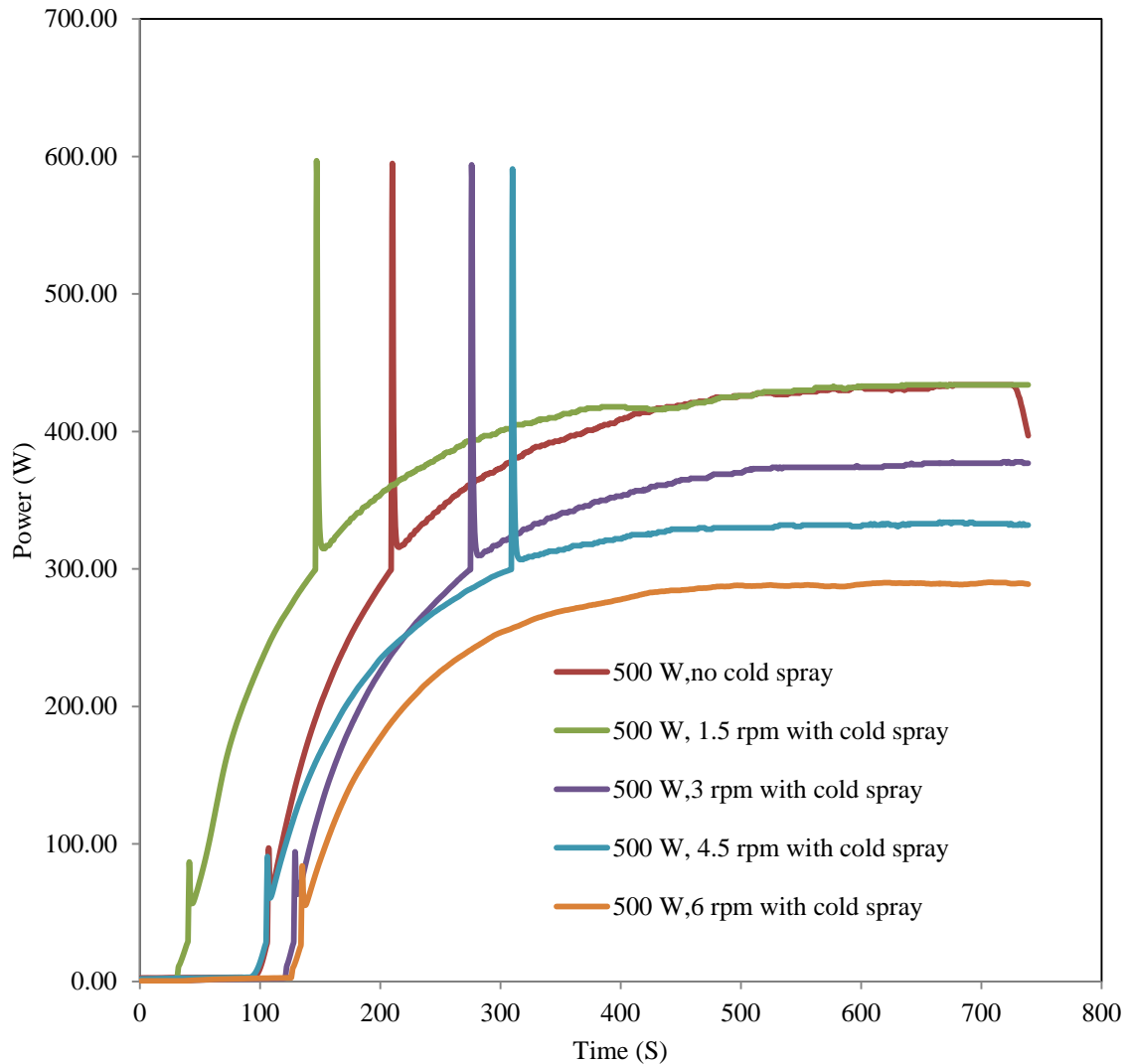


**Figure 7.7: Beam attenuation at various powder loading/feeding rates**

### 7.3.1 Surface temperature profile:

Surface temperature recorded using an IR pyrometer is presented in Figure 7.8. The pyrometer travels with the nozzle and data is plotted for a total of 5 reciprocating passes. Without the laser irradiation, surface temperature reaches a maximum of 250°C. The addition of laser in steps of 50W increases the surface temperature to 320°C. Beyond 200W the substrate starts warping and eventual starts to melt at >300W.

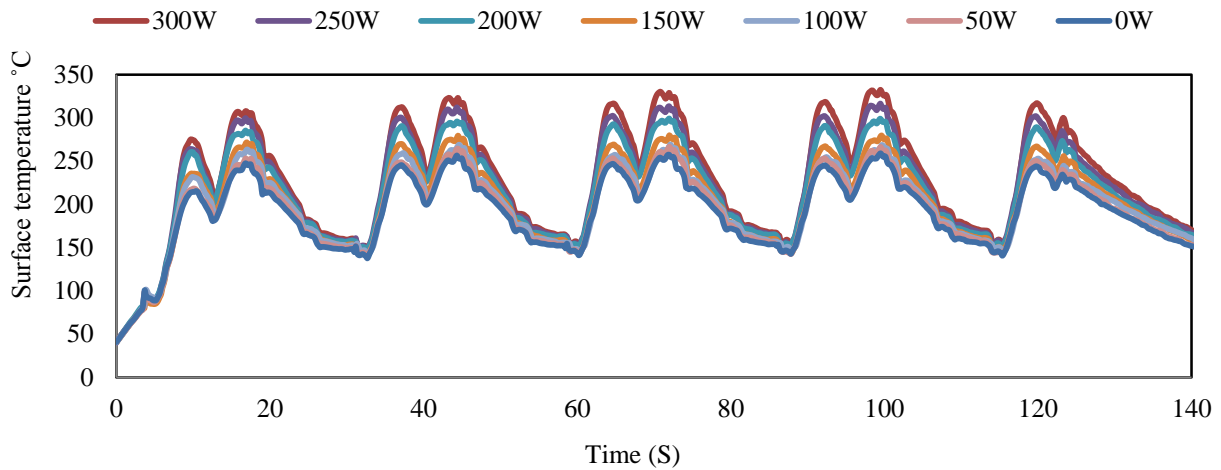
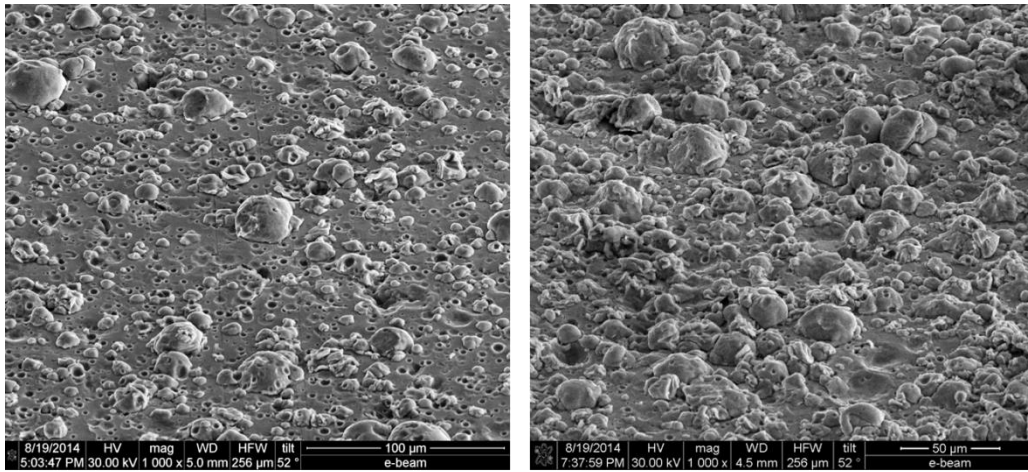


**Figure 7.8: Surface temperature profile during deposition at different laser powers 0 to 300W in 50W increments**

### 7.3.2 Swipe tests

In a swipe test, the deposition nozzle is ‘swiped’ over the target at said standoff distances at a large scan velocity (typically 200mm/s). This creates scarcely deposited layer necessary to distinguish and analyze individual splats. The results of the swipe test are presented in Figure 7.9. SEM images taken a 52° tilt present a cross-section of a particle after impact. Swipe testing was conducted on previous coated and polished Fe-Mn coatings at 0 and 500W of laser power. This was done for the following reasons: First, during deposition onto aluminum, the powder penetrates the surface without significant deformation [25]. Secondly the higher thermal conductivity of the aluminum results in the need for higher laser powers to achieve necessary increase in surface temperature[64], [111]. The Swipe test shows densely populated depositions sites when assisted with laser beam. The Swipe test, SEM examination was followed by a cross-section of the deposited particles for further analysis. Dissection was performed with a focused ion beam to reveal the internal microstructure of deposited powder (Figure 7.10). A 1 micron layer of platinum was deposited prior to ion milling to protect the features of the deposited powder.



0W deposit

500W deposit

**Figure 7.9: SEM images at 52° of ‘Swipe’ tested samples using a coaxial laser beam**

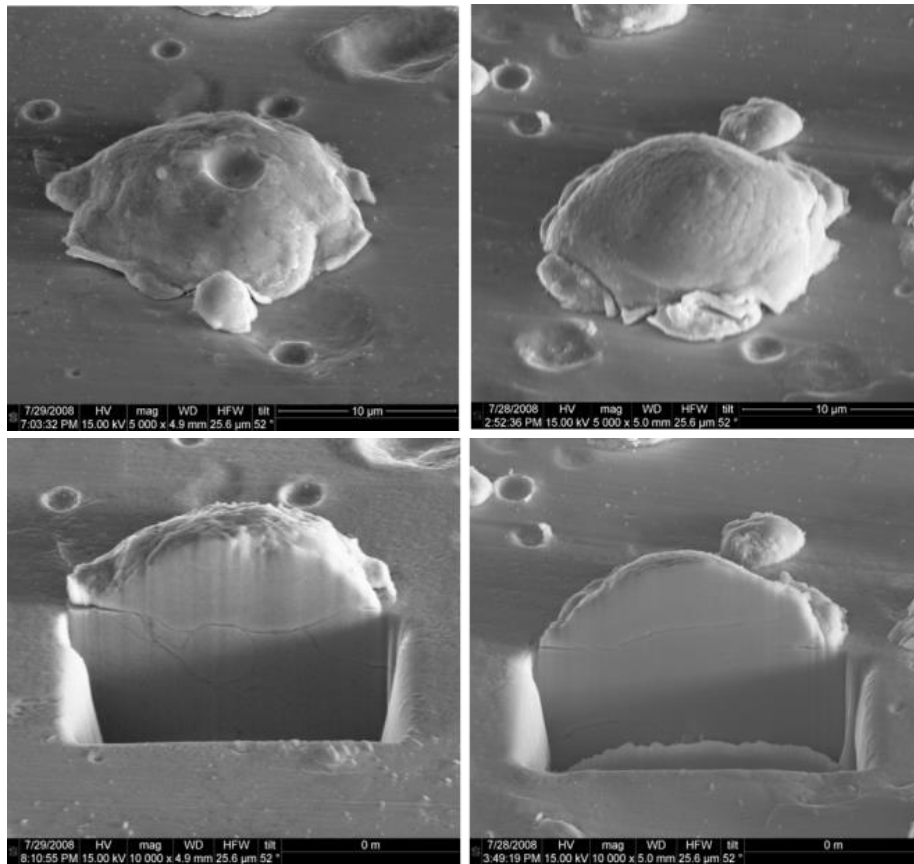


**Figure 7.10: FIB crosssection examination of deposited particles at 0 and 500W laser power with coaxial laser beam**

### 7.3.3 Auger Electron Spectroscopy (AES)

AES was performed to understand the effect of the process on lighter elemental species, that cannot be detected through conventional EDS technique. The samples were sputtered to remove surficial contaminants and to get a depth profile. Nitrogen and Oxygen levels are of interest owing to chances of nitridation and/or oxidation due to presence of nitrogen jet and higher surface temperatures with the laser. The results of the AES scan of swipe tested particles are presented in Figure 7.11. The SEM picture shows the point scan performed on deposited particle as well as previously deposited and polished coating. The intensity profile indicates that the laser assisted samples show lesser oxygen content. This is similar to result obtained after annealing the powders (as shown in chapter 5)

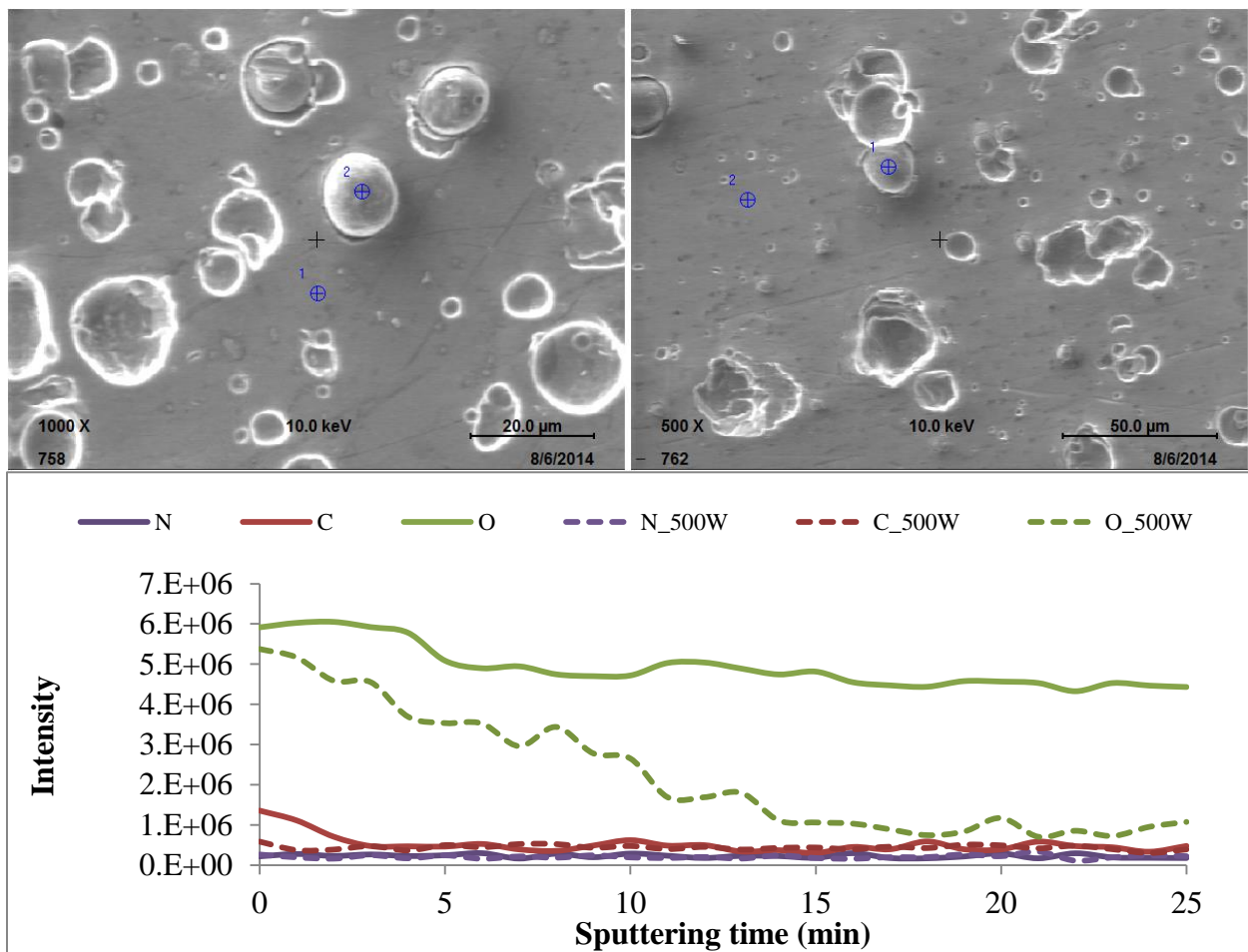
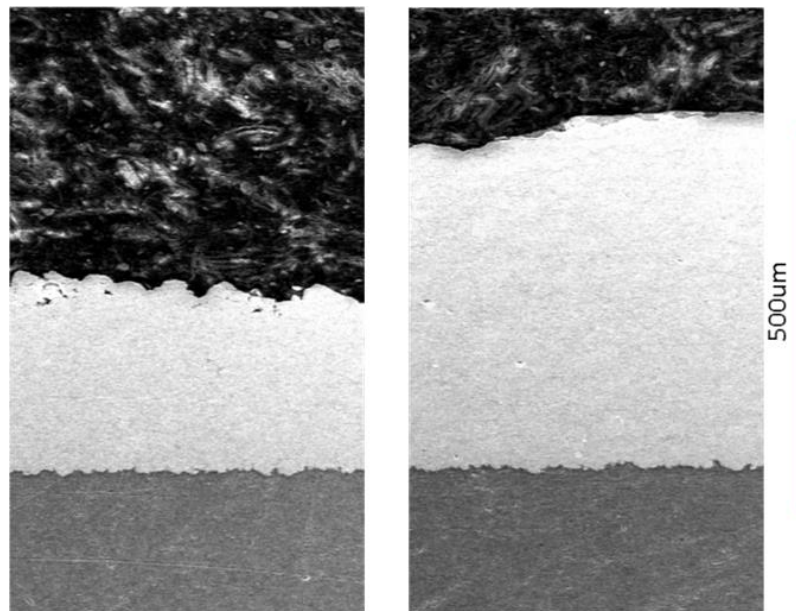


Figure 7.11: AES spectra of the swipe tested Fe-Mn<sub>2</sub> samples at 0 and 500W laser power

### 7.3.4 Coating microstructure analysis

The complete deposition cross-section of the coatings with and without laser assist are presented in optimum cold spray conditions Figure 7.12 and at higher particle loading- Figure 7.13. The particle loading adversely affects its velocity. For the present Fe-Mn<sub>2</sub> alloy system, the addition of laser at 150W results in increase in deposition thickness as shown. Beyond this power, the effect of laser was detrimental and resulting in fracture within the coating. The beneficial effect of the laser is also seen in non-optimum deposition in Figure 7.13. Here while there is negligible increase deposit thickness, coating benefits from significant increase in deposition quality. The laser helps in substantial reduction from fracture that could result from lower particle velocities. At higher particle loading (2rpm) the particle velocity is reduced. Particles with lower velocity in addition to the inability to deposit can counteract by acting as erosive media. At higher laser powers (>150W) the surface temperature is fairly high (>300°C). Hence the erosive action is now aggravated resulting in a detrimental effect. The corresponding phase evolution of cold sprayed Fe-Mn<sub>2</sub> Coatings with laser assistance is shown in Figure 7.14. The presence of laser subdued the evolution of secondary phases in the coatings. There was no peak broadening signifying minimum effect on grain size in the coatings.



**Figure 7.12: Effect of laser power on deposition efficiency of Fe-Mn<sub>2</sub> coatings at optimum cold spray conditions**



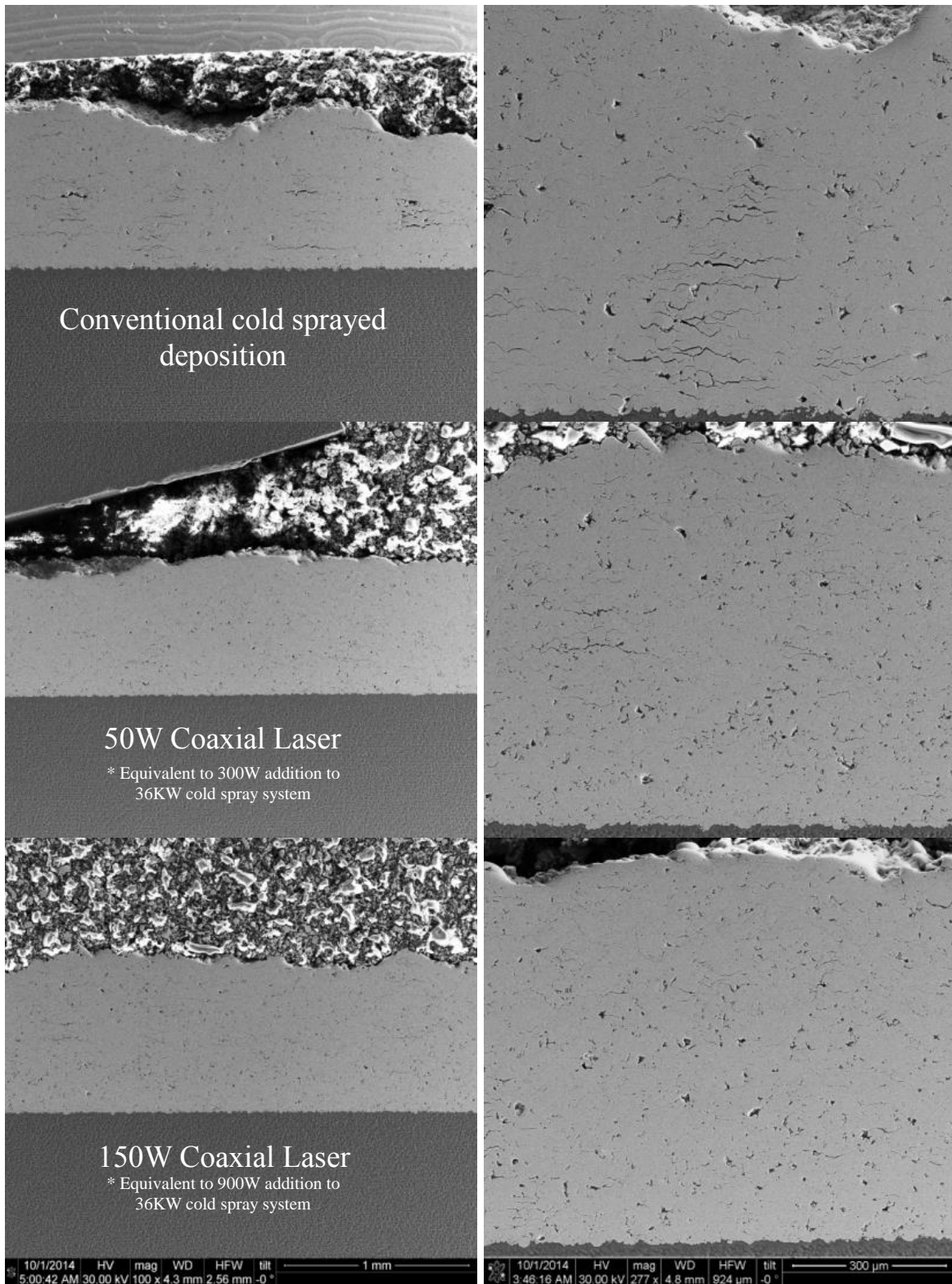


**Figure 7.13: Effect of laser power on deposition efficiency of Fe-Mn<sub>2</sub> Alloy at non optimum cold spray deposition condition (higher particle loading)**

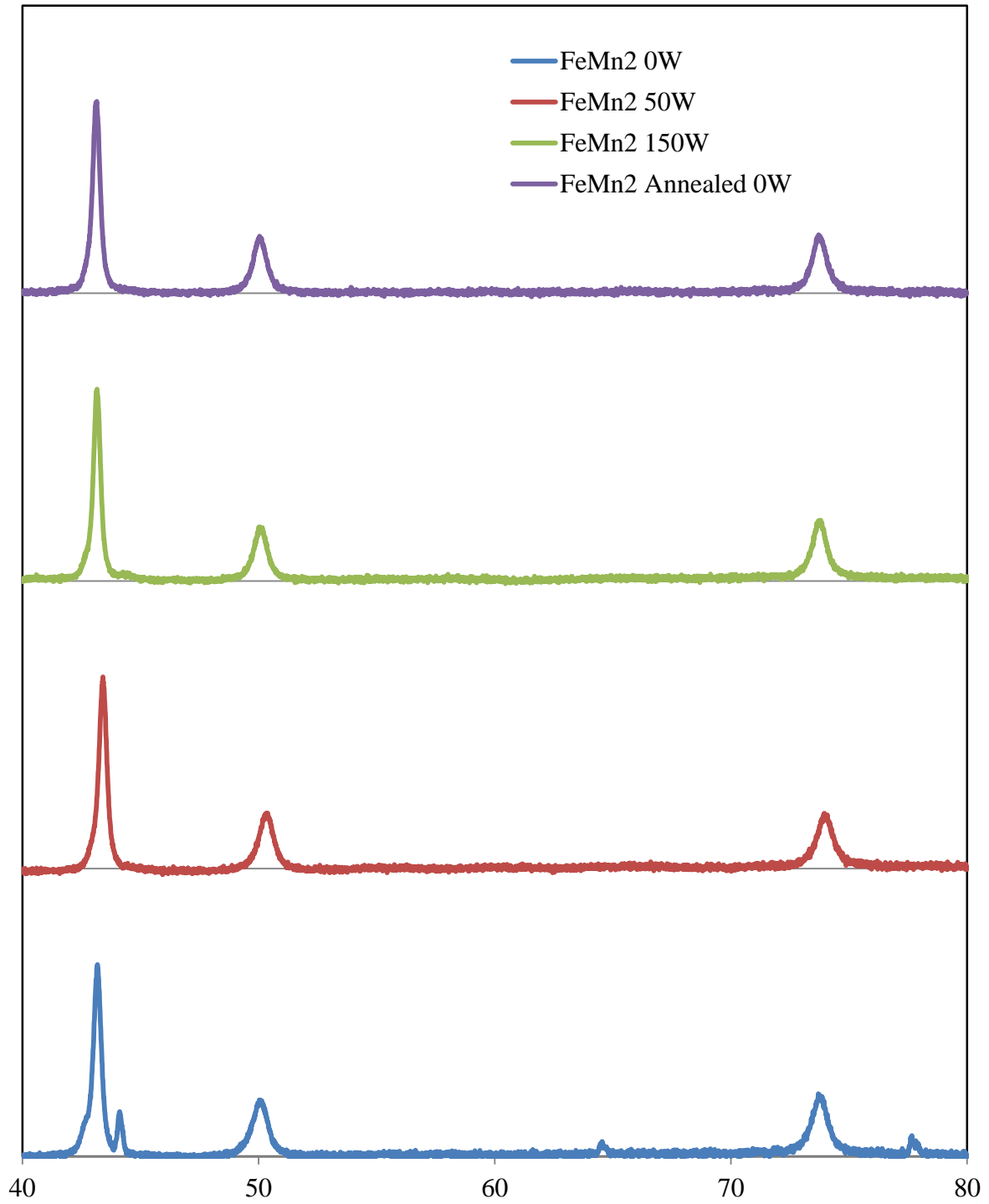


Figure 7.14: XRD peaks of Fe-Mn<sub>2</sub> deposited coatings at increasing levels of axial laser irradiation

### 7.3.5 Electrochemical Study – Open circuit potential:

The OCP data for Fe-Mn<sub>2</sub> alloys deposited without laser, with annealed powder and with 150W laser is shown in Figure 7.15. There was no difference observed in the OCP values between coating with and without laser treatment. This result is consistent with the one of previous OCP tests and the absence of passivation behavior of the alloys has been predicted by prior literature [22].

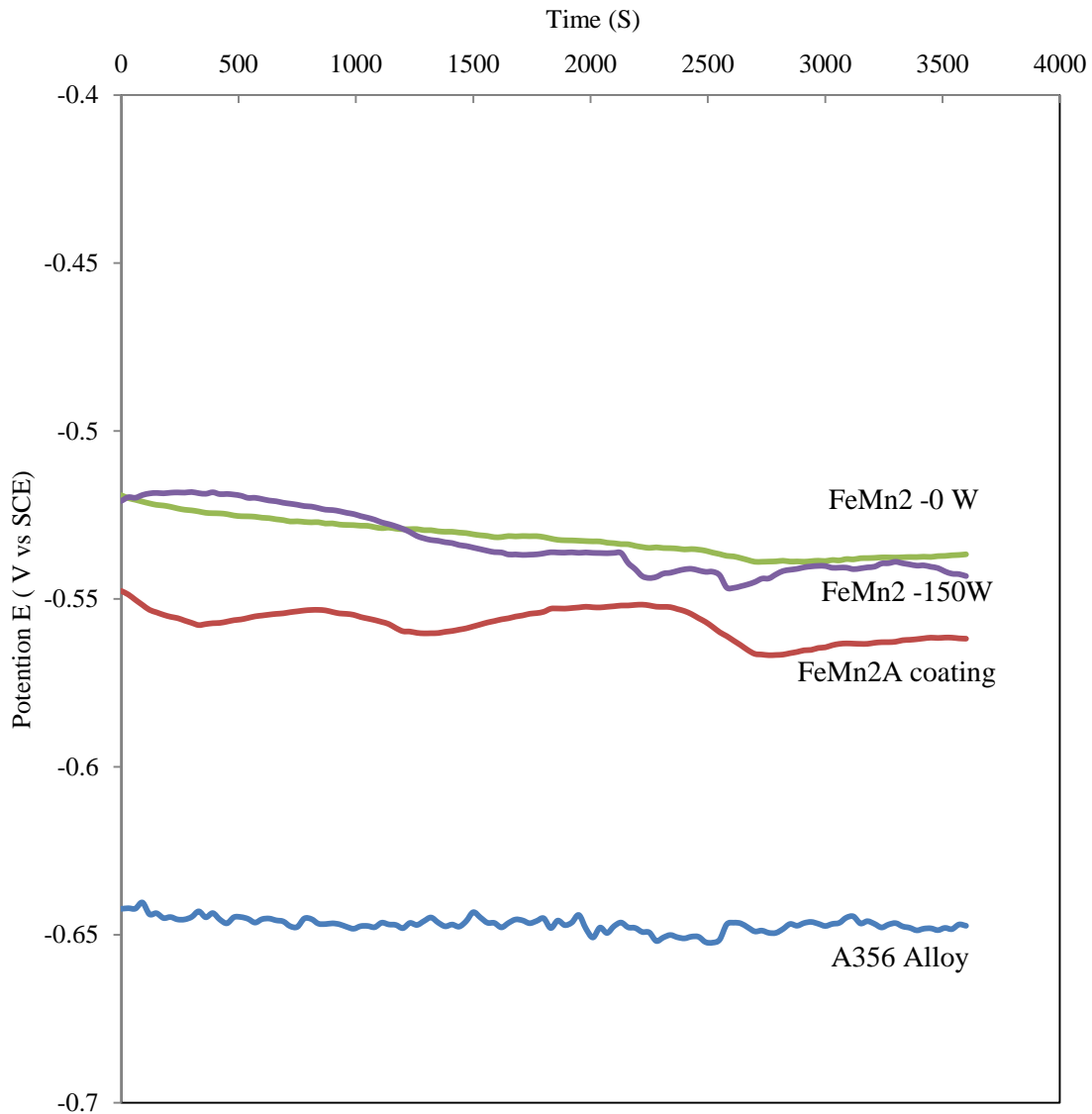


Figure 7.15: Open circuit potential of Fe-Mn<sub>2</sub> coatings at increasing levels of axial laser irradiation

### 7.3.6 Wear testing:

The Coefficient of friction (COF) of cold sprayed Fe-Mn<sub>2</sub> coatings deposited at 0, 50 and 150W of laser power is presented in Figure 7.16. All three coatings exhibited identical behavior and took about 3000 cycles to exhibit stable friction profile. The amplitude of uneven COF increased with increasing laser power. Based on history of wear testing conducted in this study, the COF is not related to the phase of the coating but the deposition style. A similar effect was observed with SS316 coatings deposited with Nozzle8 in Chapter 4. Hence it is believed that the variation (COF) from steady behavior could be due to the result improved deposition. The absence of lubricating phase results in excessive COF of Fe-Mn<sub>2</sub> coatings.

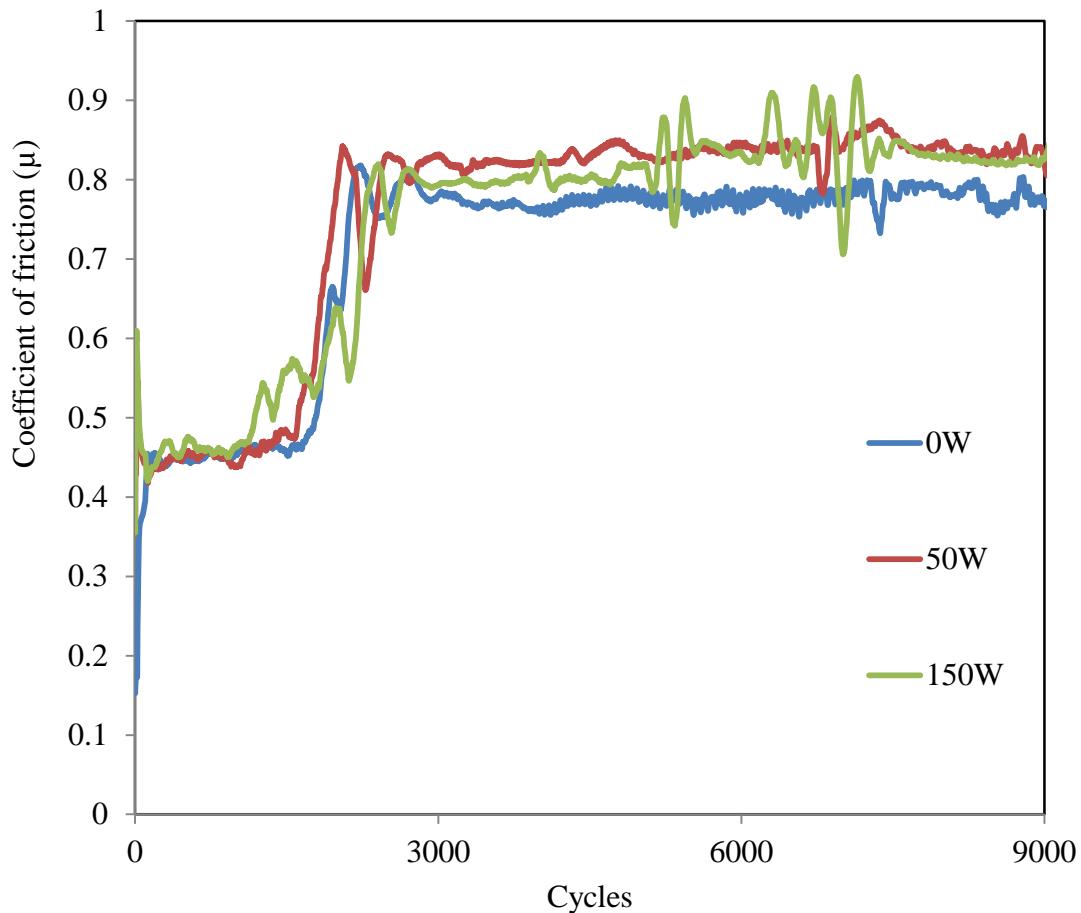
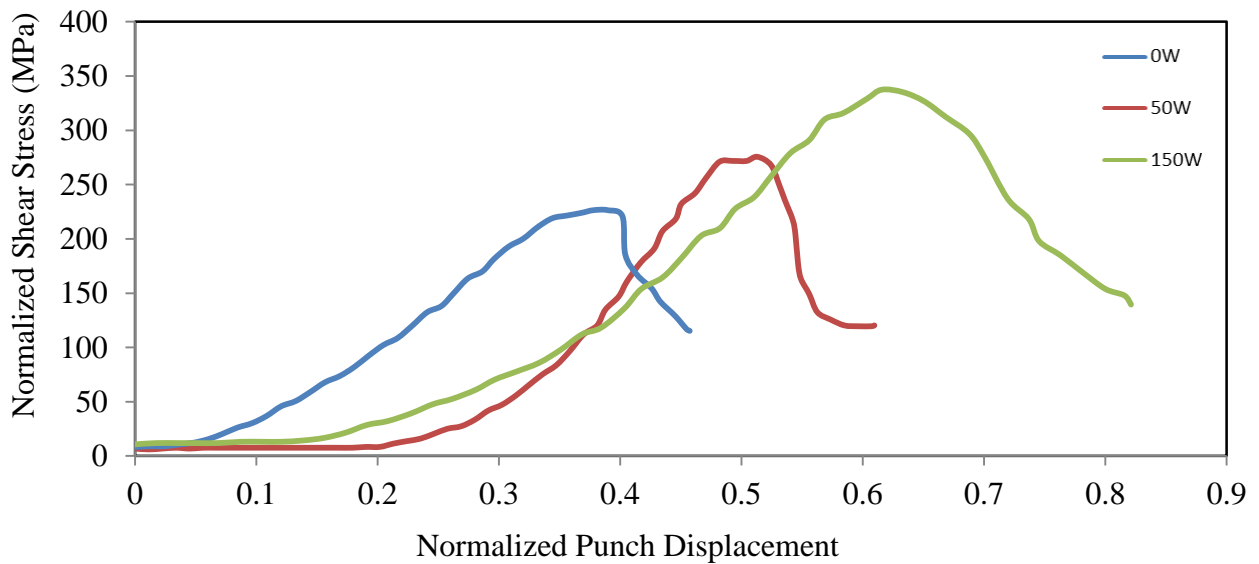


Figure 7.16: Coefficient of friction of Fe-Mn<sub>2</sub> coatings at increasing levels of axial laser irradiation

### 7.3.7 Shear punch test (SPT):

Figure 7.17 shows the SPT curves of coating deposited at 3 distinct conditions: 0, 50 and 150W. The x-axis is plotted in terms of normalized punch displacement, which is the ratio between the punch displacement and specimen thickness. This avoids the influence of specimen thickness on the overall punch displacement [112]. The y-axis indicates the shear strength of the material. As the shear punch test was performed on coatings stripped from the substrate, the strength stems from the cohesive bonding. The increase in this strength value with increasing laser power shows an increase in cohesive strength of the coating – showing that irradiation with laser beam helps in fusing the particles together.



**Figure 7.17: Normalized shear stress vs displacement of Fe-Mn<sub>2</sub> coatings with and without laser assistance**

### 7.3.8 Bond testing of cold sprayed coatings deposited with different laser powers:

The bond strength of cold sprayed Fe-Mn<sub>2</sub> coatings with 0, 50 and 150W laser power is presented in Figure 7.18. The increase in strength of the coatings with addition of laser is evident. Without laser assistance, a bond strength of 35Mpa is achieved which is typical of cold spray coatings [113]. At 50W laser power, the strength increases by about 7Mpa and a substantial increase are obtained at 150W by an excess of 23Mpa. The deviation in results is also tighter with increasing laser power. Bond test of samples deposited with more than 150W was not conducted due to presence of detrimental cracks in the coating as shown in Chapter 6.

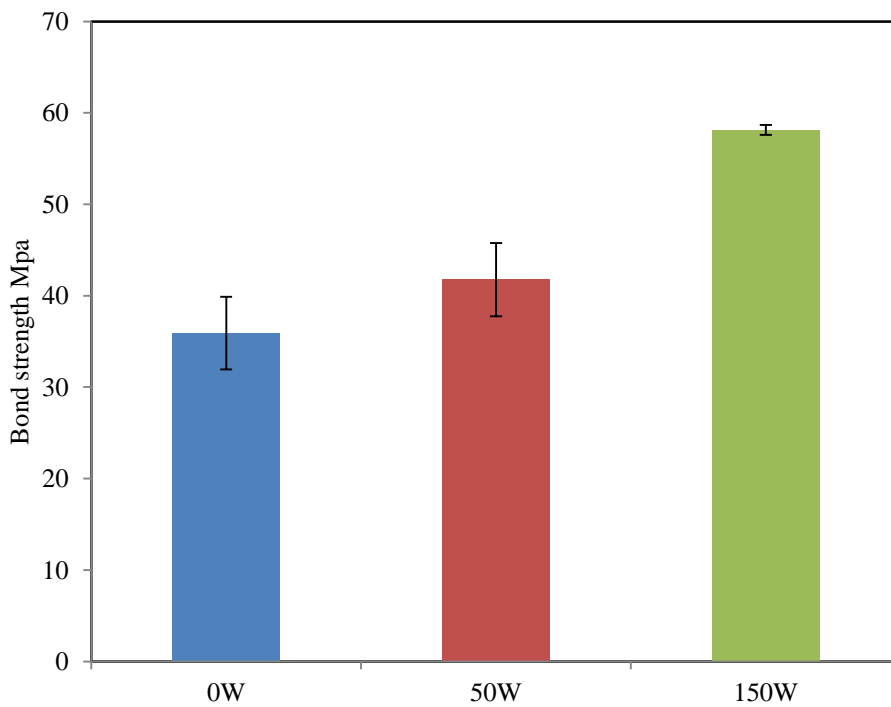


**Figure 7.18: Bond strength of Fe-Mn<sub>2</sub> coatings deposited at different laser powers and different powder loading rates**

## 7.4 Summary

Coaxial laser assisted cold sprayed of Fe-Mn alloy coatings are demonstrated. The coatings showed a negligible porosity and metallurgical bonding with the substrate interface. Auger profile revealed a reduction in oxygen levels in deposited coating with the laser process. With the laser assist, an increase in material jetting was observed. These agree well with other findings on the constructive influence of higher deposition temperatures. There is sweet spot for laser power; at excessively large laser intensity can lead distortion induced cracking and finally hot erosion of the deposited material. Wear and Corrosion testing lead to a minor improvement in coating performance. Significant enhancement was recorded in shear strength and bond strength levels. Both these experiments prove an increase in particle –particle fusing with an addition of .9KW of actual power consumption to the existing 36KW cold spray system. Unlike external laser assisted process presented in prior art, benefit of coaxial laser assisted deposition is realized at significantly lower laser power. Finally, a new scheme is proposed for to highlight the deposition mechanism of coaxial laser assisted cold spray process Figure 7.19.

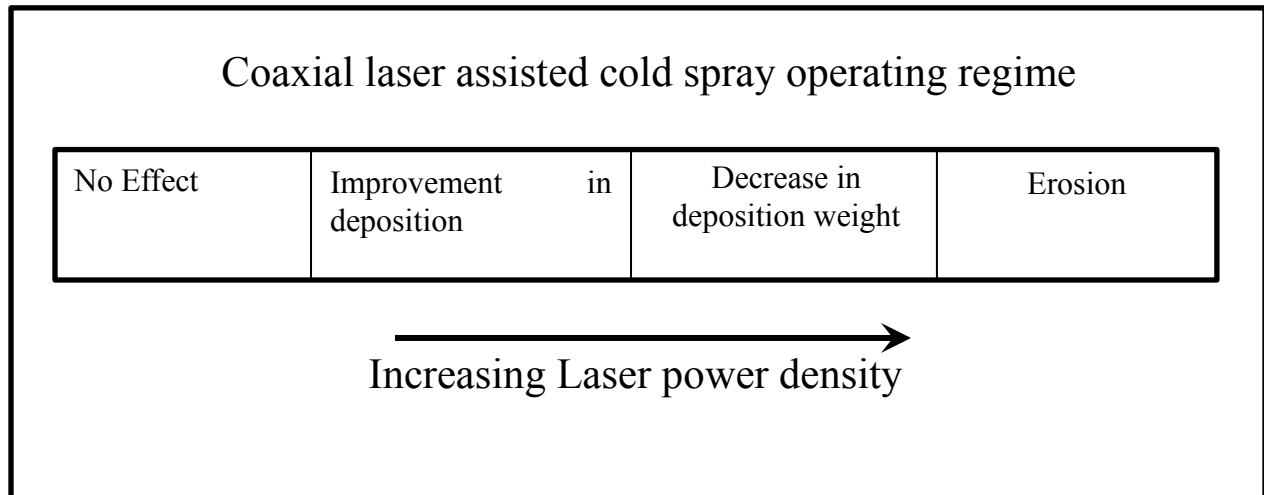


**Figure 7.19: Proposed schematic highlighting the effect of laser power density**

## **8. Application case study: Iron manganese alloy as wear resistant coated aluminum brake rotors**

### **8.1 Introduction**

The US Environmental Protection Agency (EPA) and the National Highway Traffic Safety Administration (NHTSA), with the cooperation of Major Automobile Manufacturers (MAM), adopted new regulations to dramatically increase fuel economy and decrease greenhouse gas emissions from cars and light trucks. Notably, the average fuel economy of new passenger vehicles must be at least 34.1 miles per gallon (mpg) for model year 2016 and up to 54.5 mpg for model year 2025, an increase over 2011 levels of approximately 15% and 90%, respectively [114]. In exploring fuel-economy boosting technologies, MAM are increasingly focused on the ‘light weighting’ of vehicles. Vehicle light weighting is a particularly effective solution because it affects every form of road transport, all types of propulsion, and offers genuine concrete economic advantages [115].

Mass is a crucial parameter in reducing energy demand by acting directly on the level of useful energy required to overcome the inertia and countervailing forces that prevent movement. The maximum operating mass of a vehicle is indicated by its gross vehicle weight rating (GVWR) which is comprised of curb weight (vehicle only) and payload weight (cargo/passengers). As GVWR increases with vehicle size, curb weight as a proportion to GVWR decreases. Conversely, vehicle weight accounts for a larger portion of energy demand in lighter vehicles than in heavier vehicles. Thus, Passenger vehicles (PV) and light commercial vehicles (LCV), up to truck class 6 (GVWR up to 26,000 lb) are particularly attractive targets for light weighting.

Various studies place the fuel savings associated with a 10% reduction in vehicle weight between 6% and 8% (Figure 8.1) In addition, weight reduction in one part of the vehicle creates light weighting opportunities elsewhere. For instance, the power of the engine may be reduced while



achieving the same performance due to the energy demand economy linked to weight reduction [21]

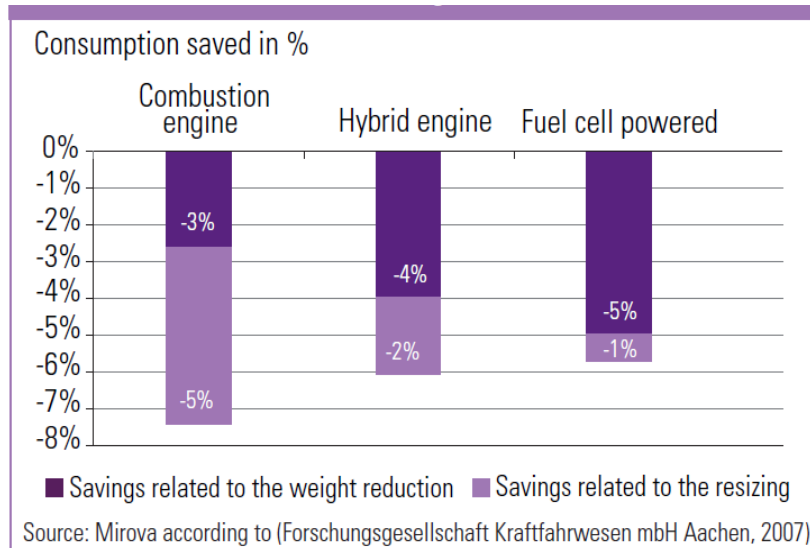


**Figure 8.1: Fuel savings based on 10% reduction of initial weight [21]**

In this regard, automotive brake rotors present a potential opportunity for weight reduction. Since their initial development they have undergone limited evolution and remain a heavy unsprung mass in today's vehicle. Several strategies have been adopted to develop Aluminum based brake rotors which will result in weight savings of 20 to 50% per rotor. These include:

**Al-MMC:**In the Aluminum Metal Matrix Composite (MMC) material, hard ceramic particles are reinforced into the Al matrix to enhance the thermal and wear resistance of the brake rotor. Despite significant effort, the brake surface temperatures are limited to approximately 450°C. The lack of solid lubricant like graphite in mmc's rotors results in lower braking efficiency, adhesive wear and galling. The cost is approximately 2 to 3 times the cost of gray cast iron rotors.

**Al-L12 alloys:**These include technological advancements in advanced high temperature grade Aluminum alloys like Al-Li and Al-Zr-Ti alloys. These contain L12 precipitates that improve high temperature development. These alloys are expensive and cannot be cast using traditional routes.

Carbon Fiber MMC: This technology is found extensively in aircrafts and high end sport cars. In addition to being expensive, these carbon fiber rotors are susceptible to fading and are not compatible with conventional Anti-lock brake systems.

Split rotor – two piece design: This product is available in the market at \$500/rotor. An aluminum core is fastened to cast iron/steel alloy rotor. There are no studies that indicate corrosion performance and thermal fatigue given the non-uniform heat flux distribution across the fasteners.

Steel Clad Rotor technology: This is developed by researchers at Michigan tech. A steel insert is placed on aluminum rotor. The manufacturer website has sufficient statistical data revealing the fuel efficiency and emission benefits. They have slots to compensate for CTE. There is no data on corrosion performance, from preliminary analysis -steel aluminum is a strong galvanic couple. This will result in reduction of product life. There is no information on reuse and recycling of these rotors.

Current Application: Use of Fe-Mn alloy as wear resistant protective layer on Aluminum alloy castings In order to assess the performance of Fe-Mn material system in current application, coatings were deposited on aluminum pucks and tested in a scaled brake dynamometer arrangement similar to the arrangement shown in Figure 8.2.

## **8.2 Experimental**

Fe-Mn<sub>2</sub> alloy was used for this evaluation. The material composition and deposition parameters developed previously are used as described in Chapter 5.

### **8.2.1 Scaled dynamometer testing:**

A reduced scaled dynamometer based on constant energy density scaling was used to simulate Fe-Mn<sub>2</sub> Coated pucks. The peak temperature during braking application on the scaled puck is shown in Figure 8.3. The testing performed included several stop sequences in accordance with FMVSS 105 directive. The sequences are as follows: Green effectiveness, Burnish stops, Characteristic checkpoints, Pressure sensitive stops and subsequent recovery periods. A total of 360 stops were performed after which the coating was analyzed. Corresponding coated puck before and after testing is shown in Figure 8.4.

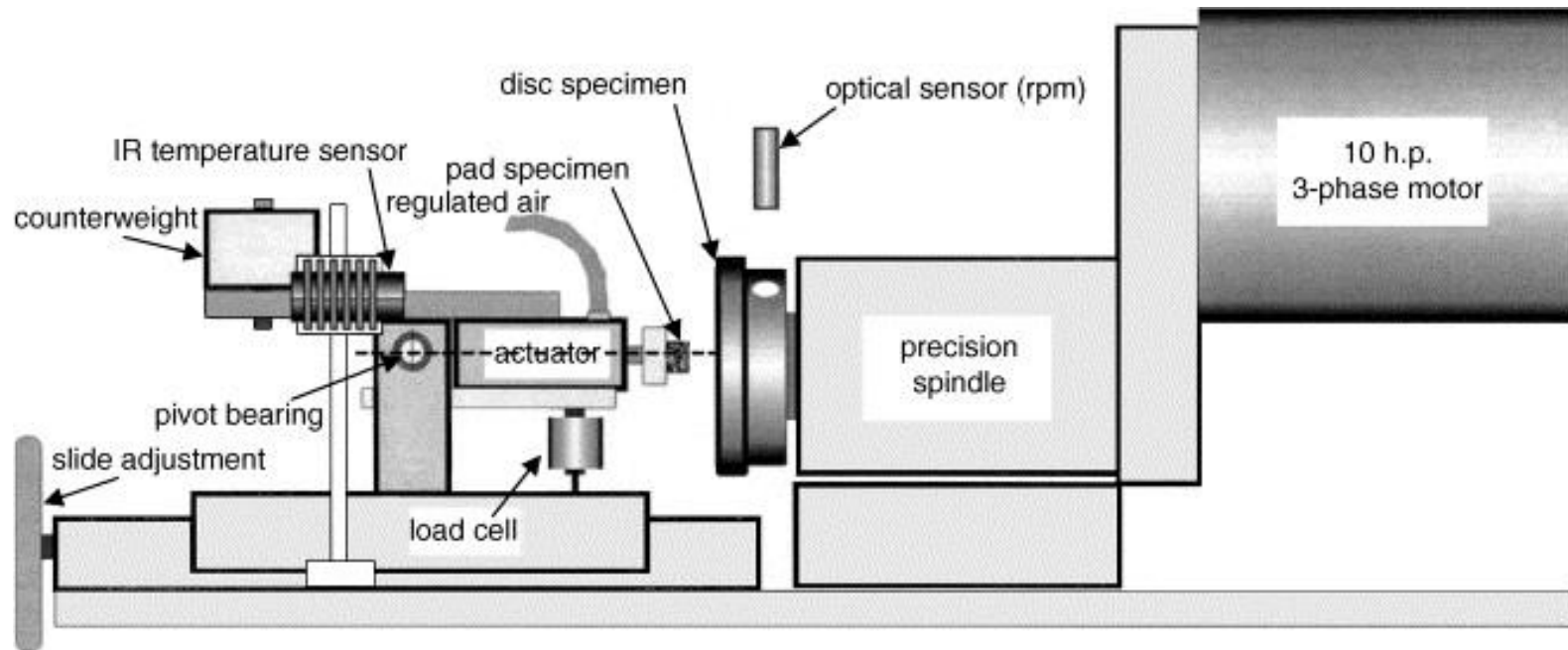


Figure 8.2: A schematic of the brake tester arrangement used for testing in the current study [124]

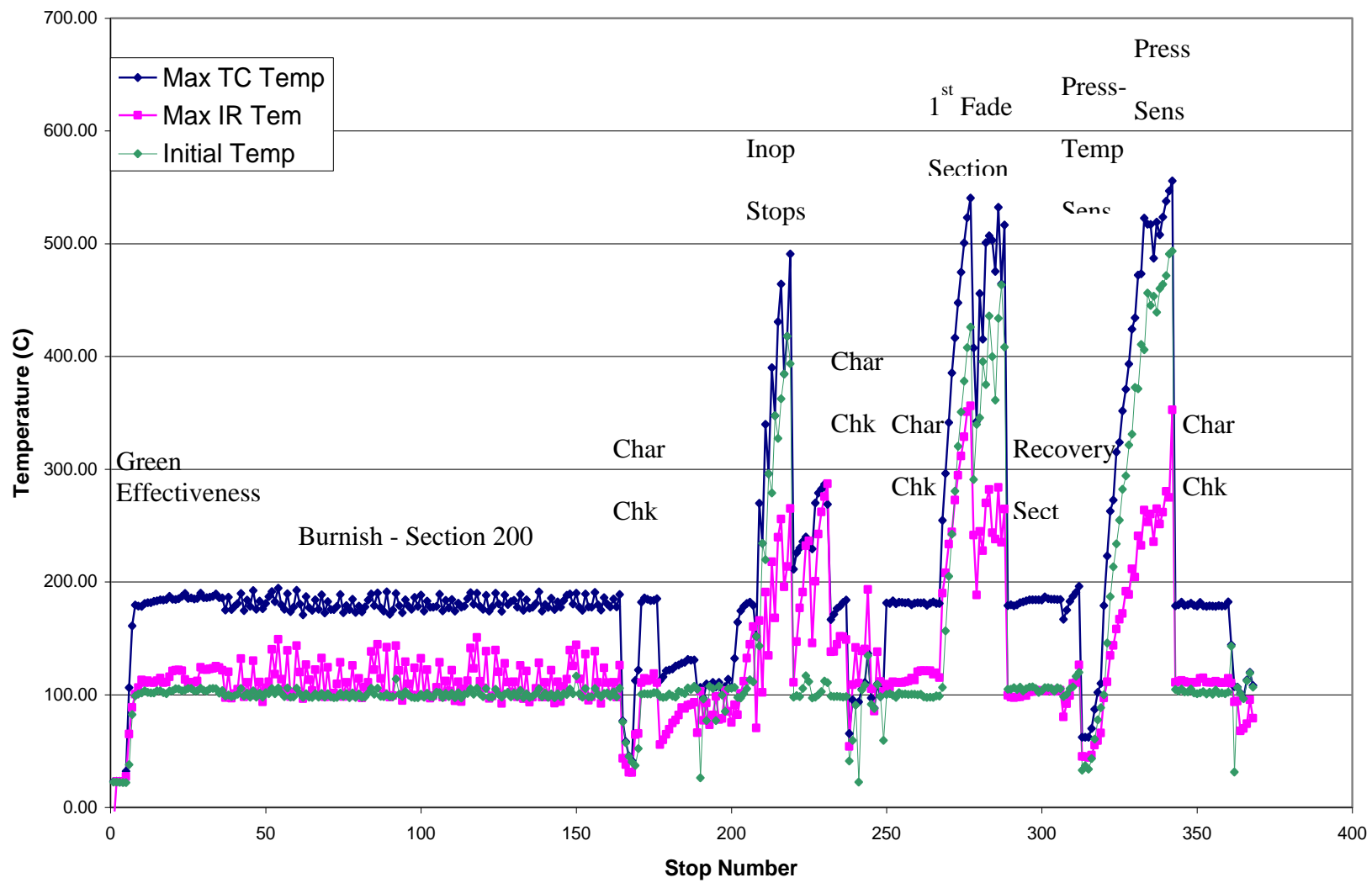


Figure 8.3: Maximum temperature vs Cumulative stop



**Figure 8.4: Aluminum pucks with cold sprayed Fe-Mn<sub>2</sub> coatings before and after testing**

### **8.3 Results and Discussion**

#### **8.3.1 Coating characterization**

The microstructure of the coating before and after testing is shown in Figure 8.5. Dense coatings with metallurgical bonding are obtained using the cold spray deposition process. After the test procedure the coating bond line was intact and no explicit fracture across coating crosssection was visible. The free surface of the coating had considerable cracks and showed inclusion of the brake pad material. Crosssection of tested laser clad Fe-Mn<sub>2</sub> coating is shown in the Figure 8.6. In this case there were no fractures present in the free surface of the coating. Hence the failure mode of cold sprayed coatings could be prevented by improving coating cohesion with higher laser power.

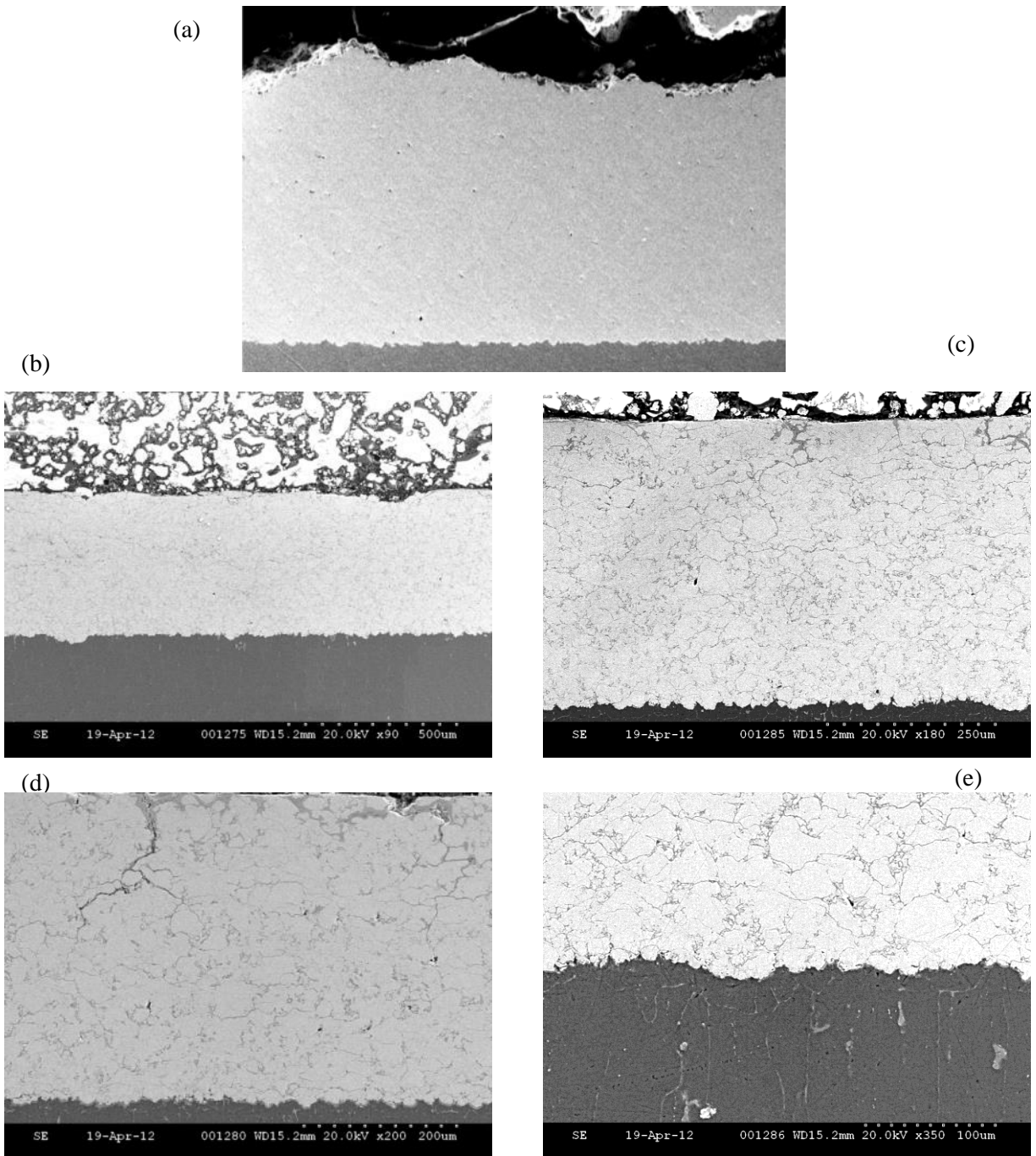


**Figure 8.5: Crosssection of cold sprayed Fe-Mn<sub>2</sub> coatings after testing in the scaled dynamometer**

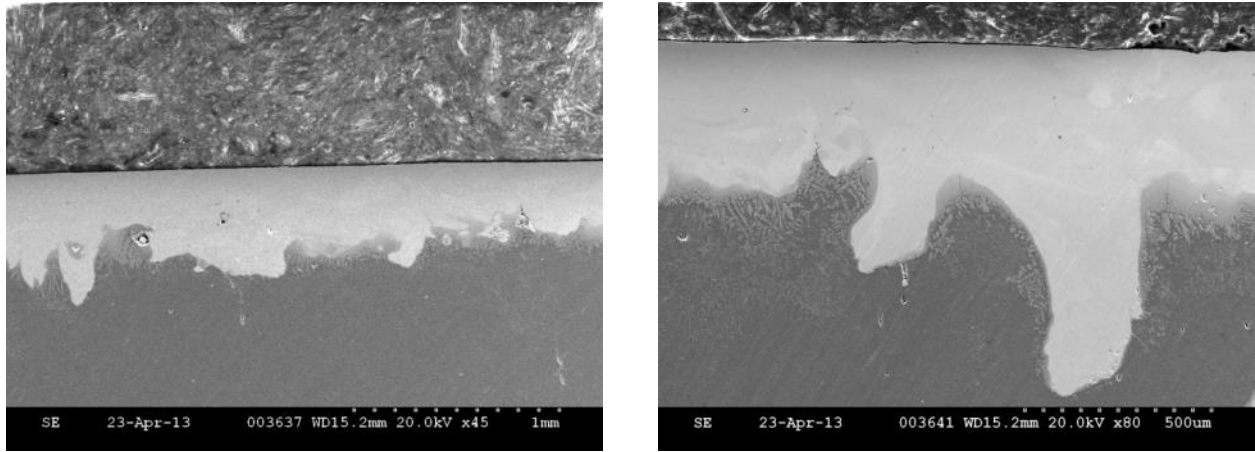


**Figure 8.6: Cross-section of laser clad Fe-Mn2 coated aluminum puck after testing**

### 8.3.2 XRD characterization:

XRD peaks of the tested rotor before and after testing are shown in Figure 8.7. The coatings were polished to remove pad material in order to obtain well defined peaks from the base Fe-Mn2 alloy. The coatings did not undergo phase transformation. There was negligible peak broadening hence the coating phase remained unaffected after testing.

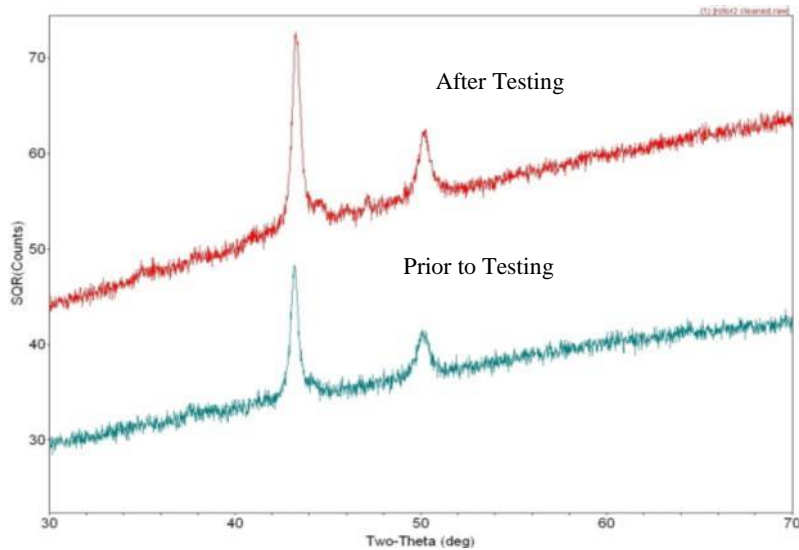


**Figure 8.7: XRD patterns of Fe-Mn2 coating before and after the scaled brake testing**

## 8.4 Summary

Fe-Mn Coating was deposited on aluminum puck and underwent scaled testing. A scaled test setup permits similar temperature profiles as that of the brake rotor in service. A 360 stop brake test was performed in accordance with the FMVSS 105 standard. Analysis was conducted on the bond line and phase homogeneity of the coating. Both these factors are critical for and can lead to sudden failure of the component. Laser clad and cold spray deposited process was utilized to develop the pucks. Laser clad has a slow build rate deposition process but results in excellent density and homogeneity. Despite the presence of brittle intermetallics at the coating interface, its performance remained adequate through the course of the test. The free surface of the clad coating did not show any signs of failure. The cold sprayed coatings were dense and presented an intact bond line post testing. Infiltration of the brake pad material due to formation of cracks were seen this coating. Thermally processed Fe-Mn<sub>2</sub> coatings showed better performance near the free surface of the coatings, while cold sprayed coatings exhibited superior bond strengths. Hence the cold spray deposition parameters have to be tuned to increase cohesive strength.



## 9. General Conclusions and Suggestions

### 9.1 Conclusions

A novel Iron Manganese (Fe-Mn) alloy system was developed as wear resistant coating material that exhibits negligible galvanic coupling with an aluminum alloy (A356). Further the alloy is designed to retain an austenitic phase to reduce coating substrate thermal expansion mismatch. Manganese (Mn), the key component of the material system is an FCC stabilizer. The unique property of the alloy stems from high Mn content which in general reduces the stacking fault energy (SFE) of the alloy system.

Laser cladding was used to synthesize select alloy permutations. This approach results in rapidly solidified microstructure and avoids precipitation and inhomogeneity observed with traditional methods. Wear and corrosion property were determined experimentally

Testing of clad Fe-Mn alloy revealed that higher alloying content of manganese resulted in lower wear resistance. This is due to the presence of martensite at lower Mn content (15wt%). The corrosion property was studied through conventional open circuit, potentiodynamic and zero resistance ammetry (ZRA) techniques. The reduction in corrosion potential with increasing Mn fractions agrees with literature and is due to high dissolution rate of Mn and Fe atoms in Cl- solution. The addition of aluminum and chromium enhance corrosion rate and help stabilize the corrosion potential. At a certain 'sweet spot' the corrosion potential of the Fe-Mn alloy is identical to that of A356 alloy. ZRA was carried out as potentiodynamic plot alone don't determine galvanic current density. A unique composition was identified wherein the galvanic coupling across Fe-Mn - A356 could not be differential from that between itself (A356- A356)

The next part of the study focusses on selection of appropriate process to develop coatings with Fe-Mn alloy system. Coatings precursors are typically wires or fine powders. The low SFE of the Fe-Mn alloys creates difficulty during cold work which limits the possibility of drawing into wires. Possible routes to develop coatings are confined to cored wires and atomized powders. Thermal spray deposition with cored wires resulted in non-homogenous coatings. This resulted in instable wear coefficients and poor corrosion resistance. Powder based thermal coating production such as HVOF and plasma resulted in inflight oxidation and depletion of manganese (due to its low vapor pressure). Shrouded and Inert gas type deposition process can reduce oxidation rate during deposition but these techniques require low surface velocities. This inevitably results in formation of a brittle intermetallic interfacial layer.

In contrast, Cold gas dynamic spray process is a solid state based approach to coating deposition. It could be considered as micro-forming operating that confirms the powders onto desired target. The process is identical to explosive powder compaction, except the powders are not static and travel at supersonic velocities. The nature of the process permits the deposition of Fe-Mn process while preventing oxidation and averting manganese from evaporation.

The study takes a quick diversion to optimize the cold spray process for the present material system. It was revealed that exit gas temperature could help recover cold. It was clear that despite higher particle velocities, the increase in substrate temperature was beneficial to deposition. Downstream injection was utilized and optimized to reduce the high injection pressure requirements and reduce nozzle fouling.

Cold spray processing has material dependent challenges and is seldom reported. Apart from eligibility of the material described in chapter 2, the high strain rate of process mechanically induces phase change. For a ferrous material, phase change from FCC to BCC and/or BCT structures can occur. From experimental findings presented in this study, considerable insight was gained into phase stability and high strain rate deformation mechanism of Iron-Manganese alloys.

The co-axial laser assisted process study outlined the effect of laser power on cold spray process. The proposed mechanism for laser assisted cold spray coatings outlines the effect of laser energy density on the coating process. A shear punch test was utilized to distinguish the effect of the

laser assisted process on the adhesive and cohesive strength of the coating. The adhesive strength – between the target and coating is usually different from the cohesive particle –particle bonding due to differences in shear localization zones. The laser irradiation enhanced both coating adhesion and cohesion showing improvements in bond and shear strength respectively. Unlike externally assisted laser deposition process, mild to moderate laser powers (<500W) were sufficient to achieve improvement in deposition.

## **9.2 Suggestions for future study**

The author feels that there are a few aspects which should be investigated for a better view of some propositions made in this study. These are outlines below:

- It is clear that alloy modification can result in substantial improvement in deposition efficiency. The absence of carbon and addition of ferritic stabilizers might enhance deposition. However, a mixture of material phases in the coating might result in poor corrosion resistance of the material.
- The coaxial laser assisted cold spray process; it will be interested to see the effect of pulsed laser beam with ultra-high frequency. It will also be interesting to see the effect of higher laser power and lower particle velocity to reduce erosive interference.
- Cold spray cannot thermodynamically nucleate phases during deposition. The nucleating phase is often below the particle size requirements of the process. To this end, the laser energy can nucleate precipitates in the material. The process could be used on material systems which will benefit from this precipitation

### 9.3 Publications arising from this work

#### Patent

V Varadaraajan, P S Mohanty, J Boileau, T J Potter, P G Sanders and M J Zaluzec, “Thermally and galvanically compatible wear resistant alloy coated aluminum articles and the application thereof”

#### Journal Papers (In manuscript)

V. Varadaraajan, R. Visveswaran, and P. S. Mohanty, “Iron manganese alloy development using laser based melting: Effect of alloying composition”

V. Varadaraajan and P. S. Mohanty, “Development of Iron manganese alloy coatings on aluminum alloys: Cold spray optimization via numerical modeling and experimental validation”

V. Varadaraajan and P. S. Mohanty , “Cold spray deposition of Fe-Mn coatings for wear resistant

V. Varadaraajan and, P. S. Mohanty , “Coaxial laser assisted cold spray process of Fe-Mn coatings for wear resistant applications - Microstructure characterization – process development”

#### Conference Presentation

V. Varadaraajan and P. S Mohanty, “Role of precursor properties in cold spray coating process”  
Internation the2015, Long beach CA, May 2015

V. Varadaraajan and P. S Mohanty, “Coaxial laser assisted cold spray technology” ITSC 2015,  
Long beach CA, May 2015

## 10. References

- [1] C. B. Fuller, D. N. Seidman, and D. C. Dunand, "Mechanical properties of Al(Sc,Zr) alloys at ambient and elevated temperatures," *Acta Mater.*, vol. 51, no. 16, pp. 4803–4814, Sep. 2003.
- [2] E. . Marquis and D. . Seidman, "Nanoscale structural evolution of Al<sub>3</sub>Sc precipitates in Al(Sc) alloys," *Acta Mater.*, vol. 49, no. 11, pp. 1909–1919, Jun. 2001.
- [3] C. Booth-Morrison, D. N. Seidman, and D. C. Dunannd, "Effect of Er additions on ambient and high-temperature strength of precipitation-strengthened Al–Zr–Sc–Si alloys," *Acta Mater.*, vol. 60, no. 8, pp. 3643–3654, May 2012.
- [4] S. Wilson, "Effect of temperature on the sliding wear performance of Al alloys and Al matrix composites," vol. 196, pp. 270–278, 1996.
- [5] S. V. Prasad and R. Asthana, "Aluminum Metal–Matrix Composites for Automotive Applications: Tribological Considerations," *Tribol. Lett.*, vol. 17, no. 3, pp. 445–453, Oct. 2004.
- [6] W. J. Kim, S. H. Ahn, H. G. Kim, J. G. Kim, I. Ozdemir, and Y. Tsunekawa, "Corrosion performance of plasma-sprayed cast iron coatings on aluminum alloy for automotive components," *Surf. Coatings Technol.*, vol. 200, no. 1–4, pp. 1162–1167, Oct. 2005.
- [7] L. Ajdelsztajn, A. Zúñiga, B. Jodoin, and E. J. Lavernia, "Cold-Spray Processing of a Nanocrystalline Al-Cu-Mg-Fe-Ni Alloy with Sc," *J. Therm. Spray Technol.*, vol. 15, no. June, pp. 184–190, 2006.
- [8] J.-M. Lee, S.-B. Kang, and J. Han, "Dry sliding wear of MAO-coated A356/20vol.% SiCp composites in the temperature range 25–180°C," *Wear*, vol. 264, no. 1–2, pp. 75–85, Jan. 2008.

- [9] J. Tian, Z. Luo, S. Qi, and X. Sun, "Structure and antiwear behavior of micro-arc oxidized coatings on aluminum alloy," *Surf. Coatings Technol.*, vol. 154, no. 1, pp. 1–7, May 2002.
- [10] X. Shi-Gang, S. Li-Xin, Z. Rong-Gen, and H. Xing-Fang, "Properties of aluminium oxide coating on aluminium alloy produced by micro-arc oxidation," *Surf. Coatings Technol.*, vol. 199, no. 2–3, pp. 184–188, Sep. 2005.
- [11] L. Wang, S. Wan, S. C. Wang, R. J. K. Wood, and Q. J. Xue, "Gradient DLC-Based Nanocomposite Coatings as a Solution to Improve Tribological Performance of Aluminum Alloy," *Tribol. Lett.*, vol. 38, no. 2, pp. 155–160, Mar. 2010.
- [12] B. C. De Cooman, K. Chin, and J. Kim, "High Mn TWIP Steels for Automotive Applications."
- [13] O. Bouaziz, S. Allain, C. P. Scott, P. Cugy, and D. Barbier, "High manganese austenitic twinning induced plasticity steels: A review of the microstructure properties relationships," *Curr. Opin. Solid State Mater. Sci.*, vol. 15, no. 4, pp. 141–168, Aug. 2011.
- [14] O. Grassel, L. Kruger, G. Frommeyer, and L. W. Meyer, "High strength Fe–Mn–(Al, Si) TRIP/TWIP steels development — properties — application," *Int. J. Plast.*, vol. 16, pp. 1391–1409, 2000.
- [15] A. S. Hamada, L. P. Karjalainen, and M. C. Somani, "The influence of aluminum on hot deformation behavior and tensile properties of high-Mn TWIP steels," *Mater. Sci. Eng. A*, vol. 467, no. 1–2, pp. 114–124, Oct. 2007.
- [16] M. Opiela, A. Grajcar, and W. Krukiewicz, "Corrosion behaviour of Fe-Mn-Si-Al austenitic steel in chloride solution," vol. 33, no. 2, pp. 159–165, 2009.
- [17] L. Chen, Y. Zhao, and X. Qin, "Some aspects of high manganese twinning-induced plasticity (TWIP) steel, a review," *Acta Metall. Sin. (English Lett.)*, vol. 26, no. 1, pp. 1–15, Jan. 2013.
- [18] A. Saad, Manufacturing, mechanical properties and corrosion behaviour of high-Mn TWIP steels. 2007.

- [19] H.-H. Huang and T.-H. Chuang, "Erosion- and wear-corrosion behavior of Fe-Mn-Al alloys in NaCl solution," *Mater. Sci. Eng. A*, vol. 292, no. 1, pp. 90–95, Nov. 2000.
- [20] L. Remy and A. Pineau, "Twinning and Strain-induced F.C.C. ~ H.C.P. Transformation in the Fe - Mn - Cr - C System," *Mater. Sci. Eng.*, vol. 28, pp. 99–107, 1977.
- [21] E. Bayraktar, F. a Khalid, and C. Levallant, "Deformation and fracture behaviour of high manganese austenitic steel," *J. Mater. Process. Technol.*, vol. 147, no. 2, pp. 145–154, Apr. 2004.
- [22] X. M. Zhu and Y. S. Zhang, "Investigation of the Electrochemical Corrosion Behavior and Passive Film for Fe-Mn, Fe-Mn-Al, and Fe-Mn-Al-Cr Alloys in Aqueous Solutions," *Corrosion*, vol. 54, no. 1, pp. 3–12, Jan. 1998.
- [23] T. Stoltenhoff, H. Kreye, and H. J. Richter, "An Analysis of the Cold Spray Process and Its Coatings," *J. Therm. Spray Technol.*, vol. 11, no. December, pp. 542–550, 2002.
- [24] H. Assadi, F. Gärtner, T. Stoltenhoff, and H. Kreye, "Bonding mechanism in cold gas spraying," *Acta Mater.*, vol. 51, no. 15, pp. 4379–4394, Sep. 2003.
- [25] M. Grujicic, C. . Zhao, W. . DeRosset, and D. Helfrich, "Adiabatic shear instability based mechanism for particles/substrate bonding in the cold-gas dynamic-spray process," *Mater. Des.*, vol. 25, no. 8, pp. 681–688, Dec. 2004.
- [26] D. Helfrich, V. Champagne, and M. Trexler, "Compaction and Work Hardening Through High Velocity Particle Impact," 2007.
- [27] D. L. Gilmore, R. C. Dykhuizen, R. A. Neiser, T. J. Roemer, and M. F. Smith, "Particle Velocity and Deposition Efficiency in the Cold Spray Process," *J. Therm. Spray Technol.*, vol. 8, no. December, pp. 576–582, 1999.
- [28] Q. Wang and M. X. Zhang, "Review on Recent Research and Development of Cold Spray Technologies," *Key Eng. Mater.*, vol. 533, pp. 1–52, Dec. 2012.
- [29] S. Yin, X. Wang, W. Li, and X. Guo, "Examination on Substrate Preheating Process in Cold Gas Dynamic Spraying," *J. Therm. Spray Technol.*, vol. 20, no. 4, pp. 852–859, Feb. 2011.

- [30] M. Yu, W.-Y. Li, F. F. Wang, X. K. Suo, and H. L. Liao, "Effect of particle and substrate preheating on particle deformation behavior in cold spraying," *Surf. Coatings Technol.*, vol. 220, pp. 174–178, Apr. 2013.
- [31] B. Jodoin, P. Richer, G. Bérubé, L. Ajdelsztajn, a. Erdi-Betchi, and M. Yandouzi, "Pulsed-Gas Dynamic Spraying: Process analysis, development and selected coating examples," *Surf. Coatings Technol.*, vol. 201, no. 16–17, pp. 7544–7551, May 2007.
- [32] B. Qin, "Crystallography of TWIP Steel By," Pohang University of Science and Technology, 2007.
- [33] B. Adams, "Simulation of ballistic impacts on armored civil vehicles."
- [34] Y. F. Gong and B. C. De Cooman, "Selective Oxidation and Sub-Surface Phase Transformation of TWIP Steel during Continuous Annealing," *Steel Res. Int.*, vol. 82, no. 11, pp. 1310–1318, Nov. 2011.
- [35] A. Grajcar and W. Krukiewicz, "Corrosion resistance of high-manganese austenitic steels," vol. 41, no. 2, pp. 77–84, 2010.
- [36] I. El-Mahallawi, R. Abdel-karim, and A. Naguib, "Evaluation of effect of chromium on wear performance of high manganese steel," *Mater. Sci. Technol.*, vol. 17, no. November, pp. 1385–1390, 2001.
- [37] L. Bracke, J. Penning, and N. Akdut, "The Influence of Cr and N Additions on the Mechanical Properties of Fe-MnC Steels," *Metall. Mater. Trans. A*, vol. 38, no. 3, pp. 520–528, Apr. 2007.
- [38] E. Toyserkani, A. Khajepour, and S. F. Corbin, *Laser Cladding*. CRC Press, 2004, p. 280.
- [39] M. Grujicic, J. R. Saylor, D. E. Beasley, W. S. DeRosset, and D. Helfritch, "Computational analysis of the interfacial bonding between feed-powder particles and the substrate in the cold-gas dynamic-spray process," *Appl. Surf. Sci.*, vol. 219, no. 3–4, pp. 211–227, Dec. 2003.



- [40] T. Schmidt, F. Gärtner, H. Assadi, and H. Kreye, "Development of a generalized parameter window for cold spray deposition," *Acta Mater.*, vol. 54, no. 3, pp. 729–742, Feb. 2006.
- [41] F. Gärtner, T. Schmidt, T. Stoltenhoff, and H. Kreye, "Recent Developments and Potential Applications of Cold Spraying," *Adv. Eng. Mater.*, vol. 8, no. 7, pp. 611–618, Jul. 2006.
- [42] A. Sova, S. Grigoriev, A. Kochetkova, and I. Smurov, "Influence of powder injection point position on efficiency of powder preheating in cold spray: Numerical study," *Surf. Coatings Technol.*, vol. 242, pp. 226–231, Mar. 2014.
- [43] V. Lemiale, P. C. King, M. Rudman, M. Prakash, P. W. Cleary, M. Z. Jahedi, and S. Gulizia, "Temperature and strain rate effects in cold spray investigated by smoothed particle hydrodynamics," *Surf. Coatings Technol.*, Jun. 2014.
- [44] P. C. King, G. Bae, S. H. Zahiri, M. Jahedi, and C. Lee, "An Experimental and Finite Element Study of Cold Spray Copper Impact onto Two Aluminum Substrates," *J. Therm. Spray Technol.*, vol. 19, no. 3, pp. 620–634, Dec. 2009.
- [45] S. V. Klinkov, V. F. Kosarev, and M. Rein, "Cold spray deposition: Significance of particle impact phenomena," *Aerosp. Sci. Technol.*, vol. 9, no. 7, pp. 582–591, Oct. 2005.
- [46] T. Marrocco, D. G. McCartney, P. H. Shipway, and a. J. Sturgeon, "Production of Titanium Deposits by Cold-Gas Dynamic Spray: Numerical Modeling and Experimental Characterization," *J. Therm. Spray Technol.*, vol. 15, no. 2, pp. 263–272, Jun. 2006.
- [47] S. Yin, X. Wang, W. Li, and B. Xu, "Numerical Study on the Effect of Substrate Angle on Particle Impact Velocity and Normal Velocity Component in Cold Gas Dynamic Spraying Based on CFD," *J. Therm. Spray Technol.*, vol. 19, no. 6, pp. 1155–1162, May 2010.
- [48] T. Klassen, "Influence of Impact Angle and Gas Temperature on Mechanical Properties of Titanium Cold Spray Deposits," vol. 20, no. January, pp. 234–242, 2011.

- [49] K. Binder, J. Gottschalk, M. Kollenda, F. Gärtner, and T. Klassen, "Influence of Impact Angle and Gas Temperature on Mechanical Properties of Titanium Cold Spray Deposits," *J. Therm. Spray Technol.*, vol. 20, no. 1–2, pp. 234–242, Oct. 2010.
- [50] C. Li, W. Li, and Y. Wang, "Effect of Spray Angle on Deposition Characteristics in Cold Spraying," *ITSC*, pp. 91–96, 2003.
- [51] C.-J. Li, W.-Y. Li, Y.-Y. Wang, G.-J. Yang, and H. Fukanuma, "A theoretical model for prediction of deposition efficiency in cold spraying," *Thin Solid Films*, vol. 489, no. 1–2, pp. 79–85, Oct. 2005.
- [52] R. Ghelichi and M. Guagliano, "Coating by the Cold Spray Process : a state of the art," *Frat. ed Integrità Strutt.*, vol. 8, pp. 30–44, 2009.
- [53] S. V. Klinkov, V. F. Kosarev, and M. Rein, "Cold spray deposition: Significance of particle impact phenomena," *Aerosp. Sci. Technol.*, vol. 9, no. 7, pp. 582–591, Oct. 2005.
- [54] A. P. Alkhimov, V. F. Kosarev, and S. V Klinkov, "The Features of Cold Spray Nozzle Design," *J. Therm. Spray Technol.*, vol. 10, no. June, pp. 375–381, 2001.
- [55] J. Vlcek, L. Gimeno, H. Huber, and E. Lugscheider, "A Systematic Approach to Material Eligibility for the Cold-Spray Process," *J. Therm. Spray Technol.*, vol. 14, no. 1, pp. 125–133, Mar. 2005.
- [56] C. Borchers, F. Gärtner, T. Stoltenhoff, and H. Kreye, "Microstructural bonding features of cold sprayed face centered cubic metals," *J. Appl. Phys.*, vol. 96, no. 8, p. 4288, 2004.
- [57] R. C. Mccune, W. T. Donlon, O. O. Popoola, and E. L. Cartwright, "Characterization of Copper Layers Produced by Cold Gas-Dynamic Spraying," *J. Therm. Spray Technol.*, vol. 9, no. March, pp. 73–82, 2000.
- [58] C. L. Sexton, G. Byrne, and K. G. Watkins, "Alloy development by laser cladding: An overview," *J. Laser Appl.*, vol. 13, no. 1, p. 2, 2001.
- [59] R. Vilar and R. Colaço, "Laser-assisted combinatorial methods for rapid design of wear resistant iron alloys," *Surf. Coatings Technol.*, vol. 203, no. 19, pp. 2878–2885, Jun. 2009.

- [60] X. Wu, "Rapidly solidified nonequilibrium microstructure and phase transformation of laser-synthesized iron-based alloy coating," *Surf. Coatings Technol.*, vol. 115, no. 2, pp. 153–162, 1999.
- [61] J. Mazumder, "Microstructure and Wear Properties of Laser Clad Fe-Cr-Mn-C Alloys," *Metall. Trans. A*, vol. 18, no. February, 1987.
- [62] S. C. Tjong and H. C. Tsang, "Laser surface melting of an austenitic Fe-26Mn-7Al-0.9C alloy," *Surf. Coatings Technol.*, vol. 57, pp. 139–144, 1993.
- [63] J. M. Pelletier, F. Oucherif, P. Sallamand, and A. B. Vannes, "Hadfield steel coatings on low carbon steel by laser cladding," *Mater. Sci. Eng. A*, vol. A202, pp. 142–147, 1995.
- [64] A. Wang, C. Fan, C. Xie, W. Huang, and K. Cui, "Laser Cladding of Iron-Base Alloy on Al-Si Alloy and Its Relation to Cracking at the Interface," *J. Mater. Eng. Perform.*, vol. 5, no. December, pp. 775–783, 1996.
- [65] B. Grosogeat, L. Reclaru, M. Lissac, and F. Dalard, "Measurement and evaluation of galvanic corrosion between titanium/Ti6Al4V implants and dental alloys by electrochemical techniques and auger spectrometry," *Biomaterials*, vol. 20, no. 10, pp. 933–941, May 1999.
- [66] V. Varadaraajan, R. K. Guduru, and P. S. Mohanty, "Synthesis and Microstructural Evolution of Amorphous/Nanocrystalline Steel Coatings by Different Thermal-Spray Processes," *J. Therm. Spray Technol.*, vol. 22, no. 4, pp. 452–462, Jan. 2013.
- [67] R. C. Dykhuizen and M. F. Smith, "Gas Dynamic Principles of Cold Spray," *J. Therm. Spray Technol.*, vol. 7, no. June, pp. 205–212, 1998.
- [68] R. C. Dykhuizen, M. F. Smith, D. L. Gilmore, R. A. Neiser, X. Jiang, and S. Sampath, "Impact of High Velocity Cold Spray Particles," *J. Therm. Spray Technol.*, vol. 8, no. December, pp. 559–564, 1999.
- [69] B. Jodoin, "Cold Spray Nozzle Mach Number Limitation," vol. 11, no. December, pp. 496–507, 2002.

- [70] M. Grujicic, C. Tong, W. S. DeRosset, and D. Helfritch, "Flow analysis and nozzle-shape optimization for the cold-gas dynamic-spray process," *Proc. Inst. Mech. Eng. Part B J. Eng. Manuf.*, vol. 217, no. 11, pp. 1603–1613, Jan. 2003.
- [71] S. Li, B. Muddle, M. Jahedi, and J. Soria, "A Numerical Investigation of the Cold Spray Process Using Underexpanded and Overexpanded Jets," *J. Therm. Spray Technol.*, vol. 21, no. 1, pp. 108–120, Oct. 2011.
- [72] J. Pattison, S. Celotto, a. Khan, and W. O'Neill, "Standoff distance and bow shock phenomena in the Cold Spray process," *Surf. Coatings Technol.*, vol. 202, no. 8, pp. 1443–1454, Jan. 2008.
- [73] B. Samareh and a. Dolatabadi, "Dense Particulate Flow in a Cold Gas Dynamic Spray System," *J. Fluids Eng.*, vol. 130, no. 8, p. 081702, 2008.
- [74] S. Yin, X. Wang, and W. Li, "Computational analysis of the effect of nozzle cross-section shape on gas flow and particle acceleration in cold spraying," *Surf. Coatings Technol.*, vol. 205, no. 8, pp. 2970–2977, 2011.
- [75] T. Han, Z. Zhao, B. a. Gillispie, and J. R. Smith, "Effects of Spray Conditions on Coating Formation by the Kinetic Spray Process," *J. Therm. Spray Technol.*, vol. 14, no. 3, pp. 373–383, Sep. 2005.
- [76] S. Dinavahi, V. K. Champagne, and D. J. Helfritch, "Comparison of Empirical and Theoretical Computations of Velocity for a Cold Spray Nozzle," 2009 DoD High Perform. Comput. Mod. Progr. Users Gr. Conf., pp. 27–31, Jun. 2009.
- [77] J.-J. Park, M.-W. Lee, S. S. Yoon, H.-Y. Kim, S. C. James, S. D. Heister, S. Chandra, W.-H. Yoon, D.-S. Park, and J. Ryu, "Supersonic Nozzle Flow Simulations for Particle Coating Applications: Effects of Shockwaves, Nozzle Geometry, Ambient Pressure, and Substrate Location upon Flow Characteristics," *J. Therm. Spray Technol.*, vol. 20, no. 3, pp. 514–522, Aug. 2010.

- [78] V. Champagne, D. Helfritch, P. Leyman, R. Lempicki, and S. Grendahl, "Nozzle Design Influence on the Supersonic Particle Deposition Process by To improve cold spray deposition," in *Cold Spray 2004 Conference*, 2004, pp. 1–21.
- [79] B. Jodoin, F. Raletz, and M. Vardelle, "Cold spray modeling and validation using an optical diagnostic method," *Surf. Coatings Technol.*, vol. 200, no. 14–15, pp. 4424–4432, Apr. 2006.
- [80] B. Samareh, O. Stier, V. Lüthen, and a. Dolatabadi, "Assessment of CFD Modeling via Flow Visualization in Cold Spray Process," *J. Therm. Spray Technol.*, vol. 18, no. 5–6, pp. 934–943, Aug. 2009.
- [81] T. P. Singh, "Investigation of flow parameters of Titanium cold spraying using CFD simulation," Thesis, University of Waikato 2010.
- [82] R. Lupoi and W. O'Neill, "Powder stream characteristics in cold spray nozzles," *Surf. Coatings Technol.*, vol. 206, no. 6, pp. 1069–1076, 2011.
- [83] J. L. Wagner, S. J. Beresh, S. P. Kearney, B. O. Pruett, and E. Wright, "Shock Tube Investigation of Unsteady Drag in Shock- Particle Interactions," no. June, pp. 1–12, 2011.
- [84] X.-J. Ning, Q.-S. Wang, Z. Ma, and H.-J. Kim, "Numerical Study of In-flight Particle Parameters in Low-Pressure Cold Spray Process," *J. Therm. Spray Technol.*, vol. 19, no. 6, pp. 1211–1217, Sep. 2010.
- [85] V. K. Champagne, D. J. Helfritch, S. P. G. Dinavahi, and P. F. Leyman, "Theoretical and Experimental Particle Velocity in Cold Spray," *J. Therm. Spray Technol.*, vol. 20, no. 3, pp. 425–431, Aug. 2010.
- [86] W.-Y. Li, H. Liao, G. Douchy, and C. Coddet, "Optimal design of a cold spray nozzle by numerical analysis of particle velocity and experimental validation with 316L stainless steel powder," *Mater. Des.*, vol. 28, no. 7, pp. 2129–2137, Jan. 2007.
- [87] M. Karimi, A. Fartaj, G. Rankin, D. Vanderzwet, W. Birtch, and J. Villafuerte, "Numerical Simulation of the Cold Gas Dynamic Spray Process," *J. Therm. Spray Technol.*, vol. 15, no. 4, pp. 518–523, Dec. 2006.

- [88] K. Taylor, B. Jodoin, and J. Karov, "Particle Loading Effect in Cold Spray," *J. Therm. Spray Technol.*, vol. 15, no. 2, pp. 273–279, Jun. 2006.
- [89] J. Choi and J. Mazumder, "Non-equilibrium synthesis of Fe-Cr-C-W alloy by laser cladding," *J. Mater. Sci.*, vol. 29, no. 17, pp. 4460–4476, 1994.
- [90] J. Kim, G. Kim, and S. Kim, "The effect of manganese on the strain-induced martensitic transformation and high temperature wear resistance of Fe ± 20Cr ± 1C ± 1Si hardfacing alloy," *J. Nucl. Mater.*, vol. 289, pp. 263–269, 2001.
- [91] P. Sahu, S. Curtze, A. Das, B. Mahato, V.-T. Kuokkala, and S. G. Chowdhury, "Stability of austenite and quasi-adiabatic heating during high-strain-rate deformation of twinning-induced plasticity steels," *Scr. Mater.*, vol. 62, no. 1, pp. 5–8, Jan. 2010.
- [92] A. Soulam, K. S. Choi, Y. F. Shen, W. N. Liu, X. Sun, and M. A. Khaleel, "On deformation twinning in a 17.5% Mn-TWIP steel: A physically based phenomenological model," *Mater. Sci. Eng. A*, vol. 528, no. 3, pp. 1402–1408, Jan. 2011.
- [93] A. Imandoust, A. Zarei-Hanzaki, M. Sabet, and H. R. Abedi, "An analysis of the deformation characteristics of a dual phase twinning-induced plasticity steel in warm working temperature regime," *Mater. Des.*, vol. 40, pp. 556–561, Sep. 2012.
- [94] D. Li, Y. Wei, C. Liu, L. Hou, D. Liu, and X. Jin, "Effects of High Strain Rate on Properties and Microstructure Evolution of TWIP Steel Subjected to Impact Loading," *J. Iron Steel Res. Int.*, vol. 17, no. 6, pp. 67–73, Jun. 2010.
- [95] J. P. Chu, J. M. Rigsbee, G. Banas, and F. V. Lawrence, "Effects of Laser-Shock Processing on the Microstructure and Surface Mechanical Properties of Hadfield Manganese Steel," vol. 26, no. June, pp. 1507–1517, 1995.
- [96] C. Borchers, T. Schmidt, F. Gärtner, and H. Kreye, "High strain rate deformation microstructures of stainless steel 316L by cold spraying and explosive powder compaction," *Appl. Phys. A*, vol. 90, no. 3, pp. 517–526, Nov. 2007.
- [97] C.-J. Li, W.-Y. Li, and H. Liao, "Examination of the Critical Velocity for Deposition of Particles in Cold Spraying," *J. Therm. Spray Technol.*, vol. 15, no. 2, pp. 212–222, Jun. 2006.

- [98] H. Gutzmann, F. Gärtner, D. Höche, C. Blawert, and T. Klassen, “Cold Spraying of Ti<sub>2</sub>AlC MAX-Phase Coatings,” *J. Therm. Spray Technol.*, vol. 22, no. 2–3, pp. 406–412, Nov. 2012.
- [99] L. Yuan, F. Luo, and J. Yao, “Deposition Behavior at Different Substrate Temperatures by Using Supersonic Laser Deposition,” *J. Iron Steel Res. Int.*, vol. 20, no. 10, pp. 87–93, 2013.
- [100] M. Fukumoto, H. Wada, K. Tanabe, M. Yamada, E. Yamaguchi, a. Niwa, M. Sugimoto, and M. Izawa, “Effect of Substrate Temperature on Deposition Behavior of Copper Particles on Substrate Surfaces in the Cold Spray Process,” *J. Therm. Spray Technol.*, vol. 16, no. 5–6, pp. 643–650, Oct. 2007.
- [101] L. C. S. Lacs, D. K. Christoulis, M. Jeandin, E. Irissou, J. Legoux, W. Knapp, and M. Cnrs, “Laser-Assisted Cold Spray (LACS),” 2009.
- [102] P. Poza, C. J. Múnez, M. A. Garrido-Maneiro, S. Vezzù, S. Rech, and A. Trentin, “Mechanical properties of Inconel 625 cold-sprayed coatings after laser remelting. Depth sensing indentation analysis,” *Surf. Coatings Technol.*, 2012.
- [103] A. Cockburn, M. Bray, R. Lupoi, and B. O. Neill, “Laser assisted Cold Spray,” 2009.
- [104] E. O. Olakanmi and M. Doyoyo, “Laser-Assisted Cold-Sprayed Corrosion- and Wear-Resistant Coatings: A Review,” *J. Therm. Spray Technol.*, vol. 23, no. 5, pp. 765–785, Apr. 2014.
- [105] M. Kulmala and P. Vuoristo, “Influence of process conditions in laser-assisted low-pressure cold spraying,” *Surf. Coatings Technol.*, vol. 202, no. 18, pp. 4503–4508, 2008.
- [106] J. H. Andrew DeBiccari, “Laser enhancements of cold sprayed deposits,” 2006.
- [107] P. Poza, C. J. Múnez, M. a. Garrido, S. Vezzù, S. Rech, and a. Trentin, “Effect of laser remelting on the mechanical behaviour of Inconel 625 cold-sprayed coatings,” *Procedia Eng.*, vol. 10, pp. 3799–3804, Jan. 2011.
- [108] M. Bray, A. Cockburn, and W. O’Neill, “The Laser-assisted Cold Spray process and deposit characterisation,” *Surf. Coatings Technol.*, vol. 203, no. 19, pp. 2851–2857, Jun. 2009.

- [109] P. S. Mohanty, "Coaxial laser assisted cold spray nozzle," US 2011/0300306 A12011.
- [110] J. Lin, "Laser attenuation of the focused powder streams in coaxial laser cladding," vol. 12, no. 1, pp. 28–33, 2000.
- [111] P. H. Chong, H. C. Man, and T. M. Yue, "Laser fabrication of Mo-TiC MMC on AA6061 aluminum alloy surface," *Surf. Coatings Technol.*, vol. 154, no. September 2001, pp. 268–275, 2002.
- [112] R. K. Guduru, K. a. Darling, R. Kishore, R. O. Scattergood, C. C. Koch, and K. L. Murty, "Evaluation of mechanical properties using shear-punch testing," *Mater. Sci. Eng. A*, vol. 395, no. 1–2, pp. 307–314, Mar. 2005.
- [113] W. Wong, A. Rezaeian, E. Irissou, J. G. Legoux, and S. Yue, "Cold Spray Characteristics of Commercially Pure Ti and Ti-6Al-4V," *Adv. Mater. Res.*, vol. 89–91, pp. 639–644, Jan. 2010.
- [114] "Vehicle standards," C2ES.ORG. [Online]. Available: <http://www.c2es.org/federal/executive/vehicle-standards>.
- [115] "Mirova/Cambridge Sustainable mobility." Accessed: 2013.
- [116] K. Sakaki and Y. Shimizu, "Effect of the Increase in the Entrance Convergent Section Length of the Gun Nozzle on the High-Velocity Oxygen Fuel and Cold Spray Process," *J. Therm. Spray Technol.*, vol. 10, no. September, pp. 487–496, 2001.
- [117] H. Koivuluoto, A. Coleman, K. Murray, M. Kearns, and P. Vuoristo, "High Pressure Cold Sprayed (HPCS) and Low Pressure Cold Sprayed (LPCS) Coatings Prepared from OFHC Cu Feedstock: Overview from Powder Characteristics to Coating Properties," *J. Therm. Spray Technol.*, vol. 21, no. 5, pp. 1065–1075, May 2012.
- [118] D. Helfritch, V. Champagne, and A. P. Ground, "Optimal Particle Size for the Cold Spray Process by," in *ITSC*, 2006, pp. 1–16.
- [119] T. Schmidt, H. Assadi, F. Gärtner, H. Richter, T. Stoltenhoff, H. Kreye, and T. Klassen, "From Particle Acceleration to Impact and Bonding in Cold Spraying," *J. Therm. Spray Technol.*, vol. 18, no. 5–6, pp. 794–808, Aug. 2009.



- [120] W.-Y. Li, H. Liao, C.-J. Li, G. Li, C. Coddet, and X. Wang, "On high velocity impact of micro-sized metallic particles in cold spraying," *Appl. Surf. Sci.*, vol. 253, no. 5, pp. 2852–2862, Dec. 2006.
- [121] B. Jodoin, L. Ajdelsztajn, E. Sansoucy, a. Zúñiga, P. Richer, and E. J. Lavernia, "Effect of particle size, morphology, and hardness on cold gas dynamic sprayed aluminum alloy coatings," *Surf. Coatings Technol.*, vol. 201, no. 6, pp. 3422–3429, Dec. 2006.
- [122] W.-Y. Li, H. Liao, H.-T. Wang, C.-J. Li, G. Zhang, and C. Coddet, "Optimal design of a convergent-barrel cold spray nozzle by numerical method," *Appl. Surf. Sci.*, vol. 253, no. 2, pp. 708–713, Nov. 2006.
- [123] H. Katanoda, T. Matsuoka, and K. Matsuo, "Experimental study on shock wave structures in constant-area passage of cold spray nozzle," *J. Therm. Sci.*, vol. 16, no. 1, pp. 40–45, Mar. 2007.
- [124] Blau, P. J., & Meyer, H. M. (2003). Characteristics of wear particles produced during friction tests of conventional and unconventional disc brake materials. *Wear*, 255(7-12), 1261–1269. doi:10.1016/S0043-1648(03)00111-X

VV